



System Identification of a Variable Piston Pump and Design of a Hydraulic Load Circuit

Sondre Sanden Tørdal
Andreas Klausen

Supervisor
Michael Rygaard Hansen
Klaus Høj Henriksen

This master's thesis is carried out as a part of the education at the University of Agder and is therefore approved as a part of this education. However, this does not imply that the University answers for the methods that are used or the conclusions that are drawn.

University of Agder, 2015
Faculty of Engineering and Science
Department of Engineering Sciences

Summary

This master thesis is divided into two main parts. The first part focuses on the identification and modeling of a Bosch Rexroth variable piston pump in both frequency and time domain. The second part presents a hydraulic load circuit which is mounted inside a test container. The load circuit is used to test the pump in a suitable load situation which represents a small scale Active Heave Compensation (AHC) scenario.

The considered pump is named A4VSG, and the internal swash plate angle is controlled with a hydraulically driven control system delivered by Bosch Rexroth. Several frequency response tests have been carried out to identify the swash plate angle dynamics. In the time domain, a stochastic input signal have been used to evaluate and verify the time domain response of the internal pump states.

In addition to the traditional frequency response test, a proposed method to identify the swash plate dynamics using a single chirp signal test is presented. The chirp signal is a multi-cycle sine wave with a linearly increasing frequency with time. The chirp test analysis have proven promising results, and should be investigated further in other system identification applications.

The two main pump modeling techniques proposed are; a Black box model using a linear transfer function and a non-linear Grey box model, where all the unknown model parameters have been identified through non-linear optimization in MATLAB. The accuracy of the proposed models are quantified using the mean and maximum deviation between measured and simulated response in both time and frequency domain.

An accurate Grey box model have been identified through non-linear parameter optimization, and a corresponding SimulationX model is created. The simulation model also includes a simplified ripple flow. The simplified ripple flow is found through a mechanical study of the internal piston movements. To quantify the ripple flow effect on the surrounding hydraulic components, two system simulations have been studied and discussed.

The second part of the thesis proposes a hydraulic load circuit using a 4/3-way directional servo valve to control the load pressure across a variable displacement piston motor. The motor is connected to a secondary motor using a mechanical coupling. The secondary motor is placed in a closed hydraulic loop which is controlled using the A4VSG pump described in the first part. The load circuit's purpose is to apply a load torque at the mechanical coupling as the A4VSG's output flow controls the rotational velocity of the coupling. The couplings velocity reference signal is supposed to represent an offshore crane's wire drum motion during AHC.

The two control systems controlling the load pressure and the shaft speed respectively, are designed based on linear control theory. The controllers were tuned using MATLAB's controller tuning

toolbox. In order to use this tool, the systems were described using linearized transfer functions. The resulting controllers have been implemented using a National Instruments LabVIEW program.

In the end the friction torque in both motors combined have been modeled using a non-linear friction model. This model have been used to represent both the stiction and Coulomb friction in the SimulationX model representing the load circuit. The simulation results are compared with real-life experiments to validate the accuracy of the SimulationX model.

Preface

We appreciate the support and guidance provided by our supervisors Professor Michael Rygaard Hansen at the University of Agder and Klaus Henriksen at MacGregor, who have given us valuable support and help throughout the master thesis.

We also want to thank Geir Andre Iversen in the service department at MacGregor for his help in configuring the Bosch Rexroth control card, and Kjetil Lindborg and Markus Westermoen in the Software department for their help in configuring the hardware in the PLC. The group also appreciates the help from Kim Daniel Osmundsen in the Hydraulic department for fitting hydraulic hoses to the system, and Øyvind Solli in the Hydraulic Department for general help during the project.

The group consists of the following two members:

Sondre Sanden Tørdal

Sondre Sanden Tørdal

Andreas Klausen

Andreas Klausen

Grimstad, May 20, 2015

Contents

Summary	ii
Preface	iv
List of Figures	vi
List of Tables	vii
Nomenclature	viii
1 Introduction	1
1.1 Problem Statement and Motivation	2
1.2 Key Assumptions and Limitations	3
1.3 Design Criteria	6
1.4 Report Structure	7
2 Method	9
2.1 Considered Test Types	10
2.1.1 Frequency Response Test	10
2.1.2 Chirp Signal Test	11
2.1.3 Stochastic Wave Test	11
2.2 Sine Fitting using Least Squares Method	11
2.3 Frequency Response Analysis	13
2.4 Black Box Transfer Function Estimation	16
2.5 Frequency Response Analysis using Chirp Signal	17
2.6 Parameter Estimation	19
2.6.1 Non-Linear Optimization Algorithm	20
2.6.2 Optimization Objective Functions	20
2.7 Model Accuracy Verification	22
3 Hydraulic Pump Model	23
3.1 Test Setup	24
3.1.1 Location	24
3.1.2 Physical Layout	24
3.1.3 Software Layout	26
3.2 Hydraulic Actuating Circuit	27
3.2.1 Governing Equations	27

3.2.2	Non-Linear State Space Model	30
3.3	Microcontroller Control Circuit	31
3.4	Internal Pump Model	32
3.4.1	Swash Plate Mechanism	33
3.4.2	Piston Kinematics	34
3.4.3	Ripple Flow Modeling	37
3.4.4	Ripple Flow Amplitude Analysis	41
3.4.5	Empirical Simplification of the Ripple Flow	42
3.5	SimulationX Model	45
4	Results from Hydraulic Pump Model	47
4.1	Steady State Pump Flow Measurements	48
4.2	Black Box Model	49
4.2.1	No-Load Situation	49
4.2.2	Load Situation	50
4.2.3	Comparison Between Load and No-Load Situations	51
4.2.4	Black Box Model Accuracy	52
4.3	Chirp Test Compared to Traditional Frequency Response Test	54
4.4	Optimization of Non-Linear Grey Box Model	57
4.4.1	Resulting Model Parameters	57
4.4.2	Grey Box Model Accuracy	59
4.5	Analysis of the Ripple Flow Effect	64
5	Hydraulic Load Simulation Circuit	67
5.1	Physical Test Bench Description	68
5.2	Load Circuit Analysis	72
5.3	Supply Circuit Analysis	75
5.4	Control System Design	79
5.5	Friction Model	82
5.6	SimulationX Model	84
5.7	Active Heave Compensation Simulation Model	85
6	Results from Hydraulic Load Simulation Circuit	89
6.1	Controller Tuning	90
6.2	Identification of Friction Model Parameters	93
6.3	Verification of SimulationX Model	94
6.4	Simulated Step Test Verification of Control Parameters	97
7	Discussion and Conclusions	99
7.1	Hydraulic Pump Model	100
7.2	Hydraulic Load Simulation Circuit	101
Bibliography		103
Appendices		106
A	Stochastic Wave Generation	106
B	Transfer Function Estimation	109
C	Bode Plot Comparisons	110
D	Sensors and Components	117
D.1	Bosch Rexroth A4VSG Closed Loop Pump	117
D.2	Control Actuating Circuit with Proportional Valve	118

CONTENTS

D.3	Pump Microcontroller Control Card	119
D.4	Parker V12 Variable Displacement Motor	119
D.5	Inductive Transmitter	120
D.6	Parker Servo Valve	120
D.7	HYDAC Flow Sensors	121
D.8	HYDAC Pressure Transmitter	122
D.9	National Instruments myRIO	122
D.10	Laptop Computer	122
E	Static Model Parameters	123
F	SimulationX Model of the A4VSG pump	124
G	SimulationX Model of the Hydraulic Load Circuit	127
H	Detailed Overall Hydraulic Drawing	131

List of Figures

1.1	Schematic of a variable axial piston pump.	2
1.2	Simplified overview of the loading circuit and the closed loop pump.	3
2.1	Typical reference input signal used in a frequency response test.	10
2.2	Reference signal, measured and fitted system response input frequencies at 10 and 30 Hz.	13
2.3	Sine input and output at low and high frequencies.	14
2.4	Example of a bode plot at 50% offset and 10% amplitude.	15
2.5	Comparison between an estimated TF and discrete frequency response test.	16
2.6	Illustration of chirp test analysis.	17
2.7	Bode plot comparison between frequency response analysis and chirp response analysis.	19
2.8	Schematic illustration of the optimization objective.	21
3.1	Physical test setup. Picture of NI myRIO and BR VT-VPCD are taken from [1] and [2] respectively.	25
3.2	Hydraulic actuating mechanism.	27
3.3	Geometry of the sliding connection between the swash plate and the cylinder.	29
3.4	Block diagram of the hydraulic circuit and the accompanying control loop.	31
3.5	Illustration of a variable displacement piston pump.	33
3.6	2D vector loop of each axial piston.	34
3.7	Illustration of the piston kinematics.	35
3.8	Illustration of the porting lens plate.	37
3.9	Ripple flow in port A and port B.	41
3.10	Ratio between ripple flow and mean flow.	42
3.11	Comparison of simplified vs. actual ripple flow with 9 pistons.	44
3.12	Block diagram of the A4VSG pump model.	45
4.1	Comparison between flow measurement and theoretical flow at no load.	48
4.2	Frequency response comparison between a load and a no-load situation at 5% amplitude.	51
4.3	Frequency response comparison between a load and a no-load situation at 10% amplitude.	52
4.4	Frequency response analysis compared to chirp response analysis @ A = 20%.	55
4.5	Frequency response analysis compared to chirp response analysis @ A = 20%.	56
4.6	Comparison of internal measured and simulated values for the locked parameter model.	61
4.7	Comparison of internal measured and simulated values for the free parameter model.	62
4.8	Block diagram of the SimulationX program used to test ripple frequencies over a hose.	64

4.9	Comparison of flow before and after hose.	64
4.10	Simulation X Block diagram for pressure relief valve test.	65
4.11	Simulated pressure relief valve opening percentage.	65
5.1	Picture of the physical test bench, where the two motors are connected using a mechanical coupling.	68
5.2	Laptop running LabVIEW for monitoring and control of the load circuit. The hand held controller to the left is used to set speed and load references.	69
5.3	Overview of the analog joystick controllers.	69
5.4	Inductive sensor fitting. Here shown when the output signal is false.	70
5.5	Load circuit electronic layout. Picture of NI myRIO, BR VT-VPCD and Siemens PLC is taken from [1], [2] and [3] respectively.	71
5.6	Simplified overview of the hydraulic load circuit.	72
5.7	Load circuit block diagram.	75
5.8	Supply circuit diagram.	76
5.9	Supply circuit block diagram.	78
5.10	Control loops; using the load circuit to control the force/pressure and the supply circuit to control the shaft rotational speed.	79
5.11	Illustration of the friction model.	82
5.12	Simplified test bench model used to identify the friction.	83
5.13	Block diagram of the SimulationX model of the load circuit.	84
5.14	The AHC scenario offshore, where a payload shall be lowered and hoisted to the seabed with a closed loop hydraulic actuating circuit.	85
5.15	Heave motion of the vessel due to a stochastic wave.	88
5.16	Pressure difference during ideal heave compensation.	88
6.1	Bode plot illustrating load circuit tuning.	91
6.2	Bode plot illustrating supply circuit tuning.	91
6.3	Comparison between the measured and the modeled friction.	93
6.4	Comparison of measured and simulated rotational shaft velocity, when a stochastic velocity reference signal is applied to simulate a small scale AHC.	95
6.5	Comparison of measured and simulated load pressure, when a static pressure reference signal is applied during AHC.	95
6.6	Comparison of measured and simulated supply pressure during AHC.	96
6.7	Load pressure reference step on simulation model.	97
6.8	Speed reference step on simulation model.	97
1	Example of a Pierson-Moskowitz spectrum.	106
2	Evenly spaced wave spectrum.	107
3	Stochastic wave.	108
4	System identification toolbox layout [4].	109
5	Test data compared with Black and Grey Box model @ O = 25%.	111
6	Test data compared with Black and Grey Box model @ O = 50%.	112
7	Test data compared with Black and Grey Box model @ O = 75%.	113
8	Test data compared with Black and Grey Box model @ O = -25%.	114
9	Test data compared with Black and Grey Box model @ O = -50%.	115
10	Test data compared with Black and Grey Box model @ O = -75%.	116
11	Bosch Rexroth axial piston variable pump A4VSG [5].	117
12	Pump control unit with a servo valve [6].	118
13	Bosch Rexroth actuating circuit valve control card [7].	119
14	Parker V12 bent axis variable displacement pump [8].	119

LIST OF FIGURES

15	Parker D3FP Servo valve [9].	120
16	Parker Servo Valve approximated dynamics.	121
17	HYDAC Flow sensor	121
18	The SimulationX model of the pump.	124
19	The SimulationX Modelica block model of the pump.	126
20	SimulationX model of the Load Circuit test bench.	128
21	SimulationX model of Controllers.	130

List of Tables

1.1	Key assumptions and limitations associated with pump system identification process.	4
1.2	Key assumptions and limitations associated with the load circuit design and verification process.	5
1.3	Performance criteria of models in the frequency domain.	6
1.4	Performance criteria of models in the time domain.	6
4.1	Estimated TFs describing the dynamics of the swash plate during no load.	50
4.2	Pressure drop over the orifice with a certain swash plate angle.	50
4.3	Estimated TFs describing the dynamics of the swash plate during load.	51
4.4	Black Box model verification - Frequency domain.	53
4.5	Estimated Parameters for the Locked Grey Box Model.	58
4.6	Estimated Parameters for the Free Grey Box Model.	58
4.7	Locked Grey Box model verification - Frequency domain.	59
4.8	Free Grey Box model verification - Frequency domain.	60
4.9	Grey Box model verification - Time domain.	62
5.1	Transfer function parameters.	80
6.1	Transfer function parameters.	90
6.2	Optimized friction model parameters.	94
1	A4VSG pump parameters.	118
2	Hydraulic control circuit parameters.	118
3	Parker V12 data sheet specifications.	120
4	Parker servo valve specifications.	120
5	Static model parameters used in all simulations of the A4VSG pump.	123
6	Variable explanation of SimX Model part 1.	125
7	Variable explanation of SimX Model part 2.	125
8	Variable explanation of SimX Model part 3.	125
9	Variable explanation of SimX Model part 4.	126
10	Variable explanation of SimX Model part 5.	126
11	Variable explanation of SimX Model part 1 - Friction model.	127
12	Variable explanation of SimX Model part 3 - Swash plate angle controller.	129
13	Variable explanation of SimX Model part 4 - Servo valve control system.	129
14	Variable explanation of SimX Model part 5 - Coupling pulse counter system.	129
15	Variable explanation of SimX Model part 6 - Other variables.	130

Variable	Unit	Explanation
$y^{(ref)}$	—	Input signal to the system.
A	—	Amplitude of the input sine wave.
f	Hz	Frequency of the input sine wave.
O	—	Offset of the input sine wave.
t	s	The time.
$y_{chirp}^{(ref)}$	—	Chirp signal.
A_C	—	Amplitude of the chirp signal.
f_0	Hz	Initial frequency of the chirp signal.
k_{chirp}	Hz/s	The frequency ramp gradient.
f_1	Hz	Final frequency of the chirp signal.
t_1	s	The time where the sine wave frequency reaches f_1 .
$\hat{y}(t)$	—	Estimated system response.
$y(t)$	—	Measured system response.
\hat{A}	—	Estimated amplitude of the sine wave.
$\hat{\phi}$	rad	Estimated phase angle of the sine wave.
\hat{O}	—	Estimated offset of the sine wave.
c_i	—	Element i in vector \vec{c} .
M_f	dB	Magnitude of the system at a given frequency.
$\hat{A}_{@0.1Hz}$	%	Amplitude of the optimized sine \hat{a} at $f = 0.1Hz$.
b_0	—	Constant value describing the TF numerator.
$a_4 \dots a_0$	—	Constant value describing the TF denominator.
$M_{top,i}$	dB	Magnitude of the top chirp response.
$M_{bot,i}$	dB	Magnitude of the bottom chirp response.
$M_{C,i}$	dB	Mean magnitude of the chirp response.
$y_{top,i}$	—	Response at positive peak i .
$y_{bot,i}$	—	Response at negative peak i .
O_C	—	Offset of the chirp signal.
$P_{top,i}$	deg	Phase of the top chirp response.
$P_{bot,i}$	deg	Phase of the bottom chirp response.
$P_{C,i}$	deg	Mean phase of the chirp response.
$\Delta t_{top,i}$	s	Time lag between input and response positive peak i .
$\Delta t_{bot,i}$	s	Time lag between input and response negative peak i .
$f_{top,i}$	Hz	Frequency of the input signal at time of positive input signal peak i .
$f_{bot,i}$	Hz	Frequency of the input signal at time of negative input signal peak i .
$f_{C,i}$	Hz	Frequency of magnitude $M_{C,i}$ and phase $P_{C,i}$.
$\vec{\Phi}$	—	Parameter vector.
$f(\vec{\Phi})$	—	Objective value with a certain parameter vector.
\vec{L}_b	—	Lower linear bounds of $\vec{\Phi}$

Variable	Unit	Explanation
\vec{U}_b	—	Upper linear bounds of $\vec{\Phi}$
$B(\vec{\Phi}, \mu)$	—	Barrier function.
μ	—	Small positive scalar often called the “barrier parameter”.
i	—	Implies element i in the given vector.
m	—	Length of the vector.
$f_{\text{time}}(\vec{\Phi})$	—	Time domain objective function.
\bar{y}	—	Measured system response.
\bar{y}_{sim}	—	Simulated system response.
$f_{\text{freq.}}(\vec{\Phi})$	—	Frequency domain objective function
\vec{M}	dB	Measured response magnitude.
$\vec{\phi}$	deg	Measured response phase.
\vec{M}_{sim}	dB	Simulated response magnitude.
$\vec{\phi}_{\text{sim}}$	deg	Simulated response phase.
$\frac{90}{20}$	—	Weighting factor of magnitude deviations.
$f_{\text{comb.}}(\vec{\Phi})$	—	The combined time and frequency domain objective function
\bar{E}_X	—	Average absolute deviation between the experiments and the simulation.
ΔX_i	—	Deviation measurement i between the experiments and the simulation model.
N_s	—	Total number of compared samples.
$E_X^{(\max)}$	—	Maximum deviation between the simulated and the experiments.
Q_1	m^3/s	Volume flow into cylinder chamber 1.
Q_2	m^3/s	Volume flow out of cylinder chamber 2.
p_P	Pa	Pressure on the P-port.
p_T	Pa	Pressure on the T-port.
p_1	Pa	Pressure in cylinder chamber 1.
p_2	Pa	Pressure in cylinder chamber 2.
u	—	Valve spool position.
$K(u)$	m^2	Effective valve opening area.
ρ	kg/m^3	Density of the oil.
$k_1 \dots k_3$	m^2	Flow area coefficients.
\dot{p}_1	Pa/s	Pressure gradient in cylinder chamber 1.
\dot{p}_2	Pa/s	Pressure gradient in cylinder chamber 2.
β	Pa	Oil stiffness.
V_0	m^3	Dead volume on each cylinder side.
A_p	m^2	Cylinder pistons effective area.
x_p	m	Cylinder piston position.
\dot{x}_p	m/s	Cylinder piston velocity.
Q_{Leak}	m^3/s	Leakage flow from cylinder chamber 1 to 2.
K_L	m^2	Effective orifice opening between cylinder chamber 1 and 2.

Variable	Unit	Explanation
a	m	Normal distance between the cylinder rod and the swash plate.
α	rad	Swash plate tilt angle.
α_{max}	rad	Maximum swash plate tilt angle.
L	m	Cylinder stroke length.
\ddot{x}_p	m/s^2	Cylinder piston acceleration.
k	N/m	Spring coefficient in cylinder.
b	Ns/m	Damping coefficient in cylinder.
m_{eff}	kg	Effective translational mass.
$\dot{\alpha}$	rad/s	Swash plate tilt angular velocity.
$\ddot{\alpha}$	rad/s^2	Swash plate tilt angular acceleration.
\vec{x}	—	State vector representing all internal states.
$f(\vec{x}, u)$	—	State equations.
$\dot{\vec{x}}$	—	Time derivative of the state vector.
$g(\vec{x}, u)$	—	Output function.
$x_1 \dots x_4$	—	The four states in \vec{x} .
G_{PD}	—	Transfer function describing the PD-controller.
K_d	—	Proportional gain.
T_d	s	Time constant.
G_P	—	Transfer function describing the P-controller.
K_p	—	Proportional gain.
$G_v(s)$	—	Transfer function for the valve.
$u(s)$	—	Actual valve spool position.
$u^{(ref)}(s)$	—	Valve spool reference signal
ω_v	rad/s	Natural frequency of the valve.
ζ_v	—	Damping ratio of the valve.
$G_I(s)$	—	Inner transfer function.
$e^{-\tau s}$	—	The time delay transfer function.
$e(s)$	rad	Error between $\alpha^{(ref)}$ and α .
\bar{Q}	m^3/s	Mean steady state flow produced by the pump.
ω	rad/s	Motoring shaft speed.
$V_{d,max}$	m^3/rev	Maximum pump displacement.
$\vec{r}_{0,n}$	m	Vector from origin to axial axis of piston n .
$\vec{x}_{p,n}$	m	Vector from end of $\vec{r}_{0,n}$ to the revolute joint center.
\vec{r}_n	m	Vector from origin to revolute joint.
θ_n	rad	Angular position of piston n in the x-y plane.
r_0	m	Length of $\vec{r}_{0,n}$.
$x_{p,n}$	m	Length of $\vec{x}_{p,n}$.
φ_n	rad	Angle between $\vec{r}_{0,n}$ and \vec{r}_n .

Variable	Unit	Explanation
r_n	m	Length of \vec{r}_n .
φ_0	rad	Angle between horizontal and $\vec{x}_{p,n}$.
$\dot{\varphi}_n$	rad/s	Angular velocity of the angle between $\vec{r}_{0,n}$ and \vec{r}_n .
$\dot{\theta}_n$	rad/s	Angular velocity of piston n .
\dot{r}_n	m/s	Change in length of \vec{r}_n .
$\dot{x}_{p,n}$	m/s	Velocity of piston n .
L_{eff}	m	Effective stroke length of each piston.
$\theta_{A,O}$	rad	Opening angle on port A.
$\theta_{A,C}$	rad	Closing angle on port A.
$\theta_{B,O}$	rad	Opening angle on port B.
$\theta_{B,C}$	rad	Closing angle on port B.
D_p	m^2	Piston diameter.
θ	rad	Angular position of the input shaft.
θ_0	rad	Initial rotation of the input shaft.
θ_{open}	rad	Opening angle on the port plate.
R	m	Radius of the port plate.
γ	rad	Pressure carry over angle [10].
n	—	Piston number.
$\Delta\theta$	rad	Separation angle between each neighboring piston.
N_p	—	Total number of pistons in the pump.
$u_{A,n}$	—	Opening between piston chamber n and port A.
$u_{B,n}$	—	Opening between piston chamber n and port B.
Q_n	m^3/s	Flow generated by piston n .
$Q_{P,A}$	m^3/s	Flow through port A.
$Q_{P,B}$	m^3/s	Flow through port B.
$\bar{Q}_{P,A}$	m^3/s	Steady State flow from port A.
$\bar{Q}_{P,B}$	m^3/s	Steady State flow from port B.
$\Delta Q_{P,A}^{(Simp)}$	m^3/s	Simplified ripple flow.
A_r	m^3/s	Simplified ripple amplitude.
f_r	rad/s	Ripple frequency.
O_r	m^3/s	Simplified ripple offset.
ψ	—	Empirical ratio of the ripple flow amplitude.
ω_s	rad/s	The rotational velocity of the shaft/coupling.
$\alpha^{(ref)}$	%	The reference control signal to the A4VSG pump.
ΔT	s	The measured time between each rising pulse.
Q_{sv}	m^3/s	The flow through the servo valve.
u_{sv}	—	Actual servo valve spool opening.
$p_{s,L}$	Pa	Load circuit supply pressure.

Variable	Unit	Explanation
p_L	Pa	Load pressure across the motor.
K_{qu}	m^3/s	Spool opening flow gain coefficient.
K_{qp}	$\text{m}^4\text{s}/\text{kg}$	Pressure flow gain coefficient.
Q_L	m^3/s	The load flow through the motor.
$K_L(\alpha_L)$	m^3/rad	Motor gain coefficient.
ω_L	rad/s	Motor shaft rotational speed.
α_L	rad	Motor swash plate angle.
T_L	Nm	Load torque.
$\alpha_{L,max}$	rad	Maximum swash plate angle of the Parker V12 motor.
$V_{m,max}$	m^3/rev	Maximum motor displacement.
\dot{p}_L	Pa/s	Load pressure gradient.
V_{L0}	m^3/s	The dead volume on each side of the motor.
$\dot{\omega}_L$	rad/s^2	Motor shaft acceleration.
T_s	Nm	Supply torque generated by the hydraulic supply circuit.
J_{eff}	kgm^2	The effective inertia of both the motors and the connecting shaft.
c	—	Rotational friction coefficient.
Q_P	m^3/s	The delivered flow from the A4VSG variable piston pump.
K_P	$\text{m}^3/(\text{rad} \cdot \text{s})$	Flow/pressure gain coefficient as function of α .
$\alpha^{(ref)}(s)$	rad	Swash plate angle reference signal.
$G_{est}(s)$	—	Estimated Black box transfer function in Section 4.2.1.
Q_s	m^3/s	Supply circuit flow.
p_s	Pa	Pressure difference across the motor.
$K_s(\alpha_s)$	m^3/rad	Supply circuit motor gain.
α_s	rad	Supply circuit motor swash plate angle.
$p_{A,s}$	Pa	Hydraulic pressure at pump port A.
$p_{B,s}$	Pa	Hydraulic pressure at pump port B.
$\alpha_{s,max}$	rad	The maximum swash plate angle of the supply circuit motor.
\dot{p}_s	Pa/s	Supply pressure gradient.
V_{s0}	m^3	Dead volume on each side of the motor.
$\dot{\omega}_s$	rad/s^2	Rotational acceleration of the shaft.
T_i	s	Integration time constant.
$u(k)$	—	The current cycle control signal.
$u(k-1)$	—	The previous cycle control signal.
$e(k)$	—	The current cycle error signal.
$e(k-1)$	—	The previous cycle error signal.
Δt	s	Time between each cycle interrupt.
$\alpha^{(feed)}$	rad	A4VSG swash plate angle feed-forward signal.
$\omega_s^{(ref)}$	rad/s	Rotational shaft speed reference signal.

Variable	Unit	Explanation
$u_{sv}^{(feed)}$	—	Servo valve opening feed forward signal.
$K_L(\alpha_s)$	—	Supply circuit motor gain.
N	—	Number of wave components.
$z_v(t)$	m	The stochastic wave propagation in the heave direction.
$z_{v,n}(t)$	m	Each single wave component n given by the stochastic wave energy spectrum.
\ddot{z}_{PL}	m/s^2	z-directional acceleration of the payload.
F_L	N	The force due to the wire tension.
F_{buoy}	N	Buoyancy force.
F_{drag}	N	Drag force due to viscous friction in the sea water.
m_{PL}	kg	Gravitational mass of the payload.
ρ_s	kg/m^3	The sea water density.
C_d	—	The drag force coefficient, dependent to the payload shape.
A_{PL}	m^2	Payloads projected area in the z-direction.
\dot{z}_{PL}	m/s	z-directional velocity of the payload.
g	m/s^2	Earth's gravity constant.
V_{PL}	m^3	The submerged volume of the payload.
k_w	N/m	Wire spring stiffness.
E_w	Pa	Wire elasticity modulus.
A_w	m^2	Wire cross-section area.
L_w	m	Length of the wire.
c_w	Ns/m	Wire damping force coefficient.
z_v	m	Motion of the floating vessel.
r_d	m	Wire drum radius.
θ_s	rad	Wire drum rotation angle.
$\tau_f(\omega_s)$	Nm	Model friction torque due to the rotational shaft velocity.
τ_s	Nm	The maximum friction exceeded in the model due to stiction.
τ_c	Nm	Coulomb friction during high rotational velocities.
τ_0	Nm	Friction at ω_0 .
ω_0	rad/s	The rotational velocity at τ_0 .
r	—	Gradient factor describing the steepness of the $tanh$ curve.
$\dot{\omega}_s$	rad/s^2	Rotational acceleration found from numerical differentiation.
$\vec{\tau}_f(\vec{\Phi}_f, \omega_s)$	Nm	The calculated friction torque due to the friction model parameters $\vec{\Phi}_f$.
$\vec{T}_f(\dot{\omega}_s)$	Nm	Experimental friction at a given rotational velocity ω_s .
$\vec{\Phi}_f$	—	Vector containing the unknown friction model parameters.
S_x	m^2/s	Stochastic wave spectrum.
ω_{st}	rad/s	Frequency of a stochastic wave part.
H_s	m	Significant wave height.
T_p	s	Significant wave period.

Variable	Unit	Explanation
C_n	m	Amplitude of sine wave n .
$\omega_{s,n}$	rad/s	Frequency of sine wave n .
$\Delta\omega_s$	rad/s	Frequency between $\omega_{s,n+1}$ and $\omega_{s,n}$.
$x_n(t)$	m	Wave component n .
ϵ	rad	Random number $\in [0, 2\pi]$.

Chapter **1**

Introduction

1.1 Problem Statement and Motivation

MacGregor is a huge supplier of offshore cranes. Their demand for accurate simulation models increases continuously since their solutions need to be more complex and accurate. A method to identify the dynamic behavior of the core components such as hydraulic pumps, valves and motors is needed in order to meet such demands.

This master thesis present two methods to identify the swash plate dynamics of a variable piston pump (A4VSG) produced by Bosch Rexroth. The pistons inside the pump are attached to a swash plate which rotates with the input shaft. As this swash plate is tilted, the pistons are forced to move axially and suck oil from one port and push it out through another. This is illustrated in Figure 1.1 where the tilt angle of the swash plate is demonstrated. The tilt angle is controlled using a separate hydraulic circuit including a 4/3-way proportional valve and a cylinder. The cylinder is mechanically connected to the swash plate which makes it tilt. The task is to identify the parameters in a model of this circuit which should have matching dynamic characteristics of the real pump. The methods used will also be applicable to identify other components such as hydraulic valves and motors.

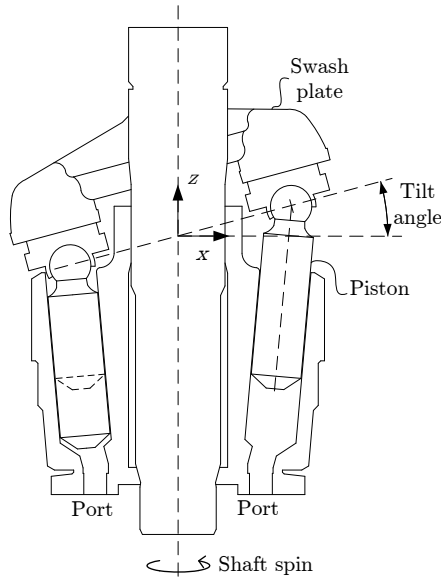


Figure 1.1: Schematic of a variable axial piston pump.

In addition, the company requires a functional load circuit which can apply a load scenario to the pump. The motivation for constructing such a load circuit is that the company lacks a practical and cost efficient method of testing newly developed control systems. Also the load circuit can be used to train newly hired service and engineering personnel.

The dynamic model of the swash plate dynamics will be verified through real life tests in both the frequency and time domain. Since SimulationX is the preferred simulation software used by MacGregor today, a SimulationX model of the A4VSG pump is constructed. The load circuit will be designed and constructed, tested and verified with a suitable control system. The master thesis can be seen as two main parts where the system identification of the swash plate dynamics plays the major role, and the load circuit design and verification part plays a minor role.

The problem is illustrated using a schematic figure describing the load circuit and the Bosch Rexroth A4VSG variable piston pump. The hydraulic load circuit consist of a supply pump, a servo valve and two motors connected to each other using a mechanical coupling. Figure 1.2 shows the two main hydraulic circuits within their area of red stapled lines.

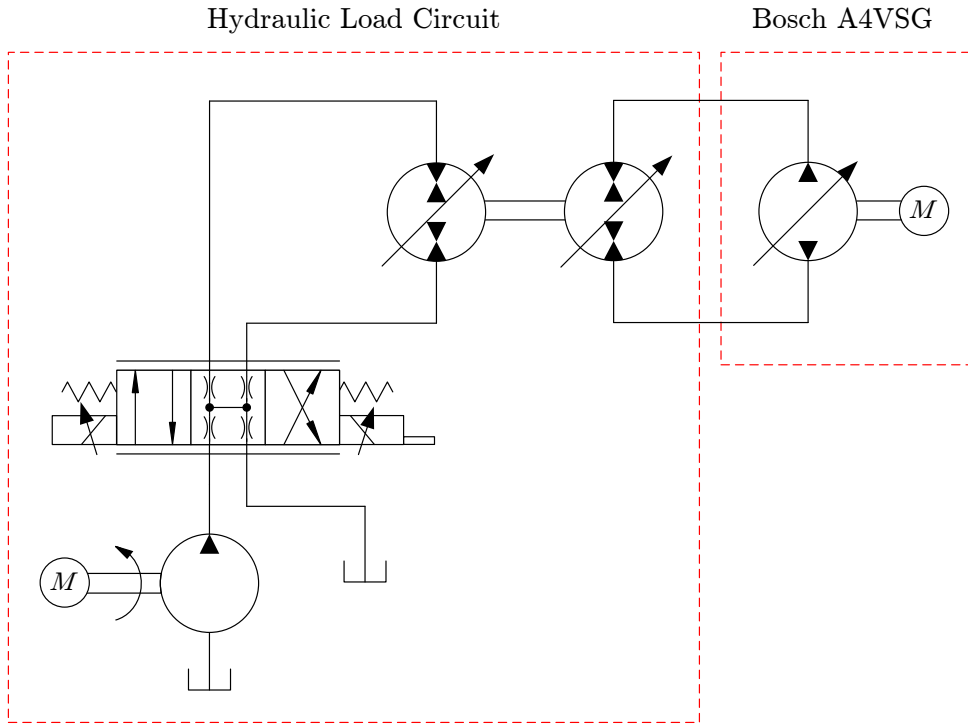


Figure 1.2: Simplified overview of the loading circuit and the closed loop pump.

The main objectives in this thesis are divided in two main parts. The two tasks to be carried out are:

- System identification and modeling of the variable hydraulic piston pump (A4VSG) produced by Bosch Rexroth. Several identification procedures are investigated.
- Design and construction of the hydraulic load circuit. A control system should also be developed in order to generate an appropriate load scenario. The load circuit should also be tested and verified through real life test using a physical test bench.

The master thesis also includes practical work such as electrical wiring and instrumentation. However, this part will not be documented in detail.

1.2 Key Assumptions and Limitations

A model describing the hydraulic pump swash plate dynamics in both time and frequency domain should be established. The pump should interact with a load circuit which shall reproduce a small scale offshore AHC scenario. There are some key assumptions and limitations considered in both parts of the project. They are listed and described in Tables 1.1 and 1.2.

Table 1.1: Key assumptions and limitations associated with pump system identification process.

System Identification of the Bosch Rexroth A4VSG Variable Displacement Pump	
Key Assumptions	
1.	Create a fully functional LabVIEW test program to carry out several tests on the closed loop pump.
2.	Determine the swash plate angle dynamics using a frequency response test.
3.	Identify several Black box models describing the dynamics in all tested offsets and amplitudes individually.
4.	Model the pump using a Grey box model, and identify the model parameters using non-linear optimization techniques.
5.	Investigate several methods to identify the swash plate angle dynamics.
6.	Identify the bundled pump controller cards internal controller gains.
7.	Model the internal piston kinematics, and model the ripple flow effect using the pistons movement as function of the input shaft velocity and the swash plate angle.
8.	Create a non-linear SimulationX model describing both the swash plate dynamics and ripple flow.
9.	Verify the Black and Grey box models in time and frequency domain.
Associated Limitations	
1.	The bundled pump controller card only includes two analog test outputs to measure the internal states of the pump.
2.	Not possible to account for the temperature deviations during the testing.
3.	It is not guaranteed that a linear Black box model described using a transfer function will fit the frequency response tests.
4.	Almost all soft and hard parameters are unknown and the pump mechanism design is not specified in detail.
5.	Some of the more sophisticated system identification methods described in theory, requires expert knowledge in both mathematics and control theory.
6.	The control loop design is specified, but it is not possible to find the control gains in the pump controller cards software due to manufacturers security settings.
7.	Almost all the internal geometry describing the piston barrel and swash plate are unknown, which means they are protected by Bosch Rexroth.
8.	SimulationX handles time delays in an inefficient way. This will slow down the simulation performance drastically, if such features are needed in the non-linear Grey box model.
9.	It is not possible to measure all the internal states in the pump during a frequency response test, due to a maximum of two analog test outputs.

1.2. KEY ASSUMPTIONS AND LIMITATIONS

Table 1.2: Key assumptions and limitations associated with the load circuit design and verification process.

Design and Verification of the Hydraulic Load Take Of Circuit	
Key Assumptions	
1.	A functional test bench which connects the A4VSG closed loop pump to the hydraulic load circuit have to be designed.
2.	All components have to be mechanically mounted and instrumented using a suitable DAQ unit. Also a suitable test program have to be developed using LabVIEW.
3.	Both the load and the supply circuit side have to be analyzed in terms of linearized dynamical behavior. This is necessary to design a sufficient control system controlling each side.
4.	The two control systems controlling the connecting shaft velocity and the load pressure respectively have to be tuned and tested in real life.
5.	The friction in both the motors combined have to be identified and implemented in the SimulationX model of the load circuit.
6.	The SimulationX model have to be verified by comparing the simulation and real life experiments.
7.	A small scale simulation of an offshore AHC have to be developed. The test bench shall be used to reproduce such scenario in real-life.
Associated Limitations	
1.	The load circuit should be designed using mainly hydraulic components which is frequently used by MacGregor.
2.	All the components are not present at the project start, and have to be ordered. Such orders may fail, and create a delay in the project progress.
3.	The components used are not fully described in terms of both dynamic and static behavior.
4.	If non-linear components such as a servo valve is introduced, a linear control system may not be an ideal solution.
5.	The friction may be hard to measure, since it depends on many unknown soft physical parameters.
6.	Due to lack of precise component models, the SimulationX model may not be sufficiently accurate.
7.	Due to further implementation in a PLC, the AHC simulation have to be simplified, since complex simulations may not run real-time on a PLC.

1.3 Design Criteria

The accuracy of a Grey or Black box model is assessed in Section 2.7 in time and frequency domain. The accuracy is determined with a mean and maximum deviation between measurements and simulations. In the frequency domain, the requirements for the model in terms of magnitude and phase deviations are shown in Table 1.3.

Table 1.3: Performance criteria of models in the frequency domain.

Description	Criteria	Upper Limit	Unit
Mean magnitude deviation	\bar{E}_M	0.5	dB
Maximum magnitude deviation	$E_M^{(max)}$	2	dB
Mean phase deviation	\bar{E}_P	5	deg
Maximum phase deviation	$E_P^{(max)}$	35	deg

In the time domain, the requirements are given in Table 1.4.

Table 1.4: Performance criteria of models in the time domain.

Description	Criteria	Upper Limit	Unit
Mean error	\bar{E}_t	2	%
Maximum error	$E_t^{(max)}$	10	%

The load pressure and speed controllers on the load circuit and supply circuit must be able to remove all steady-state error on a step input. The requirements were found through discussions with MacGregor, and the criteria must be fulfilled in a model for it to be verified.

1.4 Report Structure

This section presents a short summary of each chapter to give an overview of the master thesis. Each chapter is described using the following bullet points:

- **Chapter 1 - Introduction**

This chapter presents the problem statement together with the main motivation. The key assumptions and limitations briefly list the expected outcome and the corresponding considered limitations. In the end, the main verification criteria in terms of average and maximum model deviations are presented.

- **Chapter 2 - Method**

The Method chapter presents the different methods used to test and analyze the various hydraulic components. All the analytical methods used to analyze and process the measured data are also explained. If the reader is familiar with least squares techniques, optimization and frequency response analysis related to system identification techniques, this chapter can be skipped.

- **Chapter 3 - Hydraulic Pump Model**

In this chapter all the governing equations needed to describe the pump dynamics using a Grey box model are presented. The ripple flow effect which is caused by the internal piston movement in the pump is analyzed, and a simplified model is proposed. A SimulationX model describing the A4VSG pump is described in the end.

- **Chapter 4 - Results from Hydraulic Pump Model**

All the experimental results related to the hydraulic pump model are presented here. The results are mainly given as optimized model parameters and transfer function coefficients. This section also compares the results against the design criteria given in Tables 1.3 and 1.4.

- **Chapter 5 - Hydraulic Load Simulation Circuit**

A hydraulic load circuit is presented here. The physical construction is discussed and the corresponding mathematical models for both the load and the supply side are presented in this chapter. Suitable control systems and a non-linear friction model are proposed. In the end a complete SimulationX model is described.

- **Chapter 6 - Results from Hydraulic Load Simulation Circuit**

The resulting control parameters describing the control systems introduced in Chapter 6 are presented here. The mapped friction torque is presented and the accompanying friction model parameters are presented. In the end a time domain comparison between the SimulationX model and the physical test set up is presented.

- **Chapter 7 - Discussion and Conclusions**

In this chapter our main conclusions and findings are elaborated.

Chapter 2

Method

This chapter presents the main methods used in this master project. These methods are used when applicable in the main body of the report and will be referenced when necessary. Section 2.1 covers the various reference signals used to test the physical system in different ways. These include a frequency response test, a chirp signal and a stochastic wave. In Section 2.2 an effective least squares method used to fit an analytical sine curve to noisy measurements is presented. Further, Section 2.3 describes a procedure for identifying the linear dynamics of a plant in the frequency domain using a frequency response analysis. Using the frequency response data, Section 2.4 covers the software used to identify a linear transfer function of the plant. A frequency response test and analysis isn't the only way of identifying the dynamics of a plant in the frequency domain; Section 2.5 presents a new method of identifying the dynamics based on the response of a chirp signal test. Section 2.6 explains the algorithm and techniques used to determine parameters for a non-linear model. Based on the identified model, the accuracy is determined using techniques in Section 2.7.

2.1 Considered Test Types

This section describes three different input signals frequently used. The first one is a frequency response test which is the prerequisite for performing a frequency response analysis. The second is a description of a chirp signal that is a multi-cycle sine wave based signal that have a continuously increasing frequency. The last test input signal is a stochastic wave used to test various frequencies on a system.

2.1.1 Frequency Response Test

A frequency response test is a method for measuring the plant response when subjected to sine waves with various frequencies. It is the prerequisite for performing a frequency response analysis that identifies the linear responses in the frequency domain. In order to perform a frequency response test on a system, a user defined sine wave signal is used as the reference signal. The response of the system is measured for further analysis. The sine wave is given in Equation (2.1).

$$y^{(ref)} = A \sin(2\pi ft) + O \quad (2.1)$$

- where:
- $y^{(ref)}$ Input signal to the system.
 - A Amplitude of the input sine wave.
 - f Frequency of the input sine wave.
 - O Offset of the input sine wave.
 - t The time.

For the frequency response tests in this project, test frequencies of the sine waves are chosen to be between 0.1 and 30 Hz to fully investigate the entire dynamic range. A typical test procedure is shown in Figure 2.1:

1. The input reference starts at 0% for half a second before it is ramped to the desired offset. The signal is kept constant at this offset for a second to stabilize the system.
2. At $t = 2$ seconds, the sine wave is used as input around the desired offset, and the measurement system starts to measure the input signal and the response. This happens between the two stapled lines.
3. After several sine wave periods, the sine wave stops and the measurement service stops. Then the reference signal is ramped down to 0%.
4. For the next sine wave frequencies, the entire process is repeated.

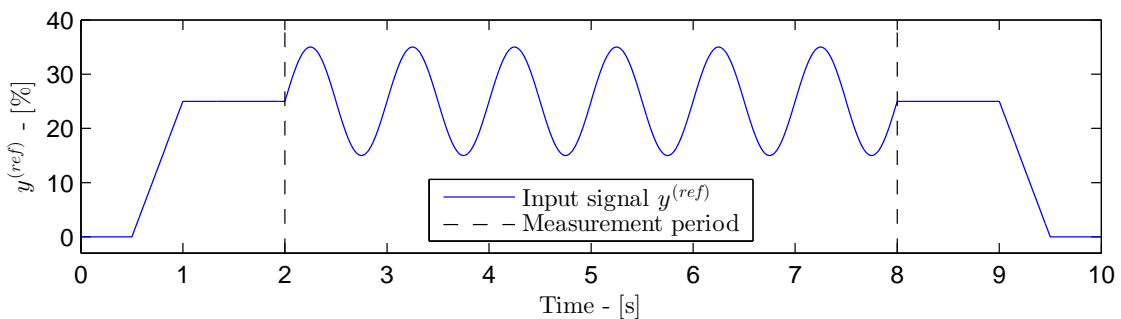


Figure 2.1: Typical reference input signal used in a frequency response test.

2.1.2 Chirp Signal Test

A chirp signal is a multi-cycle sine wave based signal that have a continuously increasing frequency. The linearly increasing frequency chirp signal is defined in Equation (2.2).

$$y_{chirp}^{(ref)} = A_C \sin \left[2\pi \left(f_0 + \frac{k_{chirp}}{2} t \right) t \right] + O_C \quad (2.2)$$

- where:
- $y_{chirp}^{(ref)}$ Chirp signal.
 - A_C Amplitude of the chirp signal.
 - f_0 Initial frequency of the chirp signal.
 - t The time.
 - k_{chirp} The frequency ramp gradient.
 - O_C Offset of the chirp signal.

The frequency ramp gradient is given by Equation (2.3)

$$k_{chirp} = \frac{f_1 - f_0}{t_1} \quad (2.3)$$

- where:
- f_1 Final frequency of the chirp signal.
 - t_1 The time where the sine wave frequency reaches f_1 .

This signal is used to uncover the frequency response of a system from a single test as described in Section 2.5.

2.1.3 Stochastic Wave Test

In order to test the system response during different sine wave frequencies to get a general idea of the dynamic response, a stochastic wave is used as an input to the system. The theory behind stochastic waves is given in Appendix A. In this test, a stochastic wave spectra is first generated based on a significant wave height H_S and a significant wave period T_S . From this spectra, a stochastic signal is generated and used as input to the system. This input reference can be used to verify time responses of a model.

2.2 Sine Fitting using Least Squares Method

The measured data from the frequency response test described in Section 2.1.1 contains measurement noise. The measured sine wave, describing the system frequency response can be processed by a filtering process. However, using a filter will introduce an additional phase lag which also have to be considered. A backward-forward filtering process should be applied if the data should keep the original phase. This is a time consuming process and the result is still in the form of a data set where the phase and magnitude have to be found by comparing the input and output curves.

A more sophisticated method to find the response is to fit an analytical sine wave to the noisy measurements [11]. The analytical sine wave is expressed using Equation (2.4).

$$\hat{y}(t) = \hat{A} \sin(2\pi ft + \hat{\phi}) + \hat{O} \approx y(t) \quad (2.4)$$

where: $\hat{y}(t)$ Estimated system response.

$y(t)$ Measured system response.

f Current test frequency.

\hat{A} Estimated amplitude of the sine wave.

$\hat{\phi}$ Estimated phase angle of the sine wave.

\hat{O} Estimated offset of the sine wave.

t Time.

The sine wave is expressed in a more convenient form by expanding the equation using the sum difference formula. The expanded form is given in Equation (2.5).

$$\hat{y}(t) = \hat{A} \cos(\hat{\phi}) \sin(2\pi ft) + \hat{A} \sin(\hat{\phi}) \cos(2\pi ft) + \hat{O} \quad (2.5)$$

This expression is decomposed and described using a matrix form given by Equation (2.6).

$$\underbrace{\begin{bmatrix} \hat{y}(0) \\ \vdots \\ \hat{y}(t) \end{bmatrix}}_{\vec{b}} = \underbrace{\begin{bmatrix} 0 & 1 & 1 \\ \vdots & \vdots & \vdots \\ \sin(2\pi ft) & \cos(2\pi ft) & 1 \end{bmatrix}}_{\mathbf{A}} \underbrace{\begin{bmatrix} \hat{A} \cos(\hat{\phi}) \\ \hat{A} \sin(\hat{\phi}) \\ \hat{O} \end{bmatrix}}_{\vec{c}} \quad (2.6)$$

The unknown vector \vec{c} is finally solved using a Least Squares method [12]. The solution vector \vec{c} is found by solving Equation (2.6) in the form of Equation (2.7).

$$\vec{c} = (\mathbf{A}^T \mathbf{A})^{-1} \mathbf{A}^T \vec{b} \quad (2.7)$$

Since the approximated sine $\hat{y}(t)$ should mimic the test data $y(t)$, \vec{b} is swapped with $y(t)$. Then Equation (2.7) is solved. The result is given by numerical values for the three components in vector \vec{c} . These three numerical values are used to find the estimated sine wave parameters. The parameters are given by the three Equations: (2.8) to (2.10).

$$\hat{A} = \sqrt{c_1^2 + c_2^2} \quad (2.8)$$

$$\hat{\phi} = \tan^{-1} \left(\frac{c_2}{c_1} \right) \quad (2.9)$$

$$\hat{O} = c_3 \quad (2.10)$$

where: c_i Element i in vector \vec{c} .

The result of this method is a set of parameters that represents an optimized fit of the analytical sine wave. An illustration of the fitted sine wave and the measured signal is given by Figure 2.2.

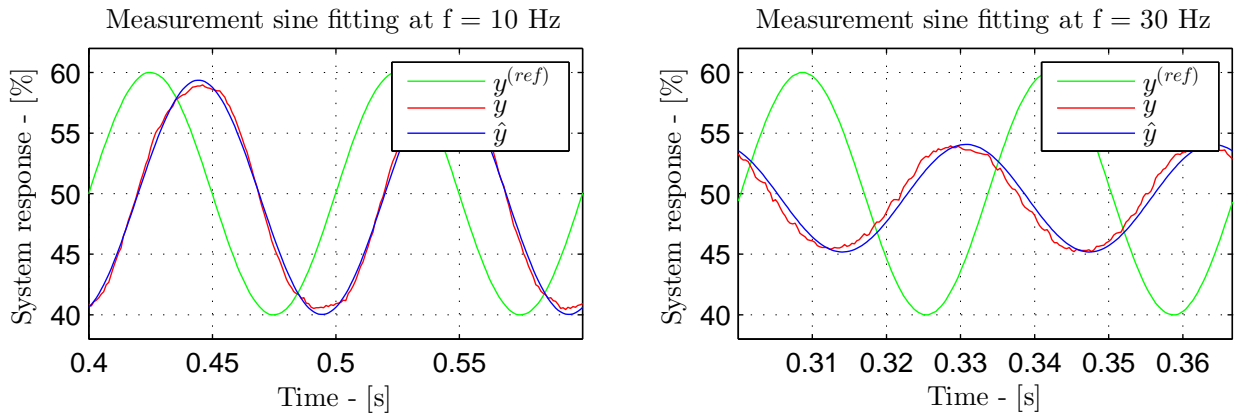


Figure 2.2: Reference signal, measured and fitted system response input frequencies at 10 and 30 Hz.

2.3 Frequency Response Analysis

After a frequency response test as described in Section 2.1.1 is finished, the measured response is analyzed to identify the dynamic characteristics in the frequency domain. During such a test, sine waves at different frequencies are used as reference signals, and the actual response is measured. The name of the log files contain the frequency tested and the contents are three columns: time, reference signal and measured response. A MATLAB script analyzes all the log files individually in an increasing frequency order. For each file, time, reference signal and the measured response are loaded into memory as $t, y^{(ref)}$ and y respectively. Since y contains some measurement noise, a sine wave is fitted on top of the measured data using a least squares method described in Section 2.2.

After the sine wave is identified using the least squares method described in Section 2.2, the approximated system response \hat{y} is given by Equation 2.11:

$$\hat{y} = \hat{A} \sin(2\pi ft + \hat{\phi}) + \hat{O} \quad (2.11)$$

where: \hat{A} Amplitude of the optimized sine wave

f Current test frequency

$\hat{\phi}$ Phase angle of the sine wave

\hat{O} Offset of the sine wave

Figure 2.2 shows examples at $f = 10\text{Hz}$ and $f = 30\text{Hz}$ including reference signal, measured response and approximated system response. The green signal is the input signal, the red signal is the measured response and the blue signal is the approximated response based on a sine wave. The reference signal is a sine wave with 50% offset and 10% amplitude. These examples show that the approximated response \hat{y} is very close to the measured response y and should therefore be a good approximation. The phase and amplitude of the approximated response can therefore with acceptable precision be used to calculate the measured magnitude and phase.

If the analyzed test frequency is $f = 0.1\text{Hz}$, the amplitude of the approximated response is stored in a variable $\hat{A}_{@0.1\text{Hz}}$. This amplitude reference is used to calculate the gain of the system to get a bode plot that starts at 0 dB. This is a fair reference because the actual angle should be equal

to the reference angle at low frequencies as shown in Figure 2.3a. As the frequency of the input signal is increased, the phase and amplitude difference between the input and output signal gets larger as shown in Figure 2.3b. This is the basis for mapping the dynamic response in a bode plot.

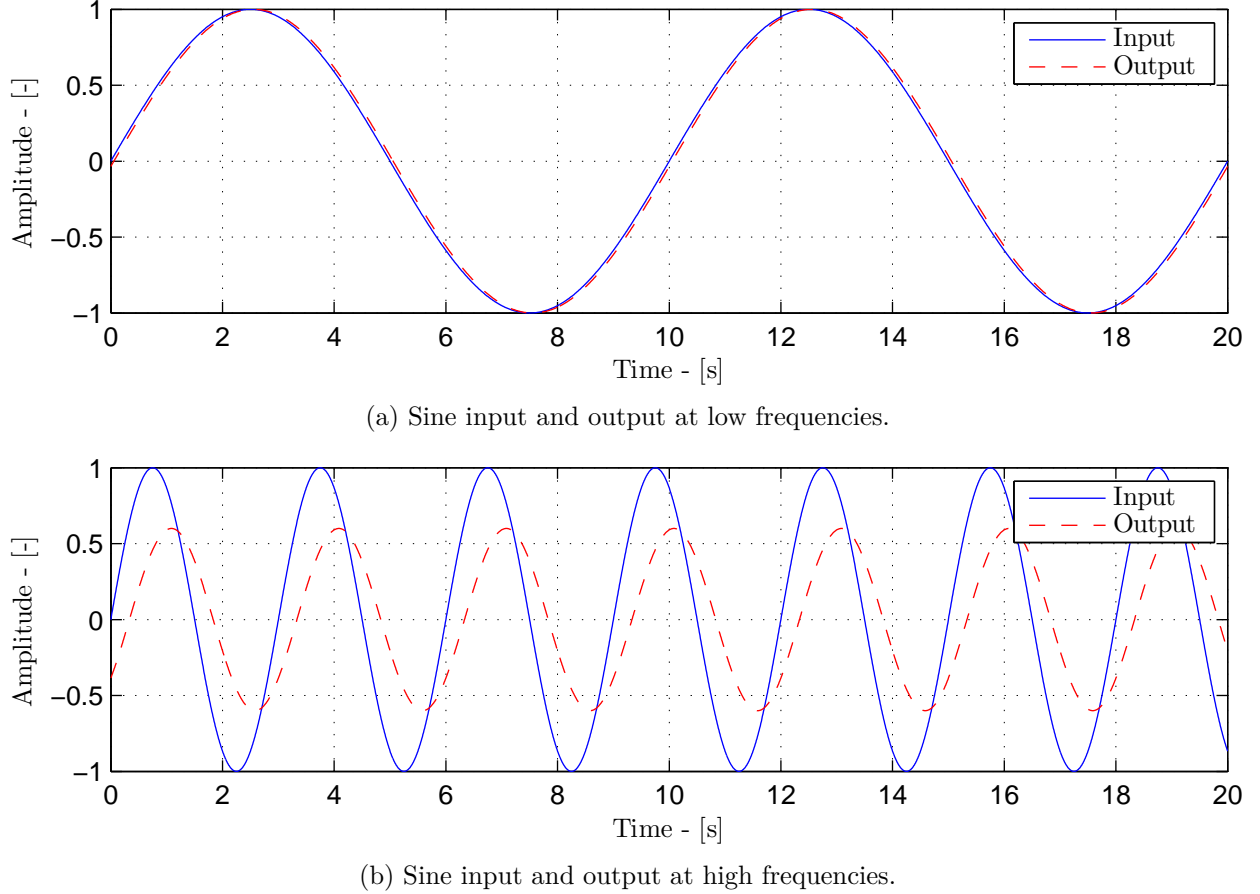


Figure 2.3: Sine input and output at low and high frequencies.

Next the magnitude of the plant is calculated the following Equation 2.12:

$$M_f = 20 \log_{10} \left(\frac{\hat{A}}{\hat{A}_{@0.1Hz}} \right) \quad (2.12)$$

where: M_f Magnitude of the system at a given frequency.

$\hat{A}_{@0.1Hz}$ Amplitude of the optimized sine \hat{a} at $f = 0.1Hz$.

and the phase of the plant is given by Equation (2.13)

$$\phi_f = \hat{\phi} \quad (2.13)$$

This information is used to generate a bode plot of the system response which characterize the systems behavior around the tested offset and amplitude. An example of a bode plot generated from a test at 50% offset and 10% amplitude is shown in Figure 2.4.

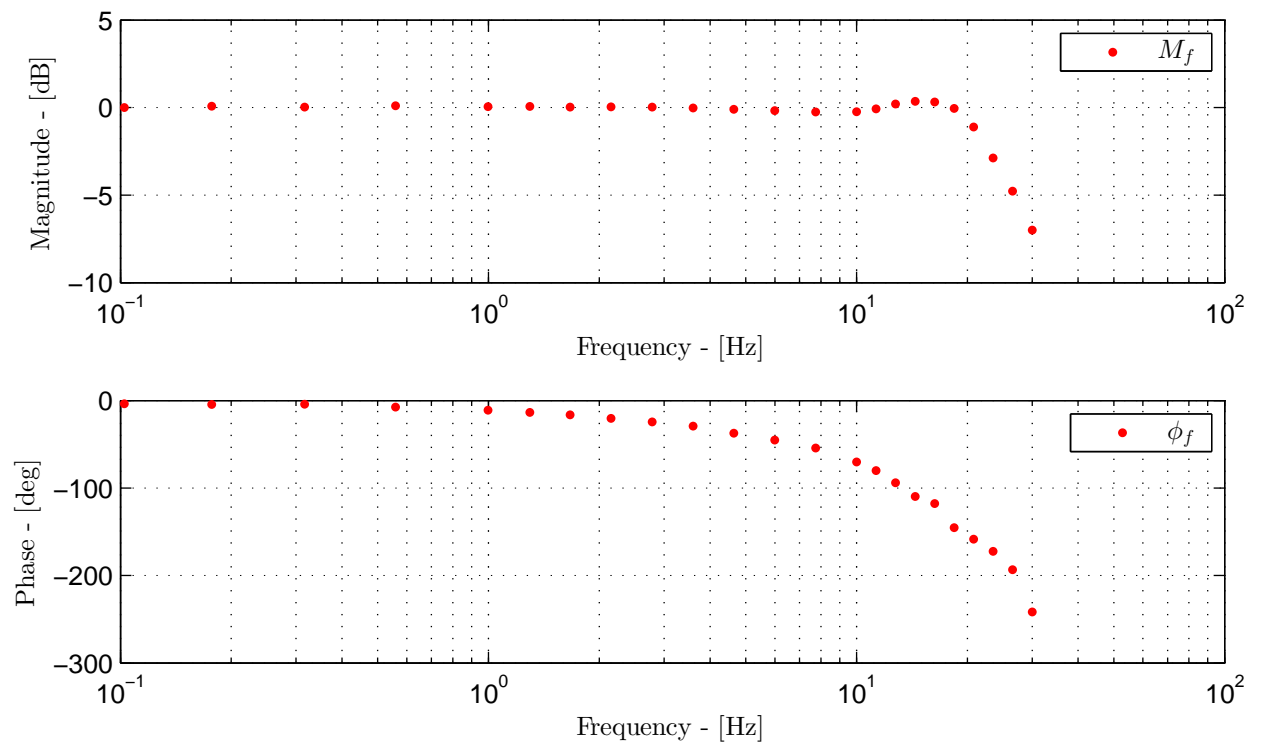


Figure 2.4: Example of a bode plot at 50% offset and 10% amplitude.

2.4 Black Box Transfer Function Estimation

It is desirable to identify a time continuous Transfer Function (TF) by using the results from Section 2.3. MATLAB is used to estimate a TF that matches the frequency response data in a best possible way. This functionality is included in MATLAB's "System Identification Toolbox" and the considered tool is named "System identification tool". This tool requires the user to import a set of three vectors including magnitude, phase and frequency of the test data and the desired number of poles and zeros in the estimated TF. This is the only information required to estimate a transfer function. After the estimation is finished, the output is an estimated TF and a fit percentage describing how good the fit is. More information about the tool is given in Appendix B. For a TF with 5 poles and no zeros, the TF is given by Equation (2.14).

$$G_{est}(s) = \frac{b_0}{s^5 + a_4 s^4 + a_3 s^3 + a_2 s^2 + a_1 s + a_0} \quad (2.14)$$

where: b_0 Constant value describing the TF numerator.

$a_4 \dots a_0$ Constant value describing the TF denominator.

A comparison between an estimated fifth order TF and actual test data is shown in Figure 2.5. The test data shown in red dots are found from a frequency response analysis at 50% offset and 10% amplitude. This estimated TF shown as a blue line has a percentage fit of 89.81% which indicates a good estimation.

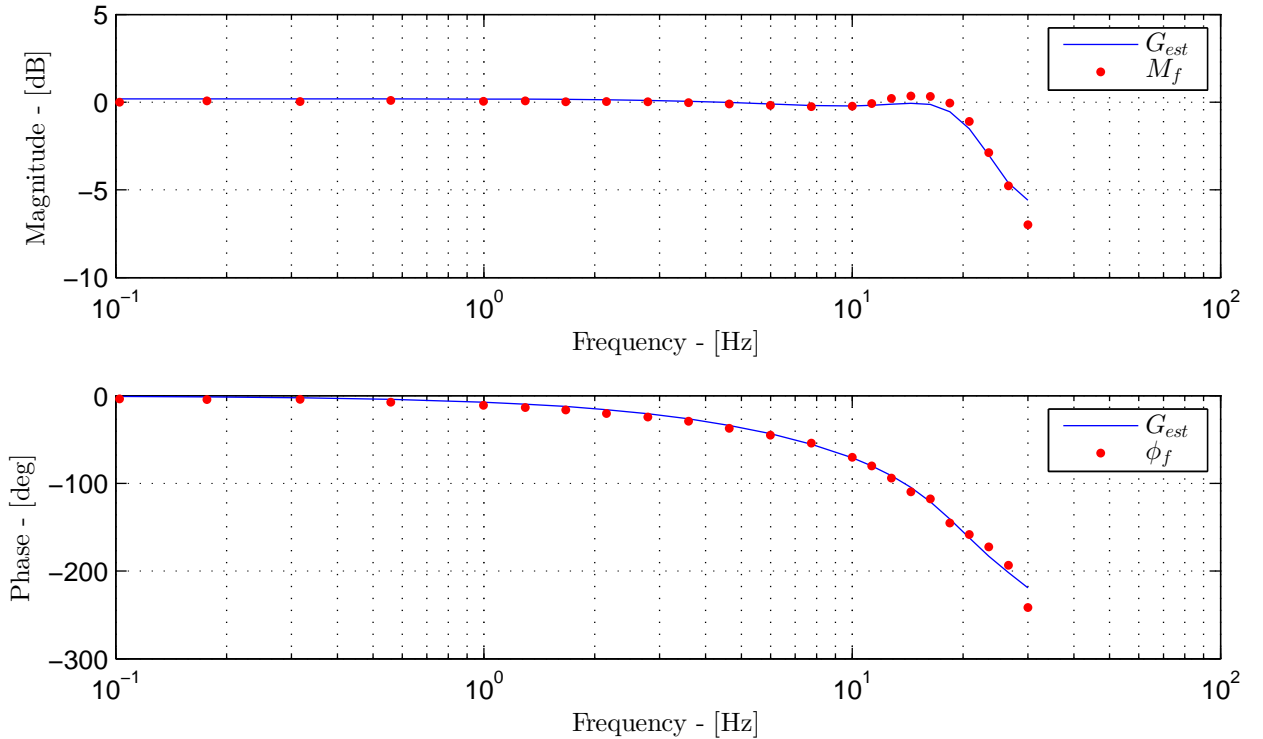


Figure 2.5: Comparison between an estimated TF and discrete frequency response test.

2.5 Frequency Response Analysis using Chirp Signal

In this section a second method is presented to estimate the frequency response of a system based on a linear chirp signal input test. The chirp signal is defined in Section 2.1.2 and it is a continuous sine signal with a linearly increasing frequency as time passes. Since the system responds to all the frequencies in the chirp signal, it should be possible to make a bode plot of the system based on the response. In this section the new method is described and it is compared with a traditional frequency response analysis to verify its performance.

At first a signal $y_{chirp}^{(ref)}$ that consist of a chirp signal as described in Section 2.1.2 is sent to a plant and the response is measured and stored as $y(t)$. During the chirp signal, the performance of the response decreases as the frequency increases. This is observable on the responding amplitude and phase. The following text will describe the algorithm as shown in Figure 2.6.

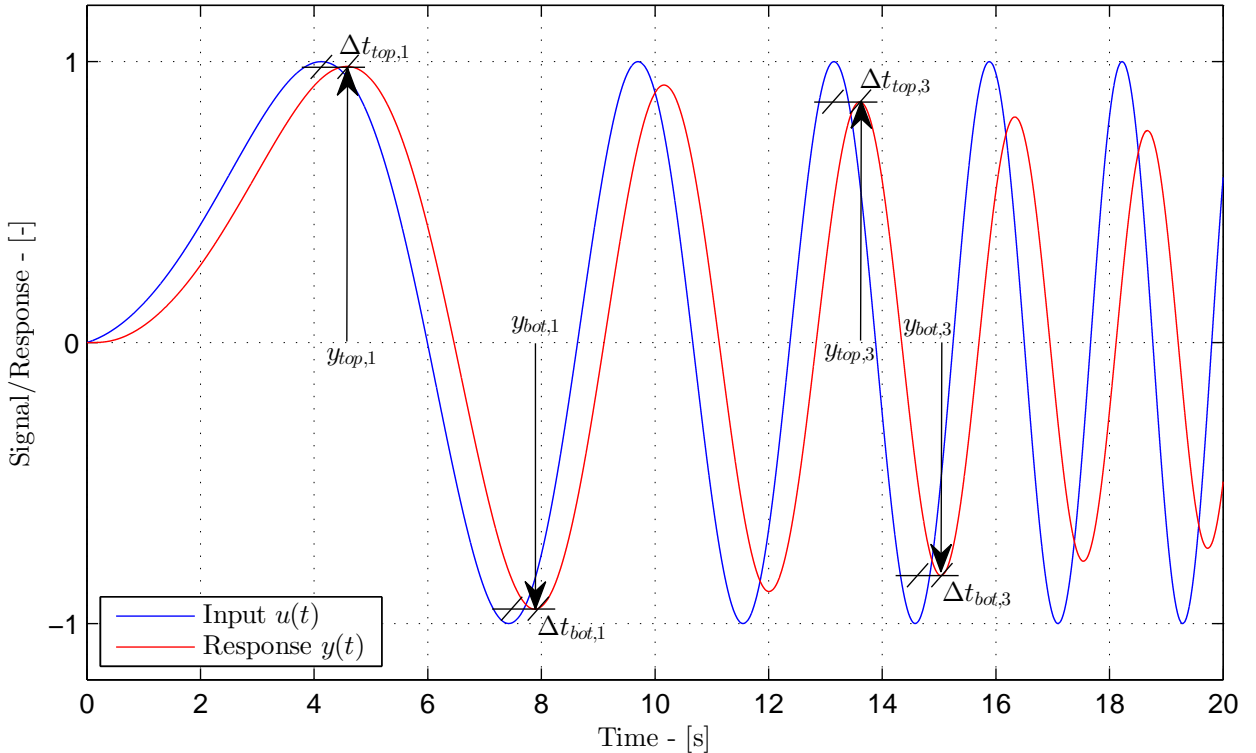


Figure 2.6: Illustration of chirp test analysis.

The algorithm starts by iterating its way through $y(t)$ until it reaches a top (i.e. the highest point between two x-axis intersections) and saves the response into memory as $y_{top,1}$. From this point of time, $y_{chirp}^{(ref)}(t)$ is iterated backwards in time until itself reaches a maximum point. Using the time of maximum response and input signal, a time lag is observed and saved into memory as $\Delta t_{top,1}$. This process is repeated for the next maxima which is a bottom response as displayed by $y_{bot,1}$ and $\Delta t_{bot,1}$. For the next top, the index number increases from 1 to 2 as shown by the index 3 used on the third top and bottom. After the algorithm finishes locating all the bottoms and tops, the gain and phase of the plant is calculated. Since a frequency response analysis is often conducted at various offsets to investigate nonlinearities in the plant, the response may not be symmetrical around the offset of the input signal. This is easily corrected in a regular frequency response analysis as the responding offset is always optimized to find an analytical sine wave. However in this algorithm,

the asymmetries are countered by calculating a mean phase and magnitude from two consecutive tops and bottoms. The magnitude of the top and bottom values of the chirp response, as well as the mean magnitude is calculated in Equations (2.15), (2.16) and (2.17) respectively.

$$M_{top,i} = 20 \log_{10} \left(\frac{y_{top,i}}{A_C} \right) \quad (2.15)$$

$$M_{bot,i} = 20 \log_{10} \left(\frac{y_{bot,i}}{A_C} \right) \quad (2.16)$$

$$M_{C,i} = \frac{M_{top,i} + M_{bot,i}}{2} \quad (2.17)$$

- where:
- $M_{top,i}$ Magnitude of the top chirp response.
 - $M_{bot,i}$ Magnitude of the bottom chirp response.
 - $M_{C,i}$ Mean magnitude of the chirp response.
 - $y_{top,i}$ Response at positive peak i .
 - $y_{bot,i}$ Response at negative peak i .
 - O_C Offset of the chirp signal.
 - A_C Amplitude of the chirp signal.

The phase of the top and bottom values of the chirp response, as well as the mean phase is calculated in Equations (2.18), (2.19) and (2.20) respectively.

$$P_{top,i} = -\Delta t_{top,i} f_{top,i} \cdot 360^\circ \quad (2.18)$$

$$P_{bot,i} = -\Delta t_{bot,i} f_{bot,i} \cdot 360^\circ \quad (2.19)$$

$$P_{C,i} = \frac{P_{top,i} + P_{bot,i}}{2} \quad (2.20)$$

- where:
- $P_{top,i}$ Phase of the top chirp response.
 - $P_{bot,i}$ Phase of the bottom chirp response.
 - $P_{C,i}$ Mean phase of the chirp response.
 - $\Delta t_{top,i}$ Time lag between input and response positive peak i .
 - $\Delta t_{bot,i}$ Time lag between input and response negative peak i .
 - $f_{top,i}$ Frequency of the input signal at time of positive input signal peak i .
 - $f_{bot,i}$ Frequency of the input signal at time of negative input signal peak i .

And finally the frequency at the mean magnitude and phase is calculated in Equation (2.21).

$$f_{C,i} = \frac{f_{top,i} + f_{bot,i}}{2} \quad (2.21)$$

- where: $f_{C,i}$ Frequency of magnitude $M_{C,i}$ and phase $P_{C,i}$.

From a test at 75% offset and 20% amplitude, the frequency response was identified using a standard frequency response analysis as described in Section 2.1.1 and a chirp signal frequency response analysis as described in this section. The identified dynamics from the standard frequency response analysis is assumed to be correct and is therefore the reference in order to validate the performance of the chirp frequency response analysis. The comparison is shown in Figure 2.7 where the black

dots shows the dynamics from a standard frequency response analysis, the blue line shows the mean response and the green and red lines shows the top and bottom responses respectively.

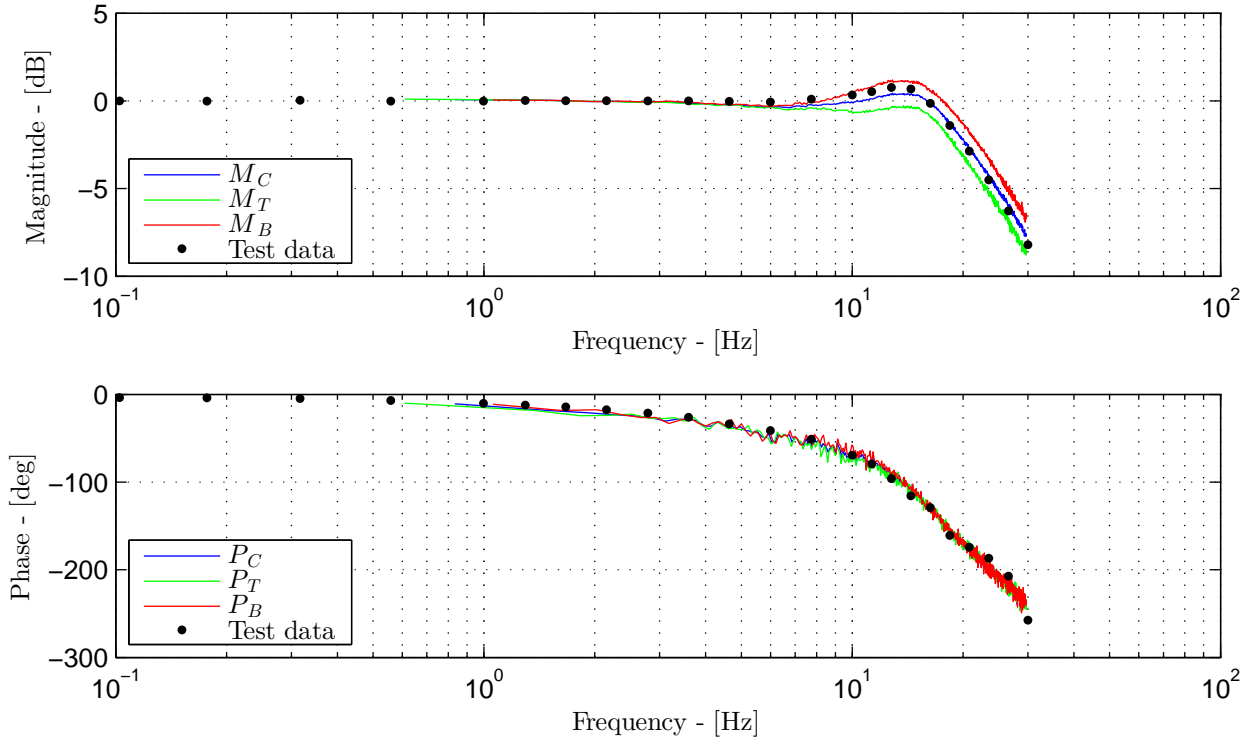


Figure 2.7: Bode plot comparison between frequency response analysis and chirp response analysis.

As shown in the figure the black dots and the blue line are almost identical, which proves the performance of the proposed algorithm. This means that the frequency response of a plant can be identified using just one signal input test, i.e. a chirp signal moving through the frequency range of the plant. Note however that the green and red line form an envelope around the frequency response test data, and that the red line gives the best response in the magnitude plot. This indicates that for the plant that it's easier to move towards zero (From +75% offset to 0%) than from zero. This should be the case in this system as a mechanical spring drags the cylinder back to zero position. This gives a second usage of this algorithm as directional based dynamics may also be identified.

2.6 Parameter Estimation

This section presents the techniques used to identify unknown parameters in non-linear models. Several methods for system identification are available in the theory, and one of the simple and popular methods are based on linear regression techniques. However, the models presented in this report includes both linear and non-linear relationships. Therefore a gradient based minimization algorithm have been chosen to determine unknown parameters. The optimization algorithm, as well as three different optimization objectives are presented in the following subsections.

2.6.1 Non-Linear Optimization Algorithm

The numerical optimization problem encountered when searching for optimal parameters in a model is classified using Equation (2.22) :

$$\arg \min_{\vec{\Phi}} f(\vec{\Phi}) \text{ subject to } \vec{L}_b \leq \vec{\Phi} \leq \vec{U}_b \quad (2.22)$$

where: $\vec{\Phi}$ Parameter vector.

$f(\vec{\Phi})$ Objective value with a certain parameter vector.

\vec{L}_b Lower linear bounds of $\vec{\Phi}$

\vec{U}_b Upper linear bounds of $\vec{\Phi}$

As mentioned in the preliminary of this section, the choice of optimization algorithm is a gradient based one named the *Interior-point* algorithm [13, 14, 15]. This algorithm minimizes a *logarithmic barrier* function rather than the objective function itself. The barrier function is given by Equation 2.23.

$$B(\vec{\Phi}, \mu) = f(\vec{\Phi}) - \mu \left(\sum_{i=1}^m \ln(U_{b,i} - \Phi_i) + \sum_{i=1}^m \ln(\Phi_i - L_{b,i}) \right) \quad (2.23)$$

where: $B(\vec{\Phi}, \mu)$ Barrier function.

μ Small positive scalar often called the “barrier parameter”.

i Implies element i in the given vector.

m Length of the vector.

As μ converges to zero, the minimum of $B(\vec{\Phi}, \mu)$ should converge to a solution of the minimization problem. From an initial guess of $\vec{\Phi}$, the gradient of the barrier function is evaluated at every iteration. By using this gradient, the algorithm determines which direction it should travel in terms of $\vec{\Phi}$. Since the barrier function $B(\vec{\Phi}, \mu)$ should be minimized, the negative gradients are chosen. The algorithm tries to find $(\vec{\Phi}, \mu)$ for which the gradient of the barrier function is zero, i.e. a local minima. At this point the algorithm stops and present the resulting parameters in $\vec{\Phi}$. More detailed information about the algorithm is found in the referenced articles [13, 14, 15].

2.6.2 Optimization Objective Functions

In Section 2.6.1 an interior point optimization algorithm was briefly discussed. This algorithm requires an objective function describing the error between a simulated model and measurements. The idea behind the objective function is illustrated with a simple block diagram given by Figure 2.8.

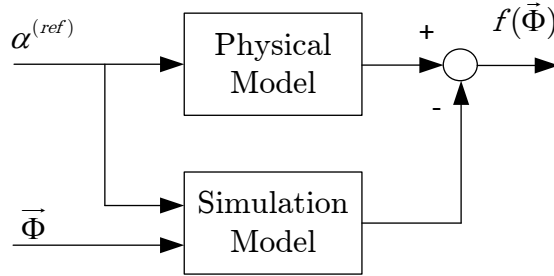


Figure 2.8: Schematic illustration of the optimization objective.

Figure 2.8 illustrates that the objective function $f(\vec{\Phi})$ is found by comparing the response between the physical model and the simulated model. The error is quantified using three main techniques given as:

1. Pure time domain. The deviations are described by comparing the time domain signals in the model. The objective function is described using Equation (2.24).

$$f_{\text{time}}(\vec{\Phi}) = \sum |\vec{y} - \vec{y}_{\text{sim}}| \quad (2.24)$$

where: $f_{\text{time}}(\vec{\Phi})$ Time domain objective function.

\vec{y} Measured system response.

\vec{y}_{sim} Simulated system response.

2. Pure frequency domain. This method sum up the difference between the measured and simulated magnitude and phase lag in all test frequencies. The objective function is given by Equation (2.25).

$$f_{\text{freq.}}(\vec{\Phi}) = \frac{90}{20} \sum |\vec{M} - \vec{M}_{\text{sim}}| + \sum |\vec{\phi} - \vec{\phi}_{\text{sim}}| \quad (2.25)$$

where: $f_{\text{freq.}}(\vec{\Phi})$ Frequency domain objective function

\vec{M} Measured response magnitude.

$\vec{\phi}$ Measured response phase.

\vec{M}_{sim} Simulated response magnitude.

$\vec{\phi}_{\text{sim}}$ Simulated response phase.

$\frac{90}{20}$ Weighting factor of magnitude deviations.

3. Combined time and frequency domain error. This method ensures that both time and frequency domain characteristics will fit the measured data properly. The expression describing the combined objective function is expressed using a combination of Equation (2.24) and (2.25). The combined objective function is given by Equation (2.26).

$$f_{\text{comb.}}(\vec{\Phi}) = f_{\text{time}}(\vec{\Phi}) + f_{\text{freq.}}(\vec{\Phi}) \quad (2.26)$$

where: $f_{\text{comb.}}(\vec{\Phi})$ The combined time and frequency domain objective function

All three objective functions can be used to find the unknown parameters in $\vec{\Phi}$. However in this project, the combined time and frequency objective function f_{comb} . is used to identify the unknown parameters. When the optimization algorithm ends up in a local minimum, the model is validated in both time and frequency domain to ensure that the model gives satisfactory results. It is clear that the third method will give the highest probability of finding a set of satisfying model parameters, as it optimizes for both domains at the same time.

2.7 Model Accuracy Verification

To state that the model is within the requirements given in Section 1.2 it is necessary to define an overall method to calculate the deviation between the simulated model and the lab measurements. It is chosen to validate the model in both frequency and time domain. The deviations are quantified in two main categories where the first one is the absolute average deviation which is calculated using Equation (2.27), and the second deviation is the maximum deviation between the lab experiments and the simulated response given in Equation (2.28).

$$\bar{E}_X = \frac{1}{N_s} \sum_{i=1}^{N_s} |\Delta X_i| \quad (2.27)$$

where: \bar{E}_X Average absolute deviation between the experiments and the simulation.

ΔX_i Deviation measurement i between the experiments and the simulation model.

N_s Total number of compared samples.

$$E_X^{(max)} = \max(\Delta \vec{X}) \quad (2.28)$$

where: $E_X^{(max)}$ Maximum deviation between the simulated and the experiments.

$\Delta \vec{X}$ The deviation vector from all the compared samples.

Both these verification procedures are performed in the two results chapters where applicable.

Chapter **3**

Hydraulic Pump Model

This chapter presents a mathematical model of a Bosch Rexroth A4VSG closed loop hydraulic pump. This pump is located in a test container at MacGregor in Kristiansand, Norway. The first Section 3.1 shows an overview of the test setup including instrumentation and physical layout.

On top of the A4VSG pump there is an actuating circuit that controls the swash plate angle. This hydraulic circuit is described using a non-linear mathematical model in Section 3.2. This actuating circuit is controlled using a Bosch Rexroth control card. The control system inside this card is modeled in Section 3.3.

Now that the actuating circuit is covered, the next step is to model all the pistons inside the pump that are attached to the swash plate. The complete kinematics of the piston barrel as well as a simplification of the Ripple flow is presented in Section 3.4. Finally a complete non-linear model of the pump including the actuating circuit and the ripple flow is detailed in Section 3.5.

3.1 Test Setup

This section covers the setup used to test the dynamics of the swash plate angle on the A4VSG closed loop pump. The physical layout of the test bench is described including the hydraulic circuit and wiring schematic. However, a more detailed hydraulic drawing is found in Appendix H. Then a method to measure signals at high speeds using software and hardware from National Instruments is described.

3.1.1 Location

MacGregor is located just outside of Kristiansand in Norway, about 45 minutes in a car from the University of Agder. The test bench is located here inside a blue container. The container is split into three parts:

1. A backside containing a hydraulic supply pump and an oil tank.
2. A middle part accessible from the front containing the A4VSG closed loop pump and the load circuit.
3. A front part with control cabinets, parts and a computer. The front and middle part is separated with plexiglass to maintain the user safety during testing.

3.1.2 Physical Layout

The dynamics of the swash plate angle is tested using a setup shown in Figure 3.1. The figure is explained using the red numbers, corresponding to the list below the figure. Most of the components are also described in detail in Appendix D, and references to the different sections within are given in parentheses after the respective component is mentioned. This physical layout will be used on all tests of the pump.

3.1. TEST SETUP

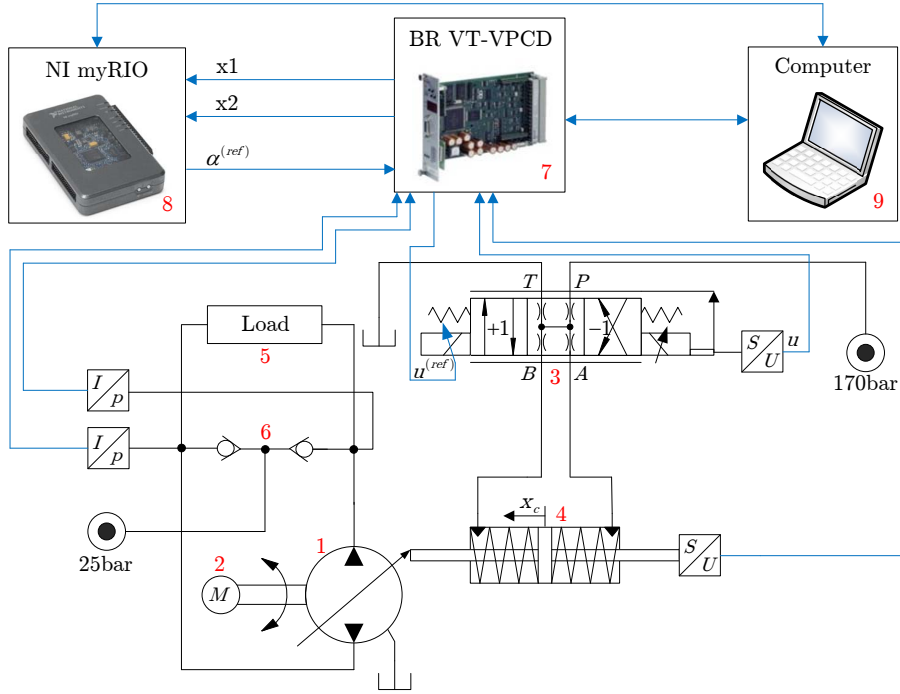


Figure 3.1: Physical test setup. Picture of NI myRIO and BR VT-VPCD are taken from [1] and [2] respectively.

1. The variable displacement axial piston closed loop pump (1) is a Bosch Rexroth A4VSG pump (Appendix D.1) with a theoretical maximum displacement of $71\text{cm}^3/\text{rev}$.
2. The pump is driven by a 4-pole induction motor (2) set at a constant speed of 1450rpm .
- 3-4. In order to control the displacement, a 4/3-way valve (3) (Appendix D.2) is manipulated to achieve a desired position on a symmetrical cylinder (4) (Appendix D.2) which directly controls the swash plate angle.
5. The pump (1) is connected to a load (5) on both sides which could include nothing (no load), an orifice, a flow sensor (Appendix D.7) or a Parker V12-060 motor (Appendix D.4).
6. In between the load and the pump, there is a refill solution (6) which keeps the pressures on either side at a minimum of 25 bar. There are also two pressure transmitters (Appendix D.8) on each side of the pump.
7. The Bosch Rexroth pump controller card (7) (Appendix D.3) measures the feedback signals and controls the valve (3).
8. The swash plate angle reference $\alpha^{(ref)}$ is sent from the National Instruments (NI) myRIO (8) (Appendix D.9) to the pump controller card (7). Test jacks x_1 and x_2 on the pump controller card (7) are used to monitor the status of two internal parameters. Usually, test jack x_1 is used to monitor the actual swash plate angle α and test jack x_2 is set to monitor the actual valve position u_p .
9. The computer (9) (Appendix D.10) is used in combination with NI myRIO (8) to manage high speed data transfers through a direct memory access (DMA) channel. The computer also monitors the status of the pump via an RS232 connection on the pump controller card using a program called “Bodac”.

3.1.3 Software Layout

In order to perform a test on the pump, two LabVIEW programs are used. The first program is located on the host computer (hereby called “host”) and the second program is located on the target FPGA (Field Programmable Gate Array) on the NI myRIO (hereby called “target”). The target program contains a routine to send a signal via an analog port and receive analog signals through others. The other purpose of this program is to log the signals into a DMA buffer which the host can read at certain intervals.

The host program initializes the target and decides the shape of the swash plate angle reference. It also stores the measured signals in a textfile so that they can be analyzed. If two test jacks are not enough to measure all the desired signals, the host may also log signals directly from the pump controller via the “Bodac” program. The downside is that the logging frequency is limited to 250 times per second for one signal, and 70 times per second for four signals. This software layout will be used for all tests carried out on the pump.

3.2 Hydraulic Actuating Circuit

3.2.1 Governing Equations

The actuating circuit is modeled based on the schematic in Figure 3.2.

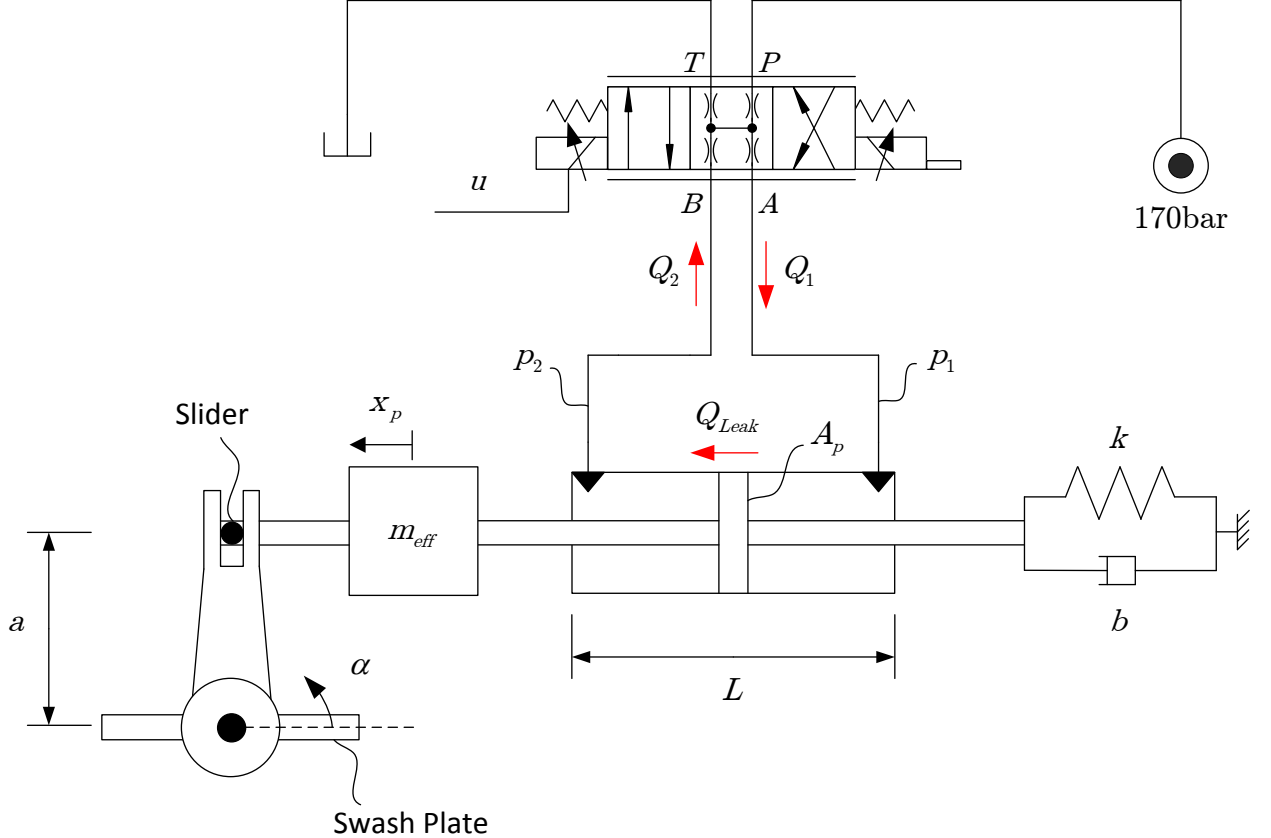


Figure 3.2: Hydraulic actuating mechanism.

The hydraulic circuit consist of a 4/3-way directional proportional valve controlling Q_1 and Q_2 . These two flows affects the two pressures p_1 and p_2 in each of the two control volumes. The swash plate is connected to the piston rod through a linking/sliding mechanism. The governing equations for the actuating circuit is set up in order to analyze the dynamics and simulate the response in the time domain. The two flows are expressed using Equations (3.1) and (3.2):

$$Q_1(p_1, u) = \begin{cases} \text{sign}(p_P - p_1)K(u)\sqrt{\frac{2}{\rho}|p_P - p_1|} & u \geq 0 \\ \text{sign}(p_T - p_1)K(u)\sqrt{\frac{2}{\rho}|p_T - p_1|} & u < 0 \end{cases} \quad (3.1)$$

$$Q_2(p_2, u) = \begin{cases} \text{sign}(p_2 - p_T)K(u)\sqrt{\frac{2}{\rho}|p_2 - p_T|} & u \geq 0 \\ \text{sign}(p_2 - p_P)K(u)\sqrt{\frac{2}{\rho}|p_2 - p_P|} & u < 0 \end{cases} \quad (3.2)$$

- where:
- Q_1 Volume flow into cylinder chamber 1.
 - Q_2 Volume flow out of cylinder chamber 2.
 - p_P Pressure on the P-port.
 - p_T Pressure on the T-port.
 - p_1 Pressure in cylinder chamber 1.
 - p_2 Pressure in cylinder chamber 2.
 - u Valve spool position.
 - $K(u)$ Effective valve opening area.
 - ρ Density of the oil.

The flow area coefficient $K(u)$ is dependent on the actual spool position u . The opening curve is extracted from the proportional valves data sheet [16], and a third order polynomial is fitted using a least squares method. The fitted polynomial describing the flow area $K(u)$ is given by Equation (3.3).

$$K(u) = k_1|u^3| + k_2u^2 + k_3|u| \quad (3.3)$$

where: $k_1 \dots k_3$ Flow area coefficients.

This opening characteristic introduces an additional non-linearity in addition to the non-linear nature of the orifice equation itself. The pressure gradients in each cylinder chamber is expressed using Equations (3.4) and Equation (3.5).

$$\dot{p}_1 = \frac{\beta}{V_0 + A_p x_p} (Q_1(p_1, u) - A_p \dot{x}_p - Q_{Leak}(p_1, p_2)) \quad (3.4)$$

$$\dot{p}_2 = \frac{\beta}{V_0 - A_p x_p} (Q_{Leak}(p_1, p_2) + A_p \dot{x}_p - Q_2(p_2, u)) \quad (3.5)$$

- where:
- \dot{p}_1 Pressure gradient in cylinder chamber 1.
 - \dot{p}_2 Pressure gradient in cylinder chamber 2.
 - β Oil stiffness.
 - V_0 Dead volume on each cylinder side.
 - A_p Cylinder pistons effective area.
 - x_p Cylinder piston position.
 - \dot{x}_p Cylinder piston velocity.
 - Q_{Leak} Leakage flow from cylinder chamber 1 to 2.

Note that the capacitance of the pressure gradients in Equations (3.4) and (3.5) does not include the static $A_p \frac{L}{2}$ part. This part have been removed to increase the freedom of V_0 since some of the volume in the cylinder is occupied with a spring etc. The leakage flow is most probably laminar, but since this flow is small compared to Q_1 or Q_2 , it have been modeled as a turbulent orifice described in Equation (3.6).

$$Q_{Leak}(p_1, p_2) = \text{sign}(p_1 - p_2) K_L \sqrt{\frac{2}{\rho} |p_1 - p_2|} \quad (3.6)$$

where: K_L Effective orifice opening between cylinder chamber 1 and 2.

The linkage mechanism between the cylinder and the swash plate is modeled using a slider mechanism. The mechanism is described using Equation (3.7) and shown in Figure 3.3.

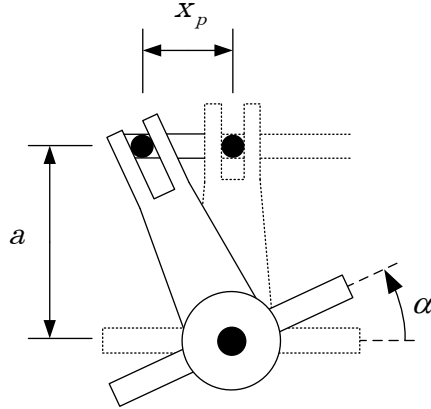


Figure 3.3: Geometry of the sliding connection between the swash plate and the cylinder.

$$x_p = a \tan(\alpha) \quad (3.7)$$

where:
 a Normal distance between the cylinder rod and the swash plate.
 α Swash plate tilt angle.

Since the maximum angle of the swash plate is restrained to be $\pm\alpha_{max}$ it is possible to use Equation (3.7) to find the relationship between the stroke length L and the distance a . The relationship is given by Equation (3.8).

$$a = \frac{L}{2 \tan(\alpha_{max})} \quad (3.8)$$

where:
 α_{max} Maximum swash plate tilt angle.
 L Cylinder stroke length.

The mechanical piston movement can be described using Newton's second law. It should be noted that all the rotational inertia from the swash plate and the attached pistons are included in a combined translational effective mass m_{eff} . The governing differential equation describing the piston acceleration \ddot{x}_p is given by Equation (3.9).

$$\ddot{x}_p = \frac{(p_1 - p_2)A_p - x_p k - \dot{x}_p b}{m_{eff}} \quad (3.9)$$

where:
 \ddot{x}_p Cylinder piston acceleration.
 k Spring coefficient in cylinder.
 b Damping coefficient in cylinder.
 m_{eff} Effective translational mass.

The connection between the actuating cylinder rod and the swash plate is modeled without any mechanical flexibility. By assuming such a connection, the relationship between the piston stroke x_p and the swash plate angle α is described using Equation (3.10).

$$\alpha = \tan^{-1} \left(\frac{x_p}{a} \right) \quad (3.10)$$

By evaluating the derivative of Equation (3.10) with respect to time, the angular velocity $\dot{\alpha}$ is described by Equation (3.11).

$$\dot{\alpha} = \frac{\dot{x}_p(1 + \cos(2\alpha))}{2a} \quad (3.11)$$

where: $\dot{\alpha}$ Swash plate tilt angular velocity.

In the end the angular acceleration can be obtained by differentiating Equation (3.11) with respect to time. The resulting angular acceleration $\ddot{\alpha}$ of the swash plate is given by Equation (3.12).

$$\ddot{\alpha} = \frac{\cos(\alpha)[\cos(\alpha)\ddot{x}_p - 2\dot{\alpha}\sin(\alpha)\dot{x}_p]}{a} \quad (3.12)$$

where: $\ddot{\alpha}$ Swash plate tilt angular acceleration.

3.2.2 Non-Linear State Space Model

All the non-linear differential equations in Section 3.2.1 are here expressed using a non-linear state space model. The non-linear model is given in a compact form by Equations (3.13) and (3.14).

$$\dot{\vec{x}} = f(\vec{x}, u) \quad (3.13)$$

$$\alpha = g(\vec{x}, u) \quad (3.14)$$

where: \vec{x} State vector representing all internal states.

$f(\vec{x}, u)$ State equations.

$\dot{\vec{x}}$ Time derivative of the state vector.

$g(\vec{x}, u)$ Output function.

An overview of the change of variables of each state is given by:

$$\begin{aligned} x_1 &= p_1 & x_3 &= x_p \\ x_2 &= p_2 & x_4 &= \dot{x}_p \end{aligned}$$

where: $x_1 \dots x_4$ The four states in \vec{x} .

By using this change of variables it is possible to construct a non-linear state space model given by Equation (3.15).

$$\dot{\vec{x}} = \begin{bmatrix} \frac{\beta}{V_0 + A_p x_3} (Q_1(x_1, u) - A_p x_4 - Q_{Leak}(x_1, x_2)) \\ \frac{\beta}{V_0 - A_p x_3} (Q_{Leak}(x_1, x_2) + A_p x_4 - Q_2(x_2, u)) \\ x_4 \\ \frac{(x_1 - x_2)A_p - x_3 k - x_4 b}{m_{eff}} \end{bmatrix} \quad (3.15)$$

Where all the flows are described using Equations (3.1), (3.2) and (3.6) where all the states are substituted. The output α is also non-linear and is given by Equation (3.16).

$$\alpha = \tan^{-1} \left(\frac{x_3}{a} \right) \quad (3.16)$$

This non-linear state-space model is solved using softwares like MATLAB, Simulink and SimulationX by applying numerical solving techniques. This model consist of 4 states in total and only includes the states describing the hydraulic actuating piston and the mechanical movement of the swash plate. To complete the simulation model, it is necessary to introduce the dynamics of the directional control valve spool position u , as well as the dynamics of the control circuit. These dynamics are introduced in Section 3.3.

3.3 Microcontroller Control Circuit

The hydraulic pump is operated by a pump controller card as shown in Figure 3.1. It is therefore necessary to identify the control loop and the accompanying control parameters if the complete response should be described. The complete pump model describes the relationship between the swash plate reference angle $\alpha^{(ref)}$ and the actual swash plate angle α . The complete control circuit is illustrated using a simplified block diagram given by Figure 3.4.

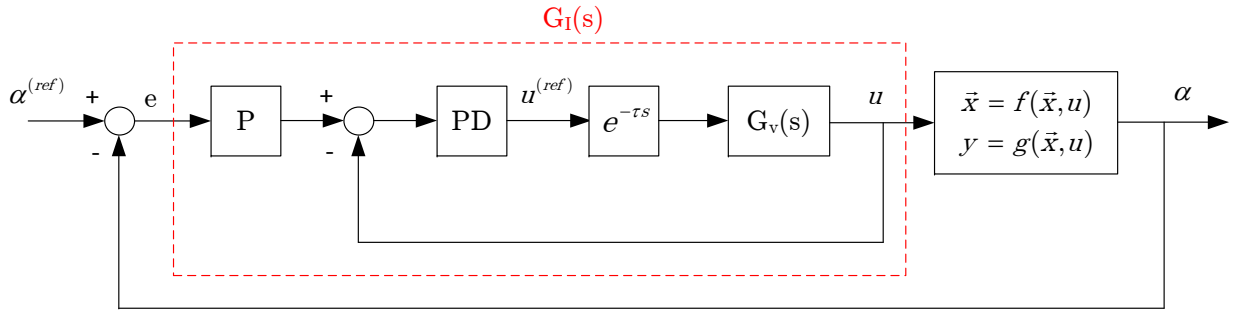


Figure 3.4: Block diagram of the hydraulic circuit and the accompanying control loop.

The control loop in Figure 3.4 consist of two closed loops, where the inner loop introduces a time delay that represents the combined time delay due to the sensors and pump controller card. The inner loop which later will be described using $G_I(s)$ consist of the dynamics of a directional control valve $G_v(s)$ placed in a closed loop with a PD-controller. The error between the reference spool position and actual position is minimized using a classical PD-controller given by Equation (3.17)

$$G_{PD}(s) = (K_d T_d s + K_d) \quad (3.17)$$

where: G_{PD} Transfer function describing the PD-controller.

K_d Proportional gain.

T_d Time constant.

Further the outer loop controls the actual swash plate angle α using a unity feedback, and the error is minimized using a simple P-controller given by Equation (3.18).

$$G_P(s) = K_p \quad (3.18)$$

where: G_P Transfer function describing the P-controller.

K_p Proportional gain.

The valve dynamics is described using a second order transfer function given by Equation (3.19).

$$G_v(s) = \frac{u(s)}{u^{(ref)}(s)} = \frac{\omega_v^2}{s^2 + 2\zeta_v\omega_v s + \omega_v^2} \quad (3.19)$$

where: $G_v(s)$ Transfer function for the valve.

$u(s)$ Actual valve spool position.

$u^{(ref)}(s)$ Valve spool reference signal

ω_v Natural frequency of the valve.

ζ_v Damping ratio of the valve.

These parameters can be found from a frequency response plot of the valve in a catalog, but they are also treated as unknowns since such catalog parameters might not be accurate. By assuming a second order system describing the valve dynamics the control loop is simplified by evaluating the inner loop and describe it using a single transfer function $G_I(s)$. The inner loop is illustrated in Figure 3.4 using the red dotted line, and the corresponding transfer function is given by Equation (3.20).

$$G_I(s) = \frac{u(s)}{e(s)} = e^{-\tau s} \frac{K_p\omega_v^2(K_dT_d s + K_d)}{s^2 + (2\zeta_v\omega_v + K_dT_d\omega_v^2 e^{-\tau s})s + (1 + K_d e^{-\tau s})\omega_v^2} \quad (3.20)$$

where: $G_I(s)$ Inner transfer function.

$e^{-\tau s}$ The time delay transfer function.

$e(s)$ Error between $\alpha^{(ref)}$ and α .

The inner transfer function describes the dynamics from the error $e(s)$ to the actual valve spool position $u(s)$. In the next Section, 3.4, the relationship between the swash plate angle and the output flow is described.

3.4 Internal Pump Model

In this section the relation between the swash plate angle α and the direction and magnitude of the output volume flow is described. First the mechanisms relying on the swash plate angle is described in Section 3.4.1, and also how the hydraulic fluid is transferred across the pump using the pistons inside the pump. In Section 3.4.2, the mechanical movement of each piston as a function of the swash plate angle and input shaft speed is described. The movement of these pistons is the source of pump flow. The final component of producing flow is the opening area between the two pump ports and the pistons as described in Section 3.4.3. This port plate opening model produces a ripple flow that is compared with the mean flow in Section 3.4.4. Since simulating the piston kinematics in the pump is computationally heavy, an empirical simplification of the ripple flow is presented in Section 3.4.5.

3.4.1 Swash Plate Mechanism

The pistons inside the pump are sliding in a cylindrical barrel that rotates around the z-axis. The movement of each piston in their axial direction is manipulated by tilting the swash plate. The swash plate is controlled into a given angle which will move the pistons up and down as the plate rotates around the z-axis. This is the basis for a variable piston pump. The mechanism allows the operator to choose which direction the flow should move and how much per second, even if the driving motor has a fixed speed and direction. An illustration of such a pump is shown in Figure 3.5.

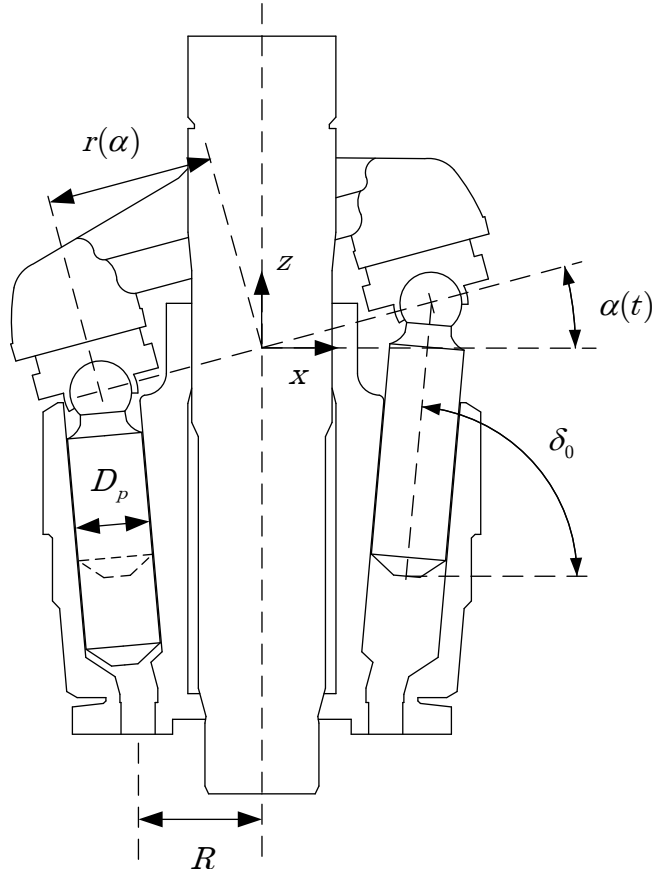


Figure 3.5: Illustration of a variable displacement piston pump.

The pistons are connected via ball joints to the swash plate in a radius $r(\alpha)$ from the axis center. When $\alpha \neq 0$, this spinning movement of the shaft forces the pistons to move in their axial direction. The ones going backward (positive z) sucks oil from one port, and pushes it out through the other port when their axial movement is reversed. The maximum angle determines how far the pistons move, and in the A4VSG pump, the maximum swash plate angle is given by (3.21)

$$\alpha_{max} = \pm 15^\circ \quad (3.21)$$

where: α_{max} Maximum swash plate tilt angle.

Now that the mechanics of the swash plate is described, the next step is to identify how each piston moves as a consequence of the tilt angle. This is important because the movement of each piston is responsible for sucking oil from one port and push it out another. The movement of each piston as a function of the swash plate angle and input shaft rotation velocity is described in Section 3.4.2.

3.4.2 Piston Kinematics

In a steady-state situation, the flow from a pump is often simplified to a mean flow as given by Equation (3.22).

$$\bar{Q} = \omega \frac{\alpha}{\alpha_{max}} V_{d,max} \quad (3.22)$$

where: \bar{Q} Mean steady state flow produced by the pump.
 ω Motoring shaft speed.
 α Swash plate angle.
 $V_{d,max}$ Maximum pump displacement.

However the simplification in Equation (3.22) does not include the ripple flow from the internal pistons. The consequences of pistons moving from one port to another causes a ripple effect in the flow with high frequencies. This effect is often damped out in the first hose, but it could trigger nearby components resonance frequency. Therefore it is desirable to model and simulate this behavior. The axial movement of piston n is given by the following vector loop as shown in Figure 3.6 and described in Equation (3.23).

$$\vec{r}_{0,n} + \vec{x}_{p,n} - \vec{r}_n = \vec{0} \quad (3.23)$$

where: $\vec{r}_{0,n}$ Vector from origin to axial axis of piston n .
 $\vec{x}_{p,n}$ Vector from end of $\vec{r}_{0,n}$ to the revolute joint center.
 \vec{r}_n Vector from origin to revolute joint.

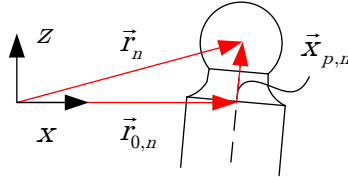


Figure 3.6: 2D vector loop of each axial piston.

This figure only shows how the pistons move in a single plane. By extending this figure into three dimensions, the endpoint of each piston is tracked as the swash plate rotates around the z-axis. This vector movement is shown in Figure 3.7.

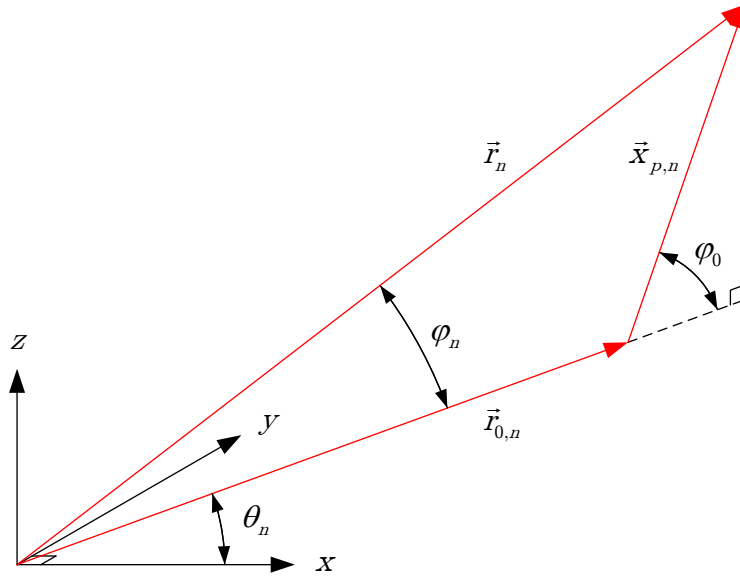


Figure 3.7: Illustration of the piston kinematics.

In Figure 3.7, θ_n describes the angular position of the n 'th piston. By knowing the angular position of each single piston around the swash plate and the swash plate tilt angle, the piston position and velocity of all pistons can be determined in a time simulation. The 3D vector loop from Figure 3.7 is given by Equation (3.24).

$$r_0 \begin{bmatrix} \cos(\theta_n) \\ \sin(\theta_n) \\ 0 \end{bmatrix} + x_{p,n} \begin{bmatrix} \cos(\varphi_0) \cos(\theta_n) \\ \cos(\varphi_0) \sin(\theta_n) \\ \sin(\varphi_0) \end{bmatrix} - r_n \begin{bmatrix} \cos(\varphi_n) \cos(\theta_n) \\ \cos(\varphi_n) \sin(\theta_n) \\ \sin(\varphi_n) \end{bmatrix} = \vec{0} \quad (3.24)$$

- where:
- θ_n Angular position of piston n in the x-y plane.
 - r_0 Length of $\vec{r}_{0,n}$.
 - $x_{p,n}$ Length of $\vec{x}_{p,n}$.
 - φ_n Angle between $\vec{r}_{0,n}$ and \vec{r}_n .
 - r_n Length of \vec{r}_n .
 - φ_0 Angle between horizontal and $\vec{x}_{p,n}$.

Note that the length r_0 is equal for all n pistons, therefore an index is not required of it. The angle φ_n and its derivative is given by:

$$\varphi_n = \alpha \cos(\theta_n) \quad (3.25)$$

$$\dot{\varphi}_n = \dot{\alpha} \cos(\theta_n) - \dot{\theta}_n \alpha \sin(\theta_n) \quad (3.26)$$

- where:
- $\dot{\varphi}_n$ Angular velocity of the angle between $\vec{r}_{0,n}$ and \vec{r}_n .
 - $\dot{\theta}_n$ Angular velocity of piston n .

Equation (3.24) is re-arranged to extract the desired variables in Equation (3.27).

$$\begin{bmatrix} \cos(\varphi_n) \cos(\theta_n) & -\cos(\varphi_0) \cos(\theta_n) \\ \cos(\varphi_n) \sin(\theta_n) & -\cos(\varphi_0) \sin(\theta_n) \\ \sin(\varphi_n) & -\sin(\varphi_0) \end{bmatrix} \begin{bmatrix} r_n \\ x_{p,n} \end{bmatrix} = r_0 \begin{bmatrix} \cos(\theta_n) \\ \sin(\theta_n) \\ 0 \end{bmatrix} \quad (3.27)$$

Solving Equation (3.27) for r_n and $x_{p,n}$ yields the following two Equations (3.28) and (3.29).

$$r_n = \frac{r_0 \sin(\varphi_0)}{\sin(\varphi_0 - \varphi_n)} \quad (3.28)$$

$$x_{p,n} = \frac{r_0 \sin(\varphi_n)}{\sin(\varphi_0 - \varphi_n)} \quad (3.29)$$

These equations describe the radial and axial position of each piston. Since the velocity of each piston will describe how much flow enters and leave each piston chamber, the above equations are differentiated with respect to time in Equations (3.30) and (3.31):

$$\dot{r}_n = \dot{\varphi}_n \frac{r_0 \cos(\varphi_n - \varphi_0) \sin(\varphi_0)}{(\sin(\varphi_n - \varphi_0))^2} \quad (3.30)$$

$$\dot{x}_{p,n} = -\dot{\varphi}_n \frac{2r_0 \sin(\varphi_0)}{\cos(2(\varphi_n - \varphi_0)) - 1} \quad (3.31)$$

where: \dot{r}_n Change in length of \vec{r}_n .

$\dot{x}_{p,n}$ Velocity of piston n .

The velocity of each piston is described in Equation (3.31) together with the diameter D_p of the pistons, describes the flow generated by each piston as the barrel rotates. Since the piston openings are closed when transferring from port A to port B and vice versa, an effective piston stroke length have to be derived using the effective opening angle. The effective piston stroke length is given by Equation (3.32).

$$L_{eff} = \frac{r_0 \sin(\alpha_{max} \cos(\theta_{A,O}))}{\sin(\varphi_0 - \alpha_{max} \cos(\theta_{A,O}))} - \frac{r_0 \sin(\alpha_{max} \cos(\theta_{A,C}))}{\sin(\varphi_0 - \alpha_{max} \cos(\theta_{A,C}))} \quad (3.32)$$

where: L_{eff} Effective stroke length of each piston.

$\theta_{A,O}$ Opening angle on port A.

$\theta_{A,C}$ Closing angle on port A.

$\theta_{B,O}$ Opening angle on port B.

$\theta_{B,C}$ Closing angle on port B.

The effective length is now known and dependent on the effective openings which is discussed in more detail in Section 3.4.3. The variable pumps maximum displacement $V_{d,max}$ is further expressed using the effective stroke length L_{eff} and the piston diameter D_p . This relationship is given by Equation (3.33).

$$V_{d,max} = N_p L_{eff} \frac{\pi}{4} D_p^2 \quad (3.33)$$

where: D_p Piston diameter.

$V_{d,max}$ Maximum pump displacement volume.

The length r_0 is solved by combining Equations (3.32) and (3.33) into Equation (3.34). With a known maximum tilt angle, α_{max} , theoretical displacement volume, $V_{d,max}$, piston diameter, D_p and number of pistons, N_p , the length of vector $\vec{r}_{0,n}$ is calculated using Equation (3.34).

$$r_0 = \frac{4V_{d,max}}{N_p \pi D_p^2} \left[\frac{\sin(\alpha_{max} \cos(\theta_{A,O}))}{\sin(\varphi_0 - \alpha_{max} \cos(\theta_{A,O}))} - \frac{\sin(\alpha_{max} \cos(\theta_{A,C}))}{\sin(\varphi_0 - \alpha_{max} \cos(\theta_{A,C}))} \right]^{-1} \quad (3.34)$$

With the length calculated in Equation (3.34), the displacement of each piston chamber is known. This is a necessary prerequisite because the length r_0 was not known through the spec sheet of the pump.

In the above equations the movement of each piston and the piston volumes are described. However the openings between the piston chambers and the two ports of the pump have not yet been discussed. The port openings as a function of the position of each piston is described in Section 3.4.3.

3.4.3 Ripple Flow Modeling

The pump piston control volumes interfere with the A and B port through a ported lens plate. The piston orifice opening connects the piston control volumes to the two pump ports A and B, and they are modeled using two variable orifices. The orifice opening depends on the location of each piston. An overview of the geometric layout describing the ported lens plate is given by Figure 3.8.

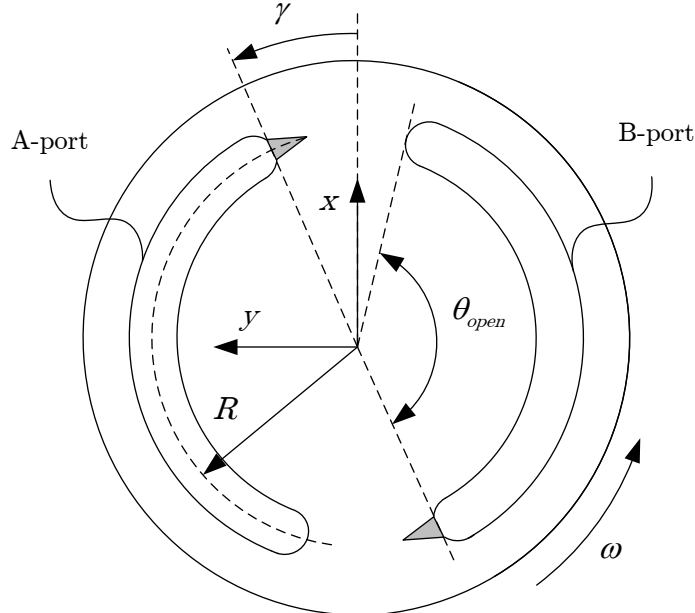


Figure 3.8: Illustration of the porting lens plate.

The rotation angle of the input shaft is expressed using Equation (3.35).

$$\theta(t) = \theta_0 + \int \omega(t) dt \quad (3.35)$$

where: θ Angular position of the input shaft.

θ_0 Initial rotation of the input shaft.

ω Angular velocity of the input shaft.

The opening angle is calculated on a knowledge that each piston chamber should be connected to either port A or port B at all times in order to reduce the high pressure gradients in the chamber. The opening angle is given by Equation (3.36)

$$\theta_{open} = \pi - \frac{D_p}{R} \quad (3.36)$$

where: θ_{open} Opening angle on the port plate.

D_p Diameter of the piston chamber.

R Radius of the port plate.

Since the piston chambers extend further than this opening angle, an opening and closing angle for each port is calculated. These calculations are shown below through Equations (3.37) to (3.40).

$$\theta_{A,O} = \gamma - \frac{D_p}{2R} \quad (3.37)$$

$$\theta_{A,C} = \theta_{open} + \gamma + \frac{D_p}{2R} \quad (3.38)$$

$$\theta_{B,O} = \pi + \gamma - \frac{D_p}{2R} \quad (3.39)$$

$$\theta_{B,C} = \gamma - \frac{D_p}{2R} \quad (3.40)$$

where: γ Pressure carry over angle [10].

By using these angles it is possible to describe the A and B opening for each single piston in the barrel. It is necessary to express the angle of each single piston as a function of pump pistons n_p . The angle of each piston $\theta_n(t)$ is given by Equation (3.41).

$$\theta_n(t) = \theta(t) + (n - 1)\Delta\theta \quad (3.41)$$

where: θ_n Angular position of piston n .

n Piston number.

$\Delta\theta$ Separation angle between each neighboring piston.

The separation angle between each piston is expressed using Equation (3.42).

$$\Delta\theta = \frac{2\pi}{N_p} \quad (3.42)$$

where: N_p Total number of pistons in the pump.

Each opening of piston number n can now be expressed using a simplified relationship. The openings $u_{A,n}$ and $u_{B,n}$ is expressed using Equations (3.43) and (3.44).

$$u_{A,n} = \begin{cases} 0 & \text{mod}(\theta_n, 2\pi) \in [0, \theta_{A,O}] \\ 1 & \text{mod}(\theta_n, 2\pi) \in [\theta_{A,O}, \theta_{A,C}] \\ 0 & \text{mod}(\theta_n, 2\pi) \in [\theta_{A,C}, 2\pi] \end{cases} \quad (3.43)$$

$$u_{B,n} = \begin{cases} 1 & \text{mod}(\theta_n, 2\pi) \in [0, \theta_{B,C}] \\ 0 & \text{mod}(\theta_n, 2\pi) \in [\theta_{B,C}, \theta_{B,O}] \\ 1 & \text{mod}(\theta_n, 2\pi) \in [\theta_{B,O}, 2\pi] \end{cases} \quad (3.44)$$

where: $u_{A,n}$ Opening between piston chamber n and port A.

$u_{B,n}$ Opening between piston chamber n and port B.

The function $\text{mod}(\theta_n, 2\pi)$ produce a repeating angle ranging from 0 to 2π radians. Note however that the opening definitions in Equations (3.43) and (3.44) are valid for $\gamma \geq \frac{D_p}{2R}$. With a smaller γ , the opening and closing bounds must be changed. The openings can have only two possible configurations, open and closed. This is a simplified description of the openings. The flow is simplified and considered as a direct product of the area and axial speed of the piston. With this definition, the flow generated by piston n is given by:

$$Q_n = -\dot{x}_{p,n} \frac{\pi}{4} D_p^2 \quad (3.45)$$

where: Q_n Flow generated by piston n .

$\dot{x}_{p,n}$ Axial movement speed of piston n .

D_p Diameter of each piston.

The positive flow direction is out of the pump, i.e. the volume flow that is pushed out of a piston chamber. This is accomplished with the negative sign in Equation (3.45) because the piston velocity is defined positive with expanding volume, refer to Figure 3.7 which shows the positive direction of $\vec{x}_{p,n}$. The complete volume flow going out or in of the two ports are given by the following two equations:

$$Q_{P,A} = \sum_{n=1}^{N_p} (u_{A,n} Q_n) \quad (3.46)$$

$$Q_{P,B} = \sum_{n=1}^{N_p} (u_{B,n} Q_n) \quad (3.47)$$

where: $Q_{P,A}$ Flow through port A.

$Q_{P,B}$ Flow through port B.

In order to isolate the ripple flow, the mean theoretical flow going through port A and B is calculated:

$$\bar{Q}_{P,A} = -\bar{Q}_{P,B} = \frac{\omega}{2\pi} \frac{\alpha}{\alpha_{max}} V_{d,max} \quad (3.48)$$

- where:
- $\bar{Q}_{P,A}$ Steady State flow from port A.
 - $\bar{Q}_{P,B}$ Steady State flow from port B.
 - α Swash plate tilt angle.
 - α_{max} Maximum swash plate tilt angle.
 - $V_{d,max}$ Maximum displacement of the pump.
 - ω Shaft rotation speed.

Using the complete pump flow and theoretical flow the ripple flow is isolated:

$$\Delta Q_{P,A} = Q_{P,A} - \bar{Q}_{P,A} \quad (3.49)$$

$$\Delta Q_{P,B} = Q_{P,B} - \bar{Q}_{P,B} \quad (3.50)$$

Depending on the usage, the model can include the ripple flow using Equations (3.46) and (3.47), or use the theoretical volume flow in Equation (3.48). Bear in mind that the theoretical volume flow is much easier to calculate as the piston kinematics are not necessary. In the next subsection an example of the ripple flow is shown compared to the theoretical flow.

3.4.4 Ripple Flow Amplitude Analysis

In this section the difference between the mean flow and ripple flow is displayed. With the basis of an A4VSG pump described in Appendix D.1 the ripple flow is created. The pump flow is calculated using these parameters:

Shaft speed	$\omega = 1450 \text{ rpm}$
Swash plate angle	$\alpha = 15^\circ$
Number of pistons	$N_p = 9$
Diameter of each piston	$D_p = 20.5 \text{ mm}$
Piston tilt angle	$\varphi_0 = 85^\circ$
Pressure cross over angle	$\gamma = 20^\circ$
Port plate radius	$R = 33.1 \text{ mm}$

Using the kinematic equations in Section 3.4, the total flow through port A and B on the pump is calculated. The mean volume flow through port A is calculated with Equation (3.48). The resulting ripple flow from Equations (3.49) and (3.50) using the above parameters are shown in Figure 3.9. The ripple flow is simulated to represent one full revolution of the input shaft.

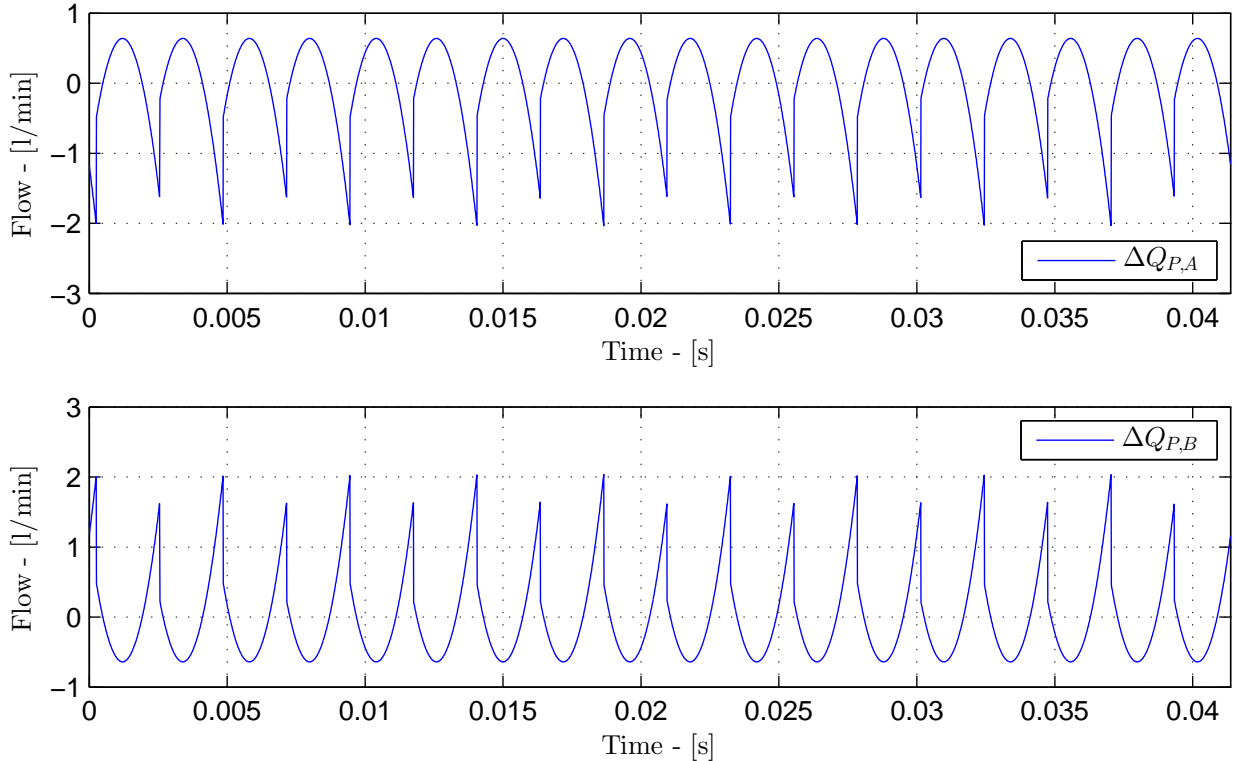


Figure 3.9: Ripple flow in port A and port B.

A ratio between the ripple flow and the theoretical flow is defined as the maximum value of the ripple flow divided by the value of the mean flow:

$$\eta_r = \frac{\max(\Delta Q_{P,A})}{\bar{Q}_{P,A}} \quad (3.51)$$

From the configuration in Figure 3.9 the ratio between the ripple flow $\Delta Q_{P,A}$ and the theoretical flow $\bar{Q}_{P,A}$ is roughly

$$\eta_r = \frac{2.063l/min}{102.95l/min} \approx 2\% \quad (3.52)$$

This finding is consistent with Manring in [10], page 283, where a graph states that 2% ripple flow is present when having 9 pistons. The ripple flow ratio η_r with different number of pistons is shown in Figure 3.10.

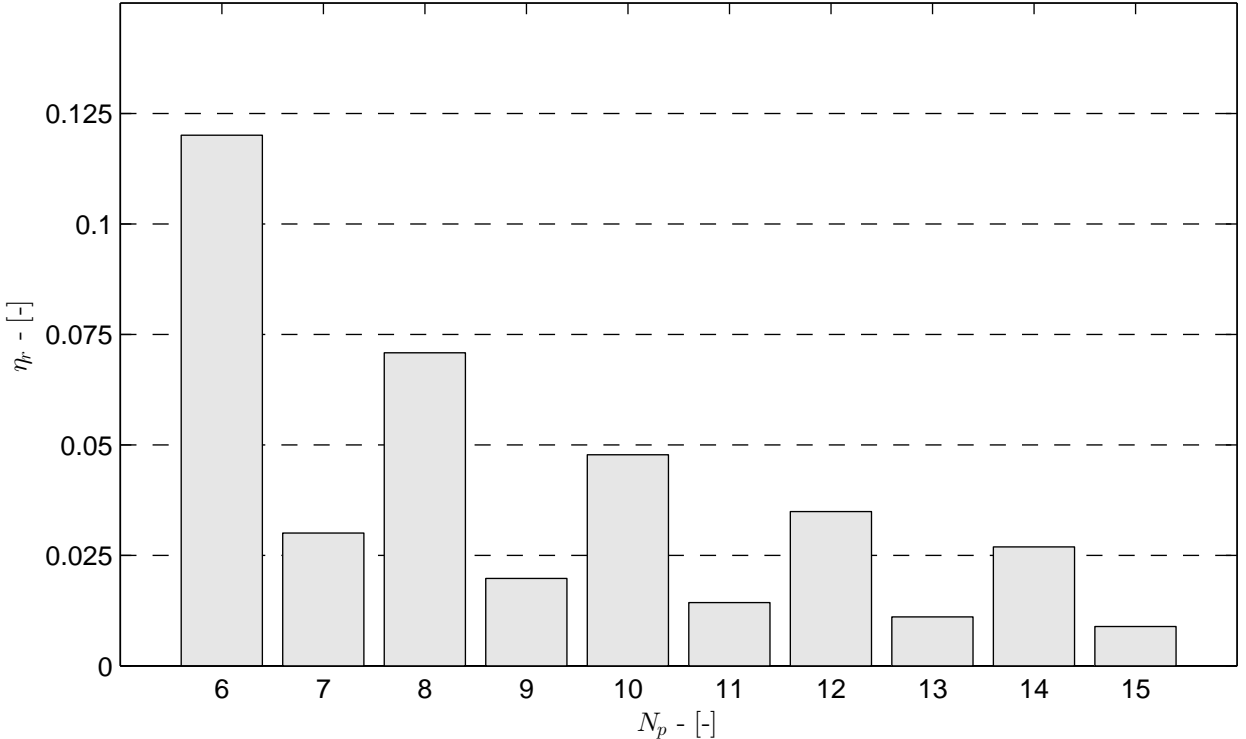


Figure 3.10: Ratio between ripple flow and mean flow.

As shown in Figure 3.10 the ratio is much larger for even number of pistons than with odd numbers. This comes from a doubling of ripple-frequency with odd number of pistons as illustrated in Figure 3.9 where a single revolution with 9 pistons shows 18 spikes. That is why pump and motor manufacturers generally uses odd number of pistons, as it decreases the ripple amplitudes compared to even numbers. Also using odd number of pistons makes the ripple less likely to trigger the resonance frequency of a nearby component because of the doubled ripple frequency.

Since the time simulation of the piston kinematics is computationally heavy, it is desirable to make a simplification of the ripple flow. This simplification is presented in the next subsection.

3.4.5 Empirical Simplification of the Ripple Flow

Calculating the ripple flow during a simulation requires a great deal more processing power than just using the theoretical mean flow. The reason is the high frequency of the ripple spikes occurring with 9 pistons and a 1450rpm shaft speed. With this configuration the ripple signal has a frequency of $\frac{1450}{60} \cdot 18 = 435Hz$, which makes variable time step solvers run much slower than before the ripple effects were added. To counter this, a simplification of the ripple signal is here proposed to lessen the computational power needed to simulate the ripple flow. The ripple signal shown in Figure 3.9

resembles the absolute value of a sine curve, and therefore the simplified ripple is based on this. The simplified ripple flow $\Delta Q_{P,A}^{(Simp)}$ is given in Equation (3.53).

$$\Delta Q_{P,A}^{(Simp)} = |A_r \sin(2\pi f_r t)| + O_r \quad (3.53)$$

- where:
- $\Delta Q_{P,A}^{(Simp)}$ Simplified ripple flow.
 - A_r Simplified ripple amplitude.
 - f_r Ripple frequency.
 - O_r Simplified ripple offset.

The ripple frequency f_r is given by the shaft speed ω and number of pistons N_p in Equation (3.54).

$$f_r = N_p \frac{\omega}{4\pi} (1 + \text{mod}(N_p, 2)) \quad (3.54)$$

The offset O_r and amplitude A_r needs to be determined by examining the ripple flow generated by the full kinematic model. Since the mean value of the ripple flow should be zero, the relationship between the offset O_r and amplitude A_r is determined by integrating the ripple stroke a half revolution and set to zero. This is shown in Equations (3.55) through (3.57).

$$\int_{\theta=0}^{\pi} (A_r \sin(\theta) + O_r) d\theta = 0 \quad (3.55)$$

$$[-A_r \cos(\theta)]_0^\pi + [O_r \theta]_0^\pi = 0 \quad (3.56)$$

$$O_r = -\frac{2}{\pi} A_r \quad (3.57)$$

where: θ Input shaft angle.

The ripple amplitude relies heavily on the number of pistons as shown in Figure 3.10. Because of the large and complex equations required to determine the ripple flow amplitude analytically, an empirical approximation is chosen to determine the simplified ripple amplitude A_r . This approximation is a function of the ratio η_r between the ripple flow and the theoretical mean flow. From Figure 3.9 the simplified ripple flow must be tangent to $\Delta Q_{P,A}$ most of the time, and the smooth top should be equal. From this figure, the smooth top is at ≈ 0.6392 , and the maximum value of the simplified ripple flow from Equation (3.53) must be as high:

$$\max(\Delta Q_{P,A}^{(Simp)}) = A_r + O_r = 0.6392 \quad (3.58)$$

By substituting Equation (3.57) for O_r in Equation (3.58), Equation (3.59) is formed.

$$A_r - \frac{2}{\pi} A_r = 0.6392 \quad (3.59)$$

Since the simplified ripple stroke should be functional for any setup of swash plate angle and number of pistons, it is desirable that the ripple amplitude is a function of the ratio between maximum ripple flow and mean flow. This relationship is given by Equation

$$A_r = \psi \eta_r \bar{Q}_{P,A} \quad (3.60)$$

where: ψ Empirical ratio of the ripple flow amplitude.

ψ is an empirically determined factor that adjusts the amplitude of the simplified ripple. By substituting Equation (3.60) for A_r in Equation (3.59), Equation (3.61) is formed.

$$\psi \eta_r \bar{Q}_{P,A} \left(1 - \frac{2}{\pi}\right) = 0.6392 \quad (3.61)$$

$$\rightarrow \psi = \frac{0.6392}{\eta_r \bar{Q}_{P,A} \left(1 - \frac{2}{\pi}\right)} \quad (3.62)$$

With the value of η_r from Figure 3.10 and the theoretical flow this ratio is determined to be:

$$\psi = \frac{0.6392}{0.0198 \cdot 102.95 \cdot \left(1 - \frac{2}{\pi}\right)} = 0.8638 \quad (3.63)$$

Now that the ratio ψ is known, the actual simplified ripple amplitude is calculated with the following equation granted that η_r is known:

$$A_r = \psi \eta_r \bar{Q}_{P,A} \quad (3.64)$$

The total flow including simplified ripple and mean flow is given by:

$$Q_{P,A}^{(Simp)} = \bar{Q}_{P,A} + \Delta Q_{P,A}^{(Simp)} \quad (3.65)$$

The flow through port B is set to be the negative of flow through port A:

$$Q_{P,B}^{(Simp)} = -Q_{P,A}^{(Simp)} \quad (3.66)$$

A comparison between true kinematic ripple and simplified ripple is shown in Figure 3.11.

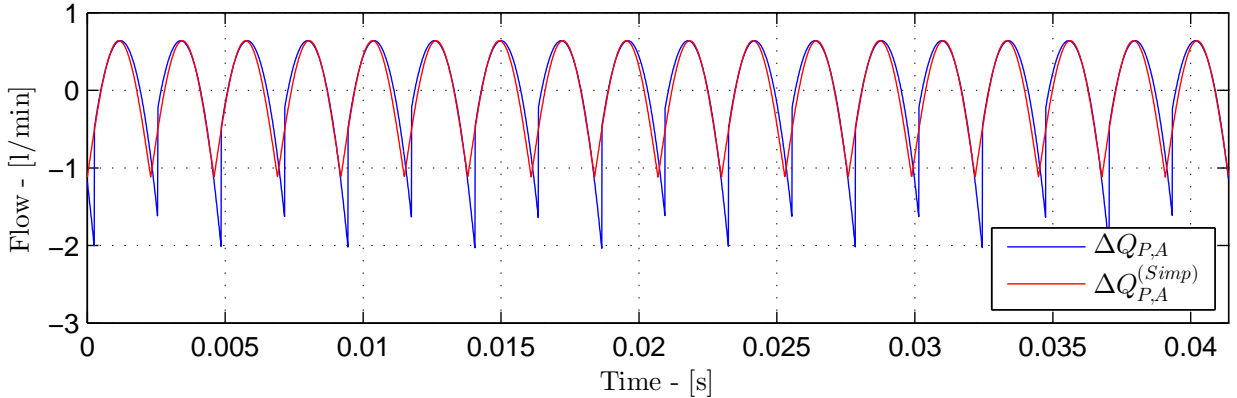


Figure 3.11: Comparison of simplified vs. actual ripple flow with 9 pistons.

As shown in this figure, the simplified ripple flow follows the actual ripple flow closely, but does not include the short spikes at the bottom.

After making this ripple flow simplification, the A4VSG pump is now mathematically modeled from swash plate angle input to flow generation. How this model is stitched together into a single non-linear model is shown in the next section.

3.5 SimulationX Model

From the pump model in Chapter 3 a SimulationX model is created. An overview of the model is shown in form of a block diagram in Figure 3.12.

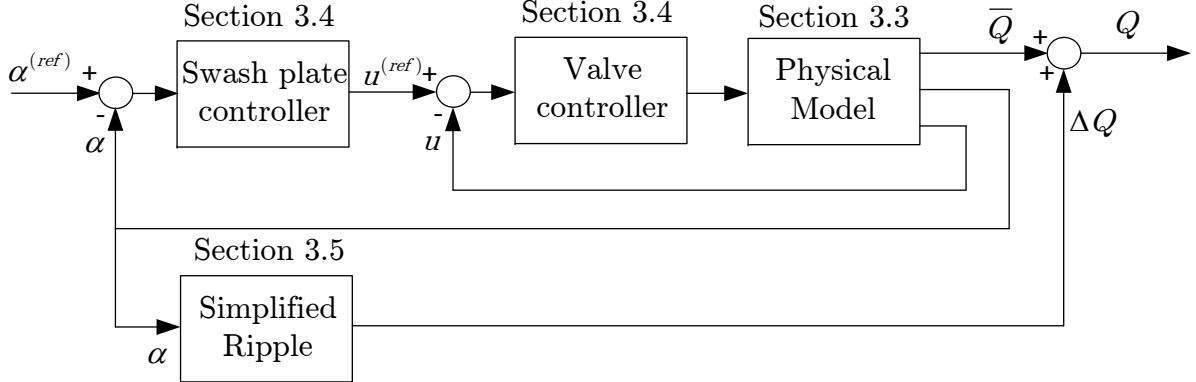


Figure 3.12: Block diagram of the A4VSG pump model.

In this figure, there is just one input, which is the reference swash plate angle $\alpha^{(ref)}$. The deviation between the actual swash plate angle and the reference is used as input to a controller as detailed in Section 3.3. The output of this controller is the valve reference, and the deviation between the valve reference and the actual valve is the input to the valve controller. This controller is also detailed in Section 3.3. The output of this controller is sent to the valve in the physical system. This block contains all the governing equations of the system, as well as the time integration necessary to produce the states at next time step. The physical model is detailed in Section 3.2. There are three outputs from this model; the actual valve position u , the actual swash plate angle α and the mean volume flow. The actual swash plate angle and valve position is used as feedback to the two control systems. The mean flow \bar{Q} is summed up with the simplified ripple flow to produce the total output flow. The ripple flow is detailed in Section 3.4.

This SimulationX model is further detailed in Appendix F, where the SimulationX blocks used and references to the governing equations are detailed.

The next Chapter focuses on every result from performing tests on the pump or in the simulation model.

Chapter 4

Results from Hydraulic Pump Model

This chapter contains all the results gathered by using the methods, information and algorithms as described in the Method Chapter 2 and the hydraulic pump model in Chapter 3. Every result subsection includes references to the method and/or parts of the simulation model used to achieve the results. This chapter is organized as follows. Section 4.1 presents measured flow versus swash plate angle to verify the rotational speed of the induction motor and the maximum pump displacement. Section 4.2 presents results from Black box modeling of the pump based on frequency response analysis. Section 4.4 presents results from the non-linear Grey box modeling of the swash plate dynamics. Section 4.5 presents results and findings from using the SimulationX model of the pump.

4.1 Steady State Pump Flow Measurements

The oil flow of the A4VSG closed loop pump have been measured using two HYDAC Flow sensor as presented in the components Appendix D.7. Because of the various measurement intervals of the two flow sensors, both have been installed in the hydraulic system. The two sensors replaced the load which is displayed in Figure 3.1 in order to measure the output flow of the pump. From the two sensors, two graphs were obtained that shows the measured flow up to 20 l/min and from 40 l/min. These two graphs are shown in Figure 4.1.

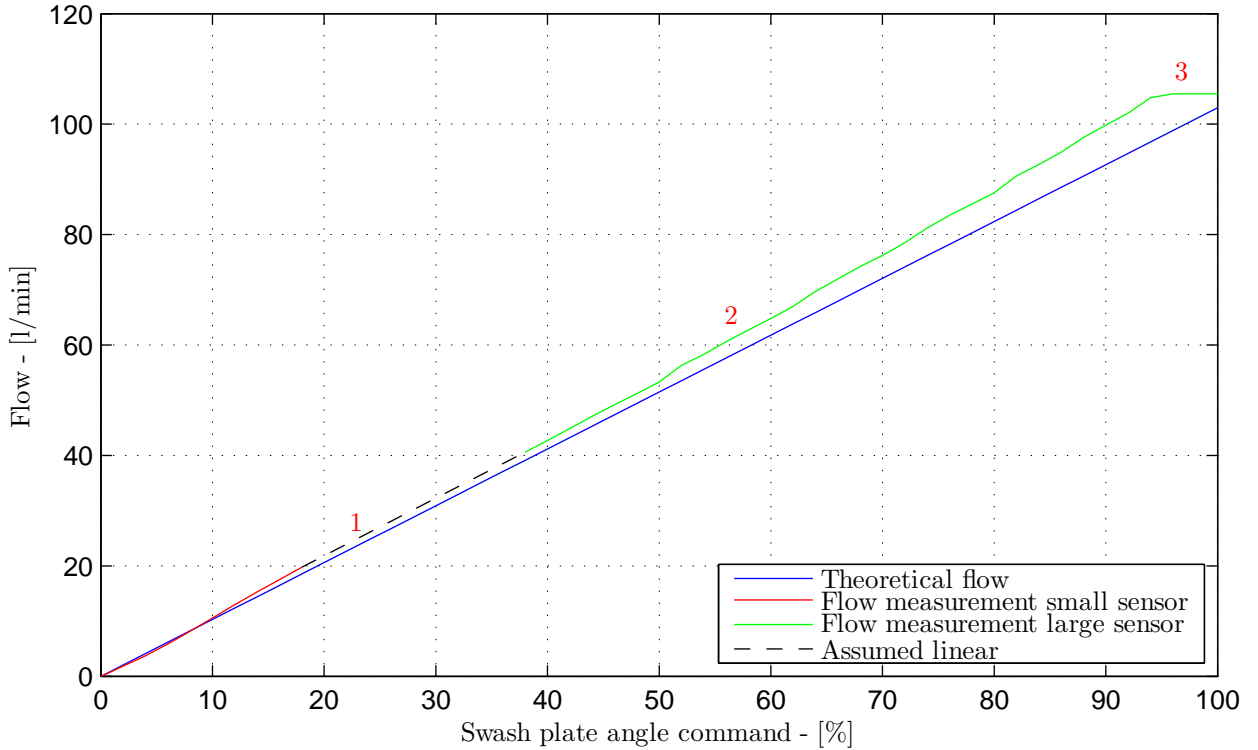


Figure 4.1: Comparison between flow measurement and theoretical flow at no load.

In this figure the blue line is the theoretical flow expected at normal conditions, the red and green line shows the measured flow using the two flow sensors and finally the black stapled line indicates an assumed linear flow between the measurements of the two sensors. On this figure there are also three red colored numbers which are explained here:

1. Here the small flow sensor gets outside its measurement area which is 20 l/min, and the large flow sensor starts at 40 l/min.
2. As seen here, the slope of the measured flow is different than the theoretical flow. If the motor driving the pump is actually faster than 1450 rpm, it would explain the larger flow.
3. Finally the flow gradient stops near 95% swash plate angle which could be due to a physical stop inside the pump.

From these flow measurements, the pump is assumed give correct amount of flow. In the next subsection the swash plate dynamics are uncovered using a frequency response analysis and a transfer function estimation.

4.2 Black Box Model

In this section a Black box model of the swash plate dynamics is identified by performing a frequency response test and analysis. At first the dynamics are assumed independent on the pump pressure in Section 4.2.1, but the load dependency is checked in Section 4.2.2. Finally the dynamics while the pump is under load vs no-load is compared in Section 4.2.3 and a performance assessment of the Black box model is performed in Section 4.2.4.

4.2.1 No-Load Situation

The results in this section is based on a test using the physical layout described in Section 3.1.2 without any load. 18 frequency response tests were first performed using the method in Section 2.1.1, and the data was analyzed with a frequency response analysis described in Section 2.3. The magnitude and phase derived from the analysis is used to estimate 18 transfer functions (TFs) using a TF estimation toolbox described in Section 2.4.

The 18 frequency response tests were carried out at $\pm[25, 50, 75]\%$ offset with $[5, 10, 20]\%$ amplitude in order to look for nonlinearities in the swash plate dynamics at different offsets and amplitudes. For this estimation, a TF with 5 poles and no zeros was chosen to describe the system. The template for this TF is shown in Equation (4.1):

$$G_{est}(s) = \frac{b_0}{s^5 + a_4 s^4 + a_3 s^3 + a_2 s^2 + a_1 s + a_0} \quad (4.1)$$

where: b_0 Constant value describing the numerator.

$a_4 \dots a_0$ Constant values describing the denominator.

The reason for using a fifth order TF is that the pump model described in Chapter 3 introduces 5 states if the pressure on each side of the actuating control piston is combined to single pressure difference state. The estimation toolbox returns the five constant values and a percentage which tells how good the fit is. For the 18 tests, the resulting constant values are given in Table 4.1.

Table 4.1: Estimated TFs describing the dynamics of the swash plate during no load.

O [%]	A [%]	b₀ [10 ⁶]	a₄ [10 ⁰]	a₃ [10 ⁰]	a₂ [10 ³]	a₁ [10 ⁶]	a₀ [10 ⁶]
-75	5	63158	216	89266	12047	1426	61788
-75	10	69756	214	88918	12283	1425	69153
-75	20	78475	254	101964	15226	1521	79129
-50	5	60963	196	89134	11583	1397	59702
-50	10	67935	201	86374	11841	1373	66457
-50	20	78762	243	101944	15372	1540	79809
-25	5	62091	191	88408	11612	1429	60185
-25	10	70880	208	88674	12347	1452	69731
-25	20	82994	231	104369	15665	1608	82857
25	5	62091	191	88408	11612	1429	60185
25	10	70880	208	88674	12347	1452	69731
25	20	82994	231	104369	15665	1608	82857
50	5	60963	196	89134	11583	1397	59702
50	10	67935	201	86374	11841	1373	66457
50	20	78762	243	101944	15372	1540	79809
75	5	63158	216	89266	12047	1426	61788
75	10	69756	214	88918	12283	1425	69153
75	20	78475	254	101964	15226	1521	79129

Bode plots of the transfer functions in Table 4.1 are shown in Appendix C together with actual frequency response and two Grey box models. The Grey box models are identified later in this results chapter in Section 4.4. The next subsection presents results from performing a frequency response test and analysis on the swash plate dynamics during a load situation.

4.2.2 Load Situation

These results comes from a test using the physical layout described in Section 3.1.2 with a load. The load is created using an orifice creating a pressure drop between port A and port B of the pump. The pressure drop at different intervals are shown in Table 4.2.

Table 4.2: Pressure drop over the orifice with a certain swash plate angle.

Angle α [%]	Pressure Drop Δp [bar]
65	32
70	41
75	52
80	63
85	75

As shown by the table, the load pressure is varying between 32 and 75 bar over the swash plate

angle region between 65% and 85% of maximum angle. A frequency response test and analysis described in Sections 2.1.1 and 2.3 is conducted on the swash plate angle of the pump while the orifice is the load. The offset was set to 75% max angle to reach the largest load pressures. Two tests at 5% and 10% amplitude were performed and the resulting transfer functions using the TF estimator in Section 2.4 are given in Table 4.3.

Table 4.3: Estimated TFs describing the dynamics of the swash plate during load.

O [%]	A [%]	$b_0 [10^6]$	$a_4 [10^0]$	$a_3 [10^0]$	$a_2 [10^3]$	$a_1 [10^6]$	$a_0 [10^6]$
75	5	72118	236	96809	13310	1594	70028
75	10	81114	231	97740	13468	1630	79655

In order to compare whether the dynamics of the swash plate angle have changed with the inclusion of the load, the next subsection compares the two setups side by side.

4.2.3 Comparison Between Load and No-Load Situations

The pump was tested without any load and with an orifice as a load in Sections 4.2.1 and 4.2.2 respectively. In this section the measured frequency responses between them are compared to check if the dynamic response is different with the added load to the swash plate. Figure 4.2 and 4.3 shows these comparisons at 5% and 10% amplitude respectively.

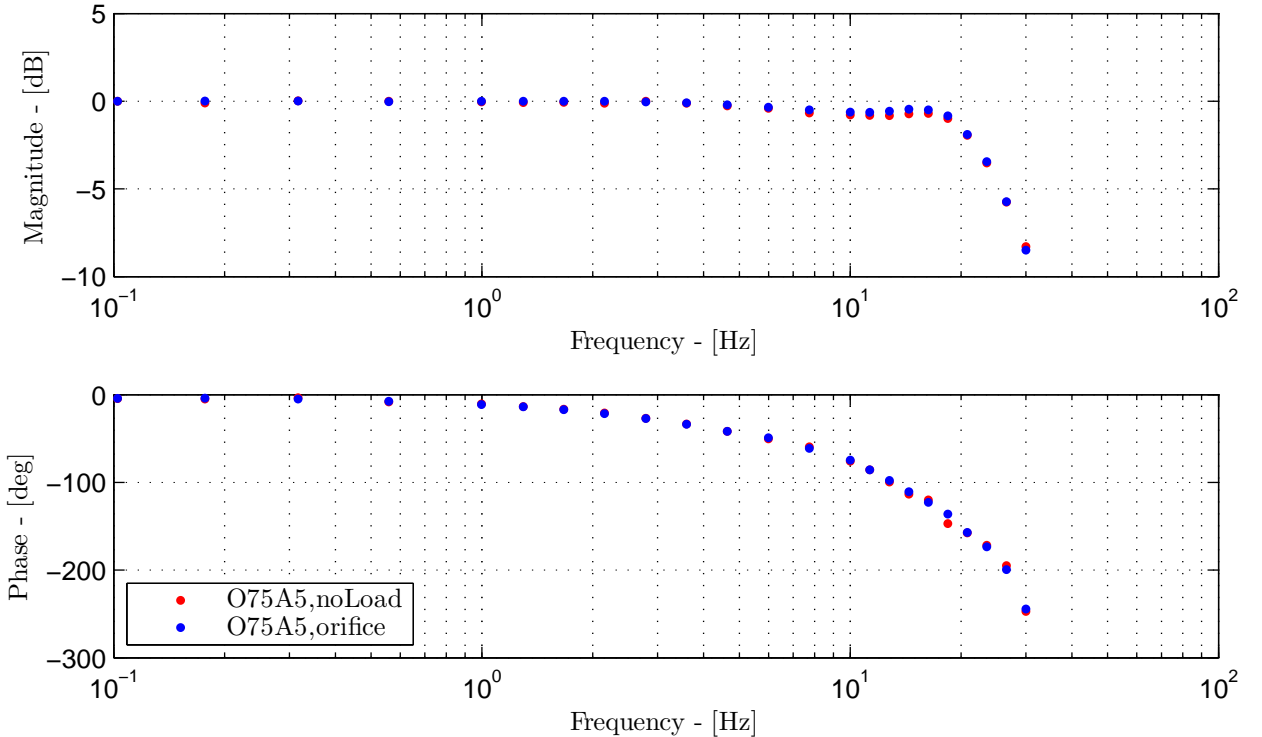


Figure 4.2: Frequency response comparison between a load and a no-load situation at 5% amplitude.

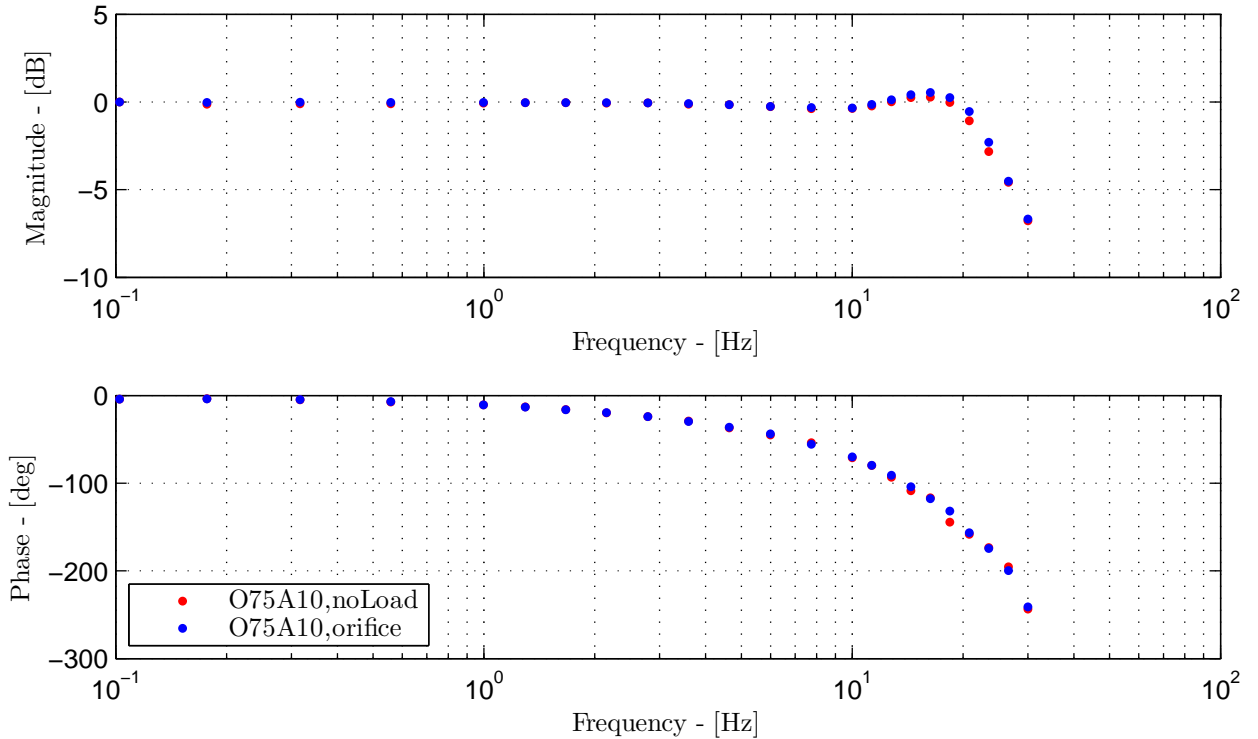


Figure 4.3: Frequency response comparison between a load and a no-load situation at 10% amplitude.

For both figures, the blue dots shows the frequency response during the load-situation and the red dots shows the frequency response during a no-load situation. As shown on the figure, the differences in dynamics between the two situations are negligible. The small deviations between them may even arise from temperature differences, and not because of the load. Therefore the Black box models describing the swash plate dynamics during no load is used in the next subsection to assess their performance.

4.2.4 Black Box Model Accuracy

The accuracy of each swash plate transfer function presented in Section 4.2.1 is checked with a mean deviation and maximum deviation as described in Section 2.7. Both the magnitude and phase is checked against the actual frequency response at the given offset and amplitude. The result is shown in Table 4.4.

In Table 4.4, the six columns describe the following from left to right:

1. Offset of the test sine input.
2. Amplitude of the test sine input.
3. Mean magnitude deviation between measured frequency response and model response.
4. Max magnitude deviation between measured frequency response and model response.
5. Mean phase deviation between measured frequency response and model response.
6. Max phase deviation between measured frequency response and model response.

Table 4.4: Black Box model verification - Frequency domain.

O [%]	A [%]	\bar{E}_M [dB]	$E_M^{(max)}$ [dB]	\bar{E}_P [deg]	$E_P^{(max)}$ [deg]	Verification
-75	5	0.34	1.98	4.6	22.9	✓
-75	10	0.21	1.29	4.2	21	✓
-75	20	0.15	0.61	4.1	29.3	✓
-50	5	0.35	2.04	4.7	25.7	✗
-50	10	0.23	1.41	4.4	22.4	✓
-50	20	0.14	0.69	4.1	29.3	✓
-25	5	0.35	1.96	4.7	25.6	✓
-25	10	0.21	1.29	4.4	21.7	✓
-25	20	0.15	0.76	4.2	31	✓
25	5	0.35	1.96	4.7	25.6	✓
25	10	0.21	1.29	4.4	21.7	✓
25	20	0.15	0.76	4.2	31	✓
50	5	0.35	2.04	4.7	25.7	✗
50	10	0.23	1.41	4.4	22.4	✓
50	20	0.14	0.69	4.1	29.3	✓
75	5	0.34	1.98	4.6	22.9	✓
75	10	0.21	1.29	4.2	21	✓
75	20	0.15	0.61	4.1	29.3	✓

7. A ✓ is shown if the model is within the criteria in Section 1.3, or a ✗ is shown if the model does not satisfy **all** criteria.

The accuracy of each Black box model is compared to the design criteria in Section 1.3, and the result is shown in the rightmost column in Table 4.4. Two of the models do not pass the accuracy test on the criteria of maximum 2 dB magnitude deviation, and are therefore not verified.

A frequency response analysis isn't the only way to map the dynamic response of a system. In the next section, the results from the frequency response tests are used to investigate the performance of a chirp response analysis.

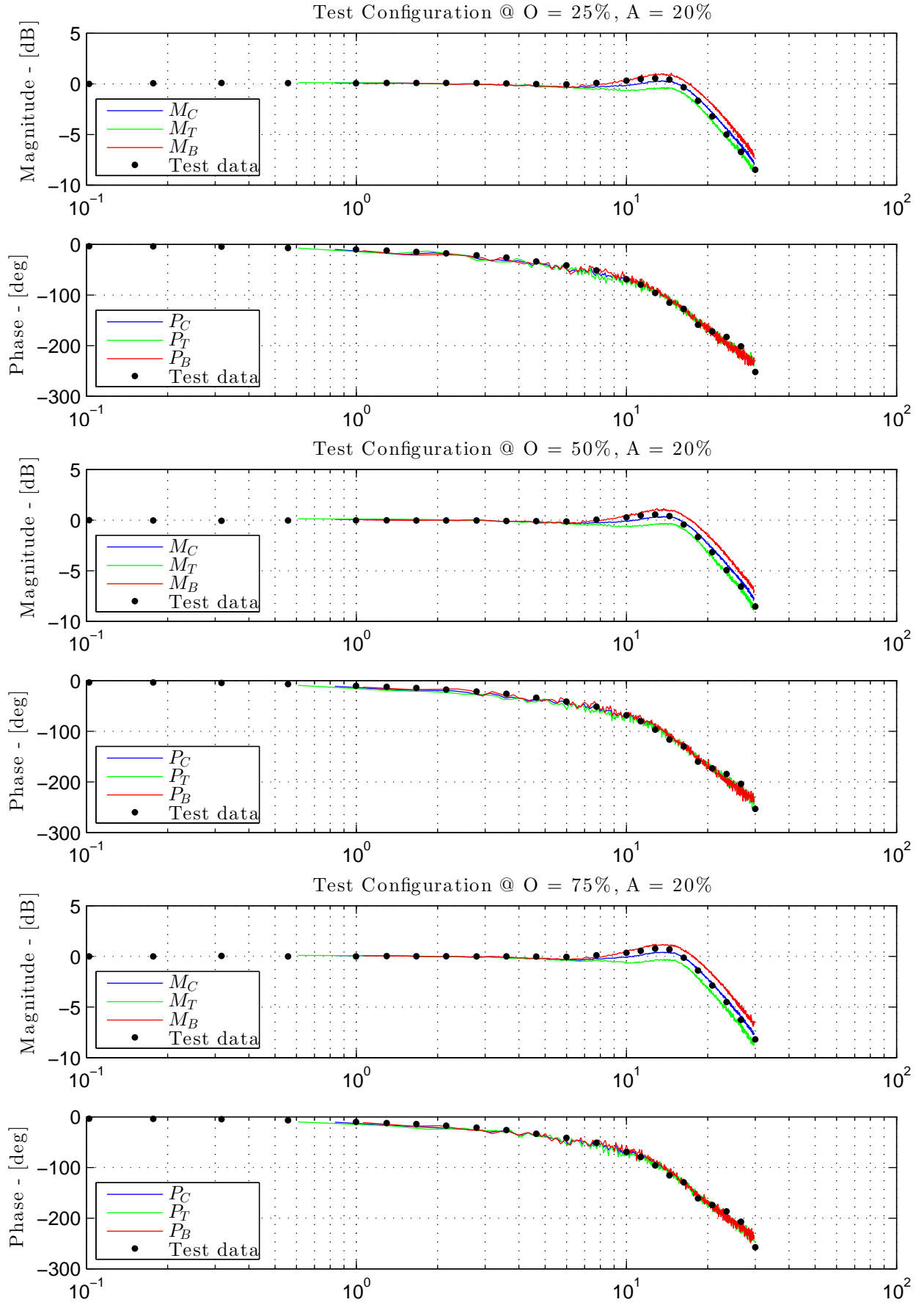
4.3 Chirp Test Compared to Traditional Frequency Response Test

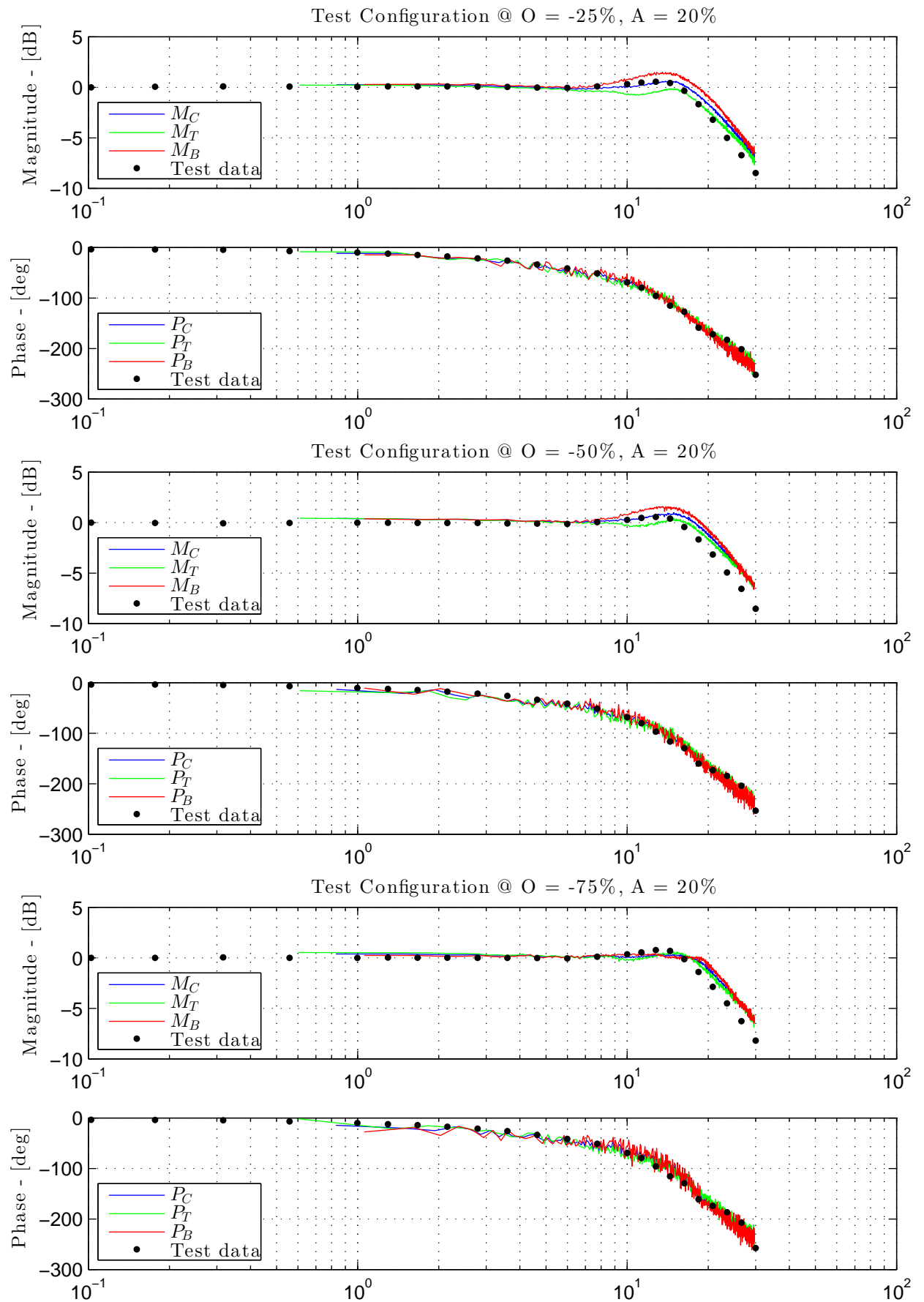
In the previous section the swash plate dynamics in the A4VSG pump was identified with a frequency response analysis. In this section the pump is tested with a chirp signal and the response is used to identify the dynamics with the algorithm described in Section 2.5. The result from this algorithm is compared with a standard frequency response analysis which is described in Section 2.3. The two following Figures 4.4 and 4.5 shows the comparison between the two methods. The title in each figure shows the test configuration and the x-axis is the frequency in Hz. The black dots are the reference dynamics from a standard frequency response analysis, the blue line shows the mean magnitude and phase from a chirp response analysis, and the green and red lines shows the top and bottom responses respectively. The top and bottom responses are shown to compare the dynamics in each direction.

In Figure 4.4 the positive offset configurations are shown with an amplitude of 20%. The blue line which is the mean chirp analysis response is very close to the reference data, the black dots. The bottom response (red curve) shows a faster response than the blue curve because it's easier for the pumps actuating circuit to move the swash plate to zero angle than from zero.

In Figure 4.5 the results from the chirp response test on negative offsets deviates a bit more from the standard frequency response analysis. The chirp response analysis reports a better response on the magnitude plot than the frequency response test. The reason may be minor mistakes in the algorithm or temperature/system differences between the chirp test and the frequency response test.

The biggest problem with estimating a linear transfer function for a non-linear system like the A4VSG swash plate mechanism, is that a separate Black box model is created for each linearization point. Instead, a non-linear Grey box model of the system can be identified to reproduce the same results around all linearization points. In the next subsection, the parameters for such a non-linear Grey box model is identified through optimization.

Figure 4.4: Frequency response analysis compared to chirp response analysis @ $A = 20\%$.

Figure 4.5: Frequency response analysis compared to chirp response analysis @ $A = 20\%$.

4.4 Optimization of Non-Linear Grey Box Model

4.4.1 Resulting Model Parameters

The Grey box model of the pump is described in Section 3.2 and the control system for the swash plate tilting is described in Section 3.3. These two combined is the non-linear Grey box model of the pump. This model is optimized using an interior point algorithm as explained in Section 2.6.1. The objective function combines deviations in the time domain and frequency domain, as explained in point 3 in Section 2.6.2. The time domain part is the total deviation between measured valve position and simulated valve position. To get time domain data, a stochastic wave with $T_p = 1\text{s}$ and $H_s = 100\%$ was used as input to the pump. The stochastic wave test is described in Section 2.1.3.

The frequency domain part of the objective function is obtained by first performing a frequency response test and analysis of the pump as described in Section 2.1.1 and 2.3 respectively. The result from this is frequency data of the dynamics between swash plate angle reference and actual swash plate angle. Such a test was performed at offsets $\in [-75, -50, -25, 25, 50, 75]\%$ and amplitudes $\in [5, 10, 20]\%$ to cover nonlinearities in the pump. To get simulated frequency data, the same frequency response test and analysis is performed from simulation data of the pump. The frequency domain objective part is therefore the deviations between the true frequency responses and simulated ones.

Using this objective function, the unknown parameters are optimized using an interior-point algorithm. The known/static parameters such as oil stiffness β and oil density ρ is given in Appendix E for reference. Two models were optimized; one model that keeps the cylinder data from Appendix D.2 as constant values, and one model where these values are variable in the optimization. **The Grey box model with the locked cylinder data is hereby called the “Locked Grey box model” and the Grey box model with the cylinder area and stroke length as optimizable parameters is hereby called the “Free Grey box model”.** The reason for optimizing two models is to see whether or not there is an advantage in measuring/acquiring hard parameters and lock them in the model. For the first model with locked cylinder data, the unknown parameters together with their upper and lower linear bounds as well as the final value are shown in Table 4.5.

Table 4.5: Estimated Parameters for the Locked Grey Box Model.

Parameter	Lower bound	Upper bound s	Final value	Unit
ω_v	18	35	34.14	Hz
ζ_v	0.3	2	1.4461	—
L	-	-	34.2	mm
A_p	-	-	1260	mm ²
V_0	0.01	0.5	0.0211	dm ³
m_{eff}	20	700	500	kg
k	0	30	17.485	N/mm
b	0	30	5.609	Ns/mm
K_p	0	100	27.493	—
K_D	0.01	1	1	—
T_d	0.005305	0.0159	0.00354	—
K_L	0.02	5	0.0850	mm ²
τ	0	50	5.797	ms

For the second model that keeps the cylinder data free, the unknown parameters together with their upper and lower linear bounds as well as the final values are shown in Table 4.6.

Table 4.6: Estimated Parameters for the Free Grey Box Model.

Parameter	Lower bound	Upper bound	Final value	Unit
ω_v	18	35	28.05	Hz
ζ_v	0.3	2	0.82031	—
L	30	120	47.011	mm
A_p	314.15	5026.54	401.33	mm ²
V_0	0.01	0.5	0.0607	dm ³
m_{eff}	20	700	62.384	kg
k	0	30	13.445	N/mm
b	0	30	13.422	Ns/mm
K_p	0	100	42.445	—
K_D	0.01	1	0.24111	—
T_d	0.0035368	0.0159	0.0040576	—
K_L	0.02	5	0.02	mm ²
τ	0	50	3.83	ms

As shown from Tables 4.6 and 4.5, there are some differences between the two models. Especially the effective mass m_{eff} is much larger on the locked Grey box model compared to the free Grey box model. This difference is most likely caused by the larger piston area on the locked Grey box model, which in turn requires a larger inertia to limit the acceleration. Bode plots of the Free and Locked Grey box models are shown in Appendix C.

Although the models are identified in this section, the accuracy of either model have not been

elaborated yet. A comparison of the two models is given in the next subsection to identify the superior model.

4.4.2 Grey Box Model Accuracy

In the previous Section, two Grey box models were presented, namely a Locked Grey box model and a Free Grey box model. The difference between the two is whether or not the area and stroke length of the cylinder should be optimizeable parameters or not. In order to validate the performance of the two models in the frequency domain, a model verification procedure described in Section 2.7 is used. The output of this procedure is essentially the mean and maximum difference between the frequency response of the model and the physical pump. Table 4.7 shows the frequency domain accuracy of the Locked Grey box model.

Table 4.7: Locked Grey Box model verification - Frequency domain.

O [%]	A [%]	\bar{E}_M [dB]	$E_M^{(max)}$ [dB]	\bar{E}_P [deg]	$E_P^{(max)}$ [deg]	Verification
-75	5	0.78	2.43	7.6	57.1	✗
-75	10	0.32	0.93	8.3	51.2	✗
-75	20	0.29	1.14	10.4	63.2	✗
-50	5	0.57	1.97	7.8	58.9	✗
-50	10	0.46	1.83	8.9	50.8	✗
-50	20	0.36	1.91	11.6	57.3	✗
-25	5	0.45	1.43	6.8	54.3	✗
-25	10	0.59	2.13	8.6	49.1	✗
-25	20	0.44	2.03	11.3	54.2	✗
25	5	0.45	1.43	6.8	54.3	✗
25	10	0.59	2.13	8.6	49.1	✗
25	20	0.44	2.03	11.3	54.2	✗
50	5	0.57	1.97	7.8	58.9	✗
50	10	0.46	1.83	8.9	50.8	✗
50	20	0.36	1.91	11.6	57.3	✗
75	5	0.78	2.43	7.6	57.1	✗
75	10	0.32	0.93	8.3	51.2	✗
75	20	0.29	1.14	10.4	63.2	✗

The verification column in Table 4.7 indicates that the model does not meet the specification criteria in Section 1.3. This is mostly due to the large deviations on mean and maximum phase. In order to verify the accuracy of the Free Grey box model to identify if it have the same accuracy problems, the same procedure is executed for the free Grey box model. The results are shown in Table 4.6.

Table 4.8: Free Grey Box model verification - Frequency domain.

O [%]	A [%]	\bar{E}_M [dB]	$E_M^{(max)}$ [dB]	\bar{E}_P [deg]	$E_P^{(max)}$ [deg]	Verification
-75	5	0.39	1.17	3.4	32.4	✓
-75	10	0.23	0.75	3.4	26	✓
-75	20	0.33	1.15	4.6	36.7	✗
-50	5	0.18	0.4	3.1	32.9	✓
-50	10	0.25	0.62	4	23.3	✓
-50	20	0.17	0.62	4.6	32.1	✓
-25	5	0.19	0.39	3.2	27.3	✓
-25	10	0.37	1.01	4.2	20.8	✓
-25	20	0.21	0.58	4.6	30.4	✓
25	5	0.19	0.39	3.2	27.3	✓
25	10	0.37	1.01	4.2	20.8	✓
25	20	0.21	0.58	4.6	30.4	✓
50	5	0.18	0.39	3.1	32.9	✓
50	10	0.25	0.62	4	23.3	✓
50	20	0.17	0.62	4.6	32.1	✓
75	5	0.39	1.17	3.4	32.4	✓
75	10	0.23	0.75	3.4	26	✓
75	20	0.33	1.15	4.6	36.7	✗

From the verification column in Table 4.8 it is shown that the accuracy of this model is much better than the locked Grey box model. Only in the two most extreme situations with $\pm 75\%$ offset and 20% amplitude, the accuracy of the model is below the criteria. A possible explanation for this is that the modeled spring in the cylinder is linear, but it may be non-linear.

Also in order to verify the time response of the two models, a test with a stochastic wave input with $H_s = 100\%$ and $T_p = 0.5s$ is used as input to the pump. Recall that during the optimization a similar dataset was used, albeit with a slower significant wave period, and therefore these measurements have not been used to optimize the model. The resulting swash plate angle α and the internal valve position u have been logged using Bodac software. For the Locked Grey box model (Table 4.5), the following comparison plots are created, see Figure 4.6

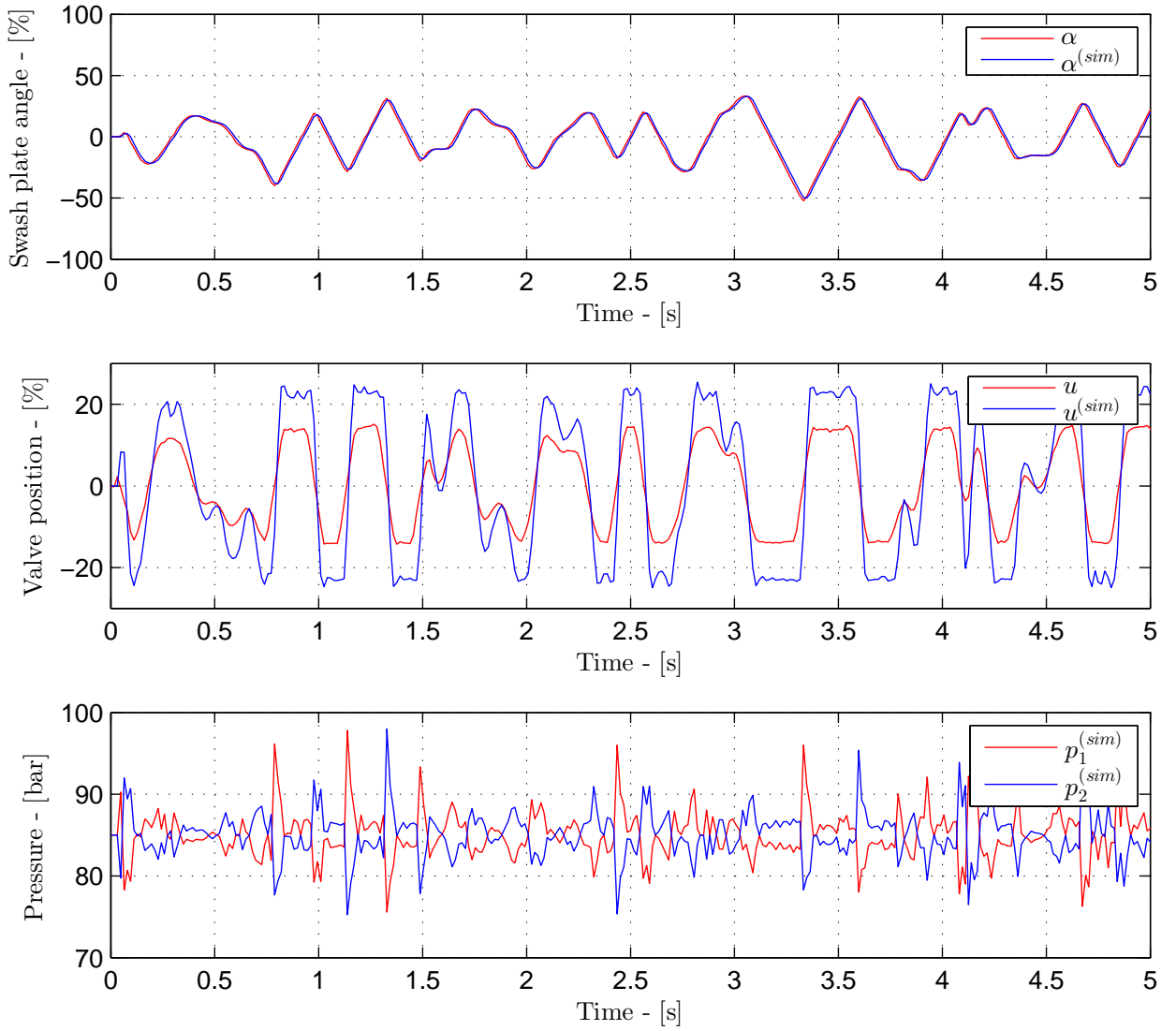


Figure 4.6: Comparison of internal measured and simulated values for the locked parameter model.

As shown in Figure 4.6 there are three plots from top to bottom: A comparison of measured angle α and simulated angle $\alpha^{(sim)}$, a comparison of measured valve position u and simulated valve position $u^{(sim)}$ and a plot showing the two simulated internal pressures $p_1^{(sim)}$ and $p_2^{(sim)}$. From this plot it is shown that the simulated response of the swash plate angle follows the measured response, and the simulated internal pressures are within limits of 0-170 bar. However, the model does not catch the measured internal position of the valve; the simulated valve $u^{(sim)}$ have a larger response than the measured valve position. The reason for this may be an inaccurate model of the cylinder chamber volumes in relation with the cylinder area.

To further strengthen this theory, lets move the focus to the free Grey box model. Comparison plots in the time domain using the free Grey box model is shown in Figure 4.7.

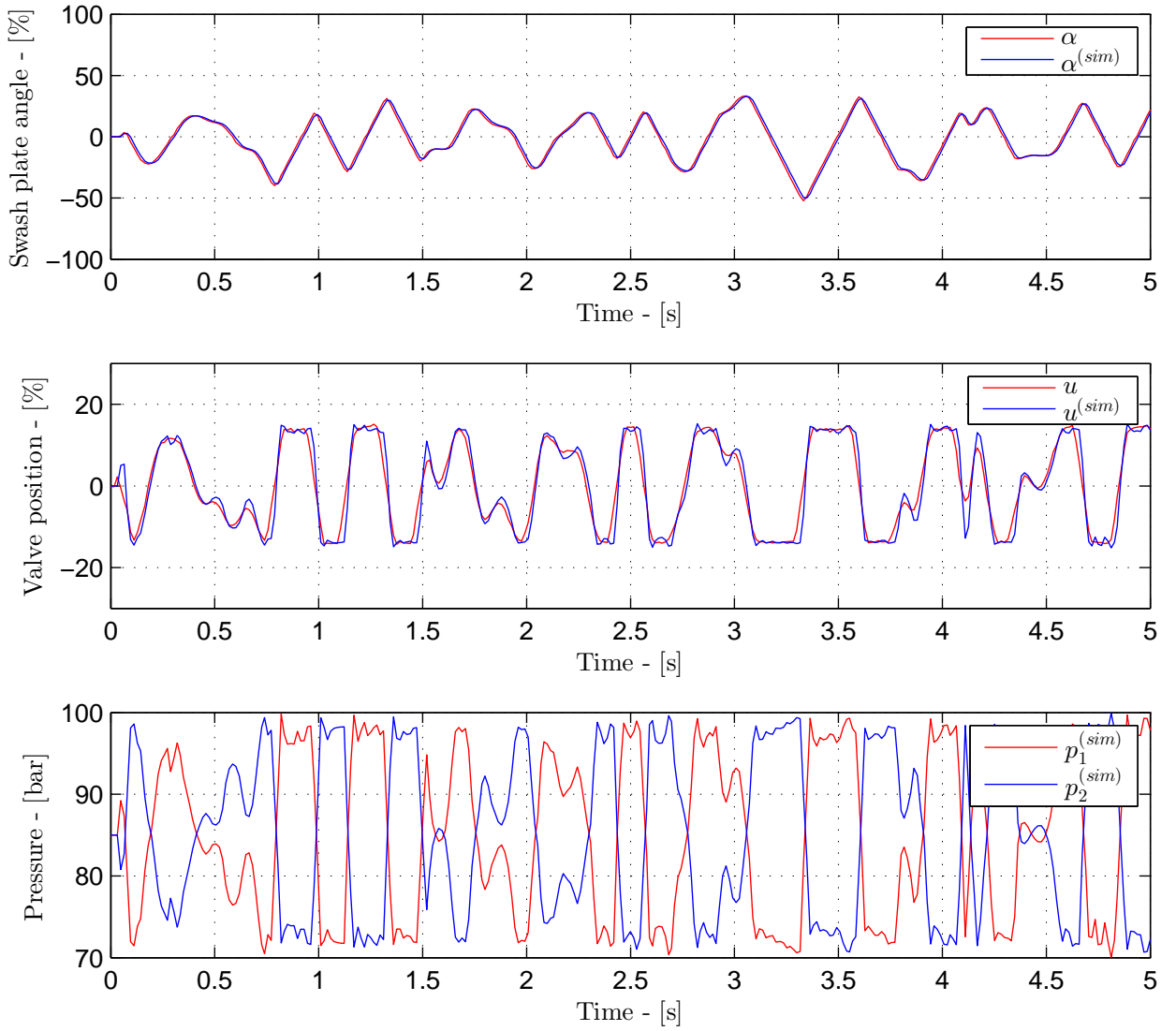


Figure 4.7: Comparison of internal measured and simulated values for the free parameter model.

In Figure 4.7, it is shown that the Free Grey box model manages to adjust its parameters so that the measured and simulated valve position is similar. A huge contribution to this is the freedom to change the cylinder area, as the free Grey box model have a third of the cylinder area compared to the locked Grey box model.

The accuracy of two models in the time domain is also assessed using the verification method in Section 2.7. The maximum and mean deviation between the measured and simulated valve position is shown for the two models in Table 4.9

Table 4.9: Grey Box model verification - Time domain.

Model	\bar{E}_t [%]	$E_t^{(\max)}$ [%]	Verification
Locked	7.86	18.49	✗
Free	1.83	9.47	✓

The upper limits for mean and maximum deviations in percentage is given in the design criteria in Section 1.3. The locked Grey box model does not pass the upper limit in terms of either maximum deviation or mean deviation. The free Grey box model passes the design criteria.

After this verification procedure, the free Grey box model appears to be the best model to reproduce the dynamics in the swash plate angle actuating circuit. Therefore the free Grey box model parameters are used as initial values in the SimulationX model of the pump. In the next section, the ripple flow effect is analyzed to determine whether it is necessary to include the ripple flow in a simulation.

4.5 Analysis of the Ripple Flow Effect

In this section, the effect of the ripple flow is analyzed in two situations. The ripple flow is generated from the piston movements inside the pump and consists of high-frequent, low-amplitude flow spikes. This behavior is further explained back in Subsections 3.4.3 through 3.4.5. In order to produce the results in this chapter, the SimulationX model of the pump from Section 3.5 is used. This model includes the simplified ripple flow.

The ripple flow is shown to have a high frequency and a low amplitude. This brings up the question whether a simulation of this ripple flow is really necessary. If the output of the pump is connected to a hose, the damping may cancel the effect of the ripple before it reaches any component. This is tested using a simple SimulationX diagram with the modeled pump with ripple flow included. The block diagram is shown in Figure 4.8.

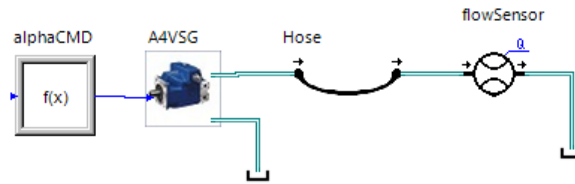


Figure 4.8: Block diagram of the SimulationX program used to test ripple frequencies over a hose.

The block diagram in Figure 4.8 contains from left to right a swash plate angle command, the A4VSG pump connected to a tank on port B and a hose and flow sensor on port A. The purpose of this simulation is to compare the flow generated by the pump with the measured flow after the hose. The hose is 3m long with an inner diameter of 10mm and standard settings for damping and wall roughness. The output of this simulation is shown in Figure 4.9.

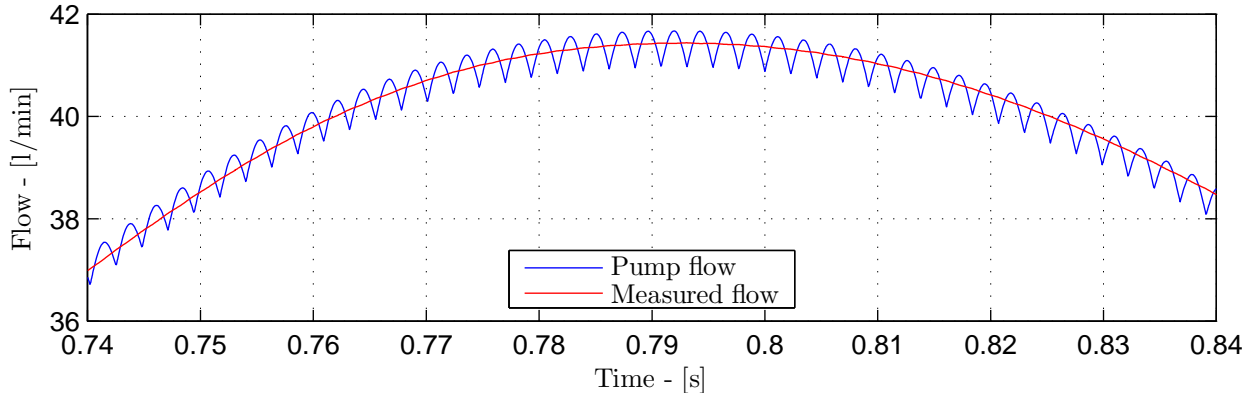


Figure 4.9: Comparison of flow before and after hose.

As shown in Figure 4.9 the effects of the ripple is canceled out in the hose. This concludes the inefficiency of simulating the ripple flow if a hose is used on the output of the pump. Another scenario worth investigation is a pressure relief valve connected to the output of the pump. If its resonance frequency is triggered by the ripple flow it could case large noises and perhaps damage the valve. This is tested using a different SimulationX program which is shown in Figure 4.10.

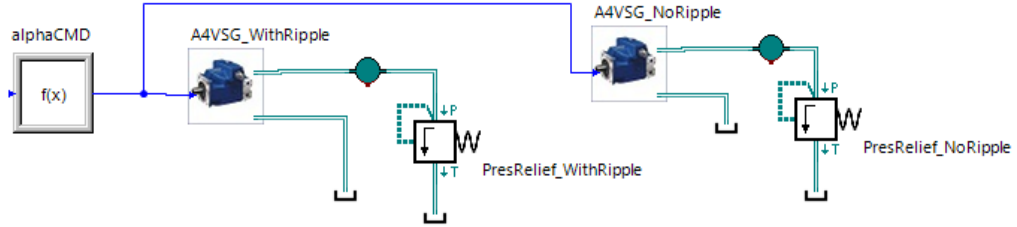


Figure 4.10: Simulation X Block diagram for pressure relief valve test.

This block diagram has two hydraulic circuits; the left part contains an A4VSG pump with ripple simulation and the right part contains an A4VSG without ripple simulation. Each of the two pumps are connected to an identical set of a volume and a pressure relief valve. The volume is sized to $0.1dm^3$. The pressure relief valves are configured with an undamped opening time equal to the period of the ripple strokes. This is done to provoke a resonance behavior in the valve when subjected to the ripple strokes. With the pumps configuration the ripple frequency is $2f_r = 435Hz$. f_r is doubled because one simplified ripple period contains two ripple strokes. The undamped opening is therefore set to $1/435Hz \approx 2.3ms$. The angle command to the pump is static at 50%. The result from this simulation is shown in Figure 4.11.

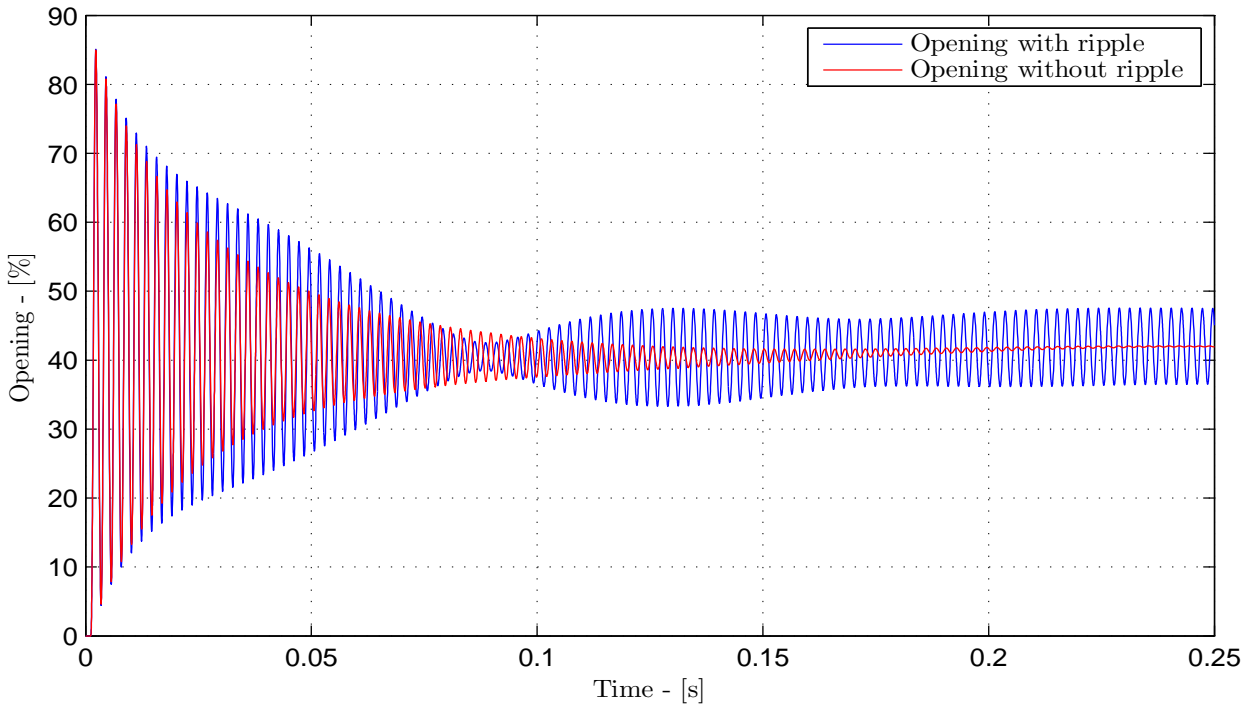


Figure 4.11: Simulated pressure relief valve opening percentage.

In Figure 4.11 the opening of the two pressure relief valves are shown. The blue curve is connected to the pump with ripple and the red is connected to the pump without ripple. During the end of the simulation from $t = 0.15s$ the blue curve clearly shows signs of resonance compared to the baseline which is the red curve. Near the end the oscillations reaches steady state between 35% and 48%. This simulation shows that the relief valve tested is affected by the ripple strokes, but whether this could be reproduced in a real experiment have not been tested.

Since the ripple flow makes such a small difference when the pump is connected to a hose, it can be favorable to neglect this to preserve computational power.

This result concludes the non-linear simulation model of the A4VSG pump, and the next chapter will focus on the design and control of a hydraulic load circuit.

Chapter **5**

Hydraulic Load Simulation Circuit

In this chapter the second part of the master thesis is presented. The purpose of this chapter is to elaborate the dynamics of the two hydraulic circuits and present a control system design which should control the shaft torque on one circuit and the rotational shaft speed using the second circuit. The shaft torque controller circuit is hereby called the “load circuit” and the speed control circuit is hereby called the “supply circuit”. An overview of the test setup for the two hydraulic circuits is presented in Section 5.1. Afterwards in Sections 5.2 and 5.3, a mathematical model of the load circuit and supply circuit is presented. These models are linearized to design linear control systems to control the shaft speed and load pressure in Section 5.4. In order to make an accurate non-linear simulation model of the two hydraulic circuits, the friction in the two motors is modeled in Section 5.5. To summarize the entire simulation model of the setup, a SimulationX model is presented in Section 5.6. Finally, an active heave compensation simulation model is presented which can be used to generate the load pressure and shaft speed reference in Section 5.7.

5.1 Physical Test Bench Description

To simulate a physical load scenario acting on the Bosch Rexroth A4VSG pump during active heave compensation, a physical simulation circuit is developed. The main idea is to use two hydraulic circuits that are connected to each other via a mechanical shaft. One of the circuits is controlled using the closed loop pump described in Chapter 3, and the second circuit is controlled using a Parker servo valve described in Appendix D.6. The two Parker motors are described in Appendix D.4. These two motors are connected using a mechanical coupling, which connects the two closed hydraulic loops. Both Parker motors are variable displacement motors, however they are fixed during the project to the maximum of $60\text{cm}^3/\text{rev}$. An illustration of the physical test bench is given in Figure 5.1.

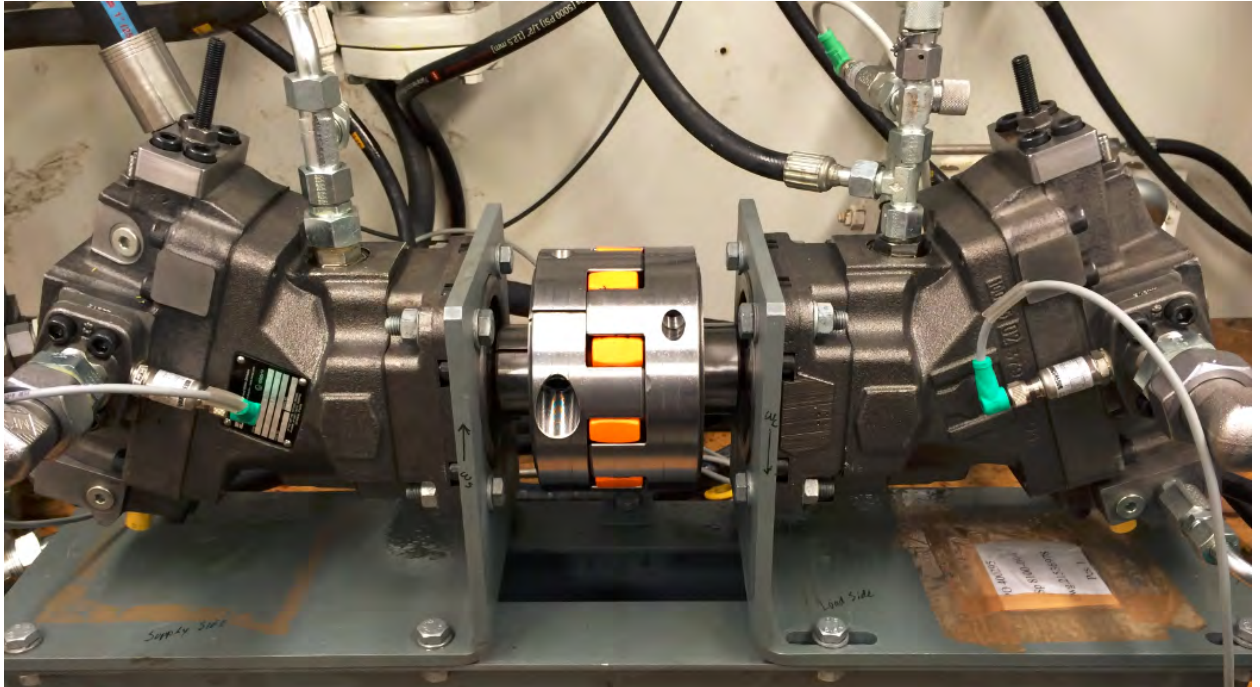


Figure 5.1: Picture of the physical test bench, where the two motors are connected using a mechanical coupling.

In Figure 5.1, both Parker motors are shown mounted on the test bench with a mechanical coupling fitted between them. All instrumentation as well as mounting of the physical test bench was carried out during the master thesis.

The pressure transmitters are of the 2-wire current transmitters type. They had to be connected to a PLC since the NI myRIO DAQ does not support current sensing at the I/O ports. The PLC reads the current signal from the pressure transmitters and provide the NI myRIO with voltage signals ranging between $1V - 5V$. The control systems are programmed using NI's LabVIEW programming environment, and run on the NI myRIO. The control systems are implemented using a difference equation which will reduce the complexity of implementing the controller later on a PLC if the company would like to do so. A picture showing the PC running the LabVIEW interface is given in Figure 5.2.



Figure 5.2: Laptop running LabVIEW for monitoring and control of the load circuit. The hand held controller to the left is used to set speed and load references.

It is desirable to adjust the shaft rotational speed and the load pressure across the load motor using analog inputs. A radio controller have been reconfigured to use the two potentiometers located in the right joystick to generate such analog voltage signal. The joystick movements have been configured as shown in Figure 5.3.

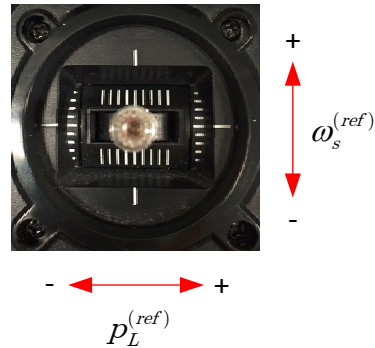


Figure 5.3: Overview of the analog joystick controllers.

The rotational speed of the coupling is measured using the time between two rising pulses from an inductive sensor. The inductive sensor is mounted in such way that the signal is positive when the inductive sensor is positioned over the metal part of the coupling. A picture of the mounting is given in Figure 5.4.



Figure 5.4: Inductive sensor fitting. Here shown when the output signal is false.

The equation describing the measured rotational speed due to the inductive pulse signal is given by Equation (5.1).

$$\omega_s = \frac{2\pi}{10\Delta T} \text{sign}(\alpha^{(ref)}) \quad (5.1)$$

- where:
- ω_s The rotational velocity of the shaft/coupling.
 - $\alpha^{(ref)}$ The reference control signal to the A4VSG pump.
 - ΔT The measured time between each rising pulse.
 - 10 The number 10 represents the number of pulses per revolution.

It is important to note that the measured speed around zero velocity will result in inaccurate measurements. Also a logic switch between positive and negative speed is added via the $\text{sign}(\alpha^{(ref)})$ since a single pulse sensor can not provide information about the direction. In future implementation/installation, MacGregor should introduce a more sophisticated sensor to measure the coupling rotational velocity. A complete schematic of the setup is shown in Figure 5.5.

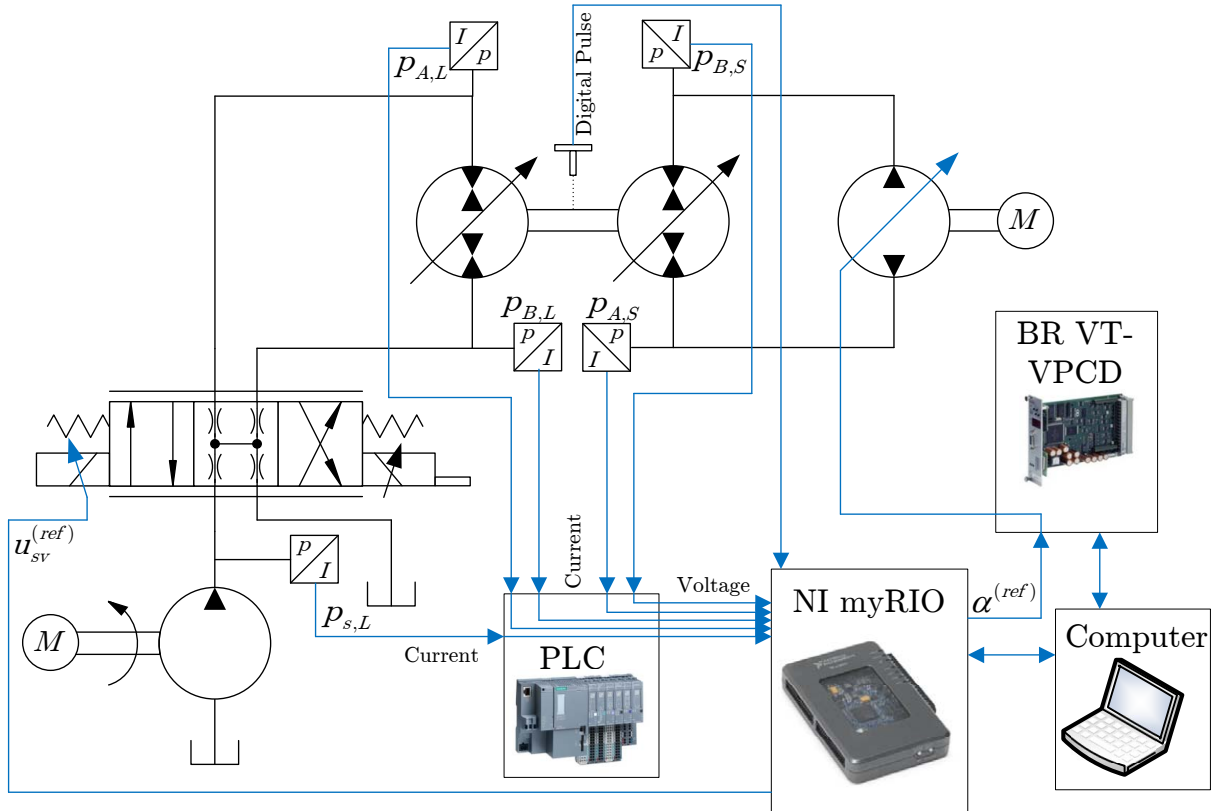


Figure 5.5: Load circuit electronic layout. Picture of NI myRIO, BR VT-VPCD and Siemens PLC is taken from [1], [2] and [3] respectively.

Now that the test setup is described, the next section focuses on a mathematical model of the hydraulic load circuit.

5.2 Load Circuit Analysis

This section presents a simplified mathematical model of the hydraulic circuit that is controlled to generate a mechanical load on the coupling between the two motors, also known as the load circuit. The circuit consists of a Parker servo valve described in Appendix D.6 and a Parker motor described in Appendix D.4. The valve is controlled to control the load torque on the motor shaft. To design an accurate controller, a linearized model of the hydraulic load circuit is found by setting up the mathematical model of the hydraulic circuit. A simplified overview of the hydraulic load circuit is shown in Figure 5.6.

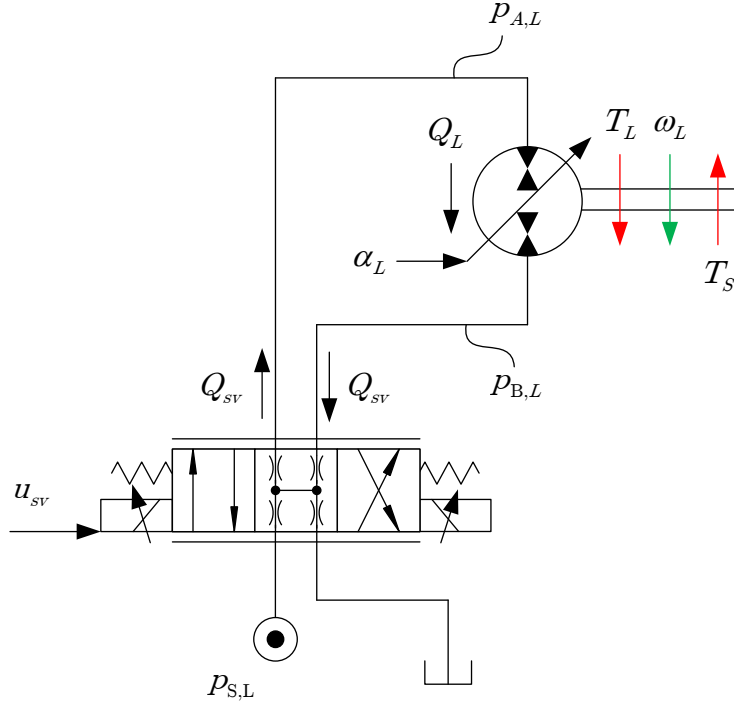


Figure 5.6: Simplified overview of the hydraulic load circuit.

From the figure, several equations are presented to model the hydraulic circuit. The first equation describes the hydraulic flow through the servo valve, and it is given by Equation (5.2).

$$Q_{sv} = u_{sv} K_{sv} \sqrt{\frac{1}{\rho} (p_{s,L} - \frac{u_{sv}}{|u_{sv}|} p_L)} \quad (5.2)$$

- where: Q_{sv} The flow through the servo valve.
- u_{sv} Actual servo valve spool opening.
- K_{sv} Servo valve orifice opening coefficient.
- $p_{s,L}$ Load circuit supply pressure.
- p_L Load pressure across the motor.

The load pressure p_L introduced in Equation (5.2) is defined by Equation (5.3).

$$p_L = p_{A,L} - p_{B,L} \quad (5.3)$$

The orifice equation describing the flow through the servo valve is non-linear and has to be linearized in order to obtain a linear expression of the valve flow. Bear in mind that the linearized model of the valve flow is used to design a control system in a later section. The linearized valve flow is given by Equation (5.4).

$$Q_{sv} \approx K_{qu} u_{sv} - K_{qp} p_L \quad (5.4)$$

where: K_{qu} Spool opening flow gain coefficient.

K_{qp} Pressure flow gain coefficient.

The coefficients K_{qu} and K_{qp} describing the linearized valve flow given by Equations (5.4) is found by using first order Taylor expansions. The coefficients are given by Equation (5.5) and (5.6).

$$K_{qu} = \frac{\partial Q_{sv}}{\partial u_{sv}} \Big|_{(ss)} = K_{sv} \sqrt{\frac{1}{\rho} \left(p_{s,L} - \frac{u_{sv}^{(ss)}}{|u_{sv}^{(ss)}|} p_L^{(ss)} \right)} \quad (5.5)$$

$$K_{qp} = \frac{\partial Q_{sv}}{\partial p_L} \Big|_{(ss)} = \frac{|u_{sv}^{(ss)}| K_{sv}}{2 \sqrt{\rho \left(p_{s,L} - \frac{u_{sv}^{(ss)}}{|u_{sv}^{(ss)}|} p_L^{(ss)} \right)}} \quad (5.6)$$

When the motor shaft rotates, a flow trough the motor is present. This flow is referred to as the load flow and it is expressed using Equation (5.7).

$$Q_L = K_L(\alpha_L) \omega_L \quad (5.7)$$

where: Q_L The load flow through the motor.

$K_L(\alpha_L)$ Motor gain coefficient.

ω_L Motor shaft rotational speed.

α_L Motor swash plate angle.

Due to the pressure drop across the motor a resulting torque on the shaft is present. This torque is described using Equation (5.8).

$$T_L = K_L(\alpha_L) p_L \quad (5.8)$$

where: T_L Load torque.

p_L Load pressure across the motor.

Equations (5.7) and (5.8) uses a gain coefficient which is dependent on the swash plate angle of the motor α_L . This gain is expressed using Equation (5.9).

$$K_L(\alpha_L) = \frac{\alpha_L}{\alpha_{L,max}} \frac{V_{m,max}}{2\pi} \quad (5.9)$$

where: $\alpha_{L,max}$ Maximum swash plate angle of the Parker V12 motor.

$V_{m,max}$ Maximum motor displacement.

The dynamic behavior of the hydraulic load circuit is described by setting up the main governing equations describing the pressure gradients and the shaft acceleration. The load pressure gradient is given by Equation (5.10).

$$\dot{p}_L = \frac{2\beta}{V_{L0}}(Q_{sv} - Q_L) \quad (5.10)$$

where: \dot{p}_L Load pressure gradient.
 β The hydraulic fluid bulk modulus.
 V_{L0} The dead volume on each side of the motor.

The acceleration of the shaft is a result of difference between the load torque T_L and the supply torque T_s . The shaft acceleration is described using Equation (5.11).

$$\dot{\omega}_L = \frac{T_L - T_s - \omega_L c}{J_{eff}} \quad (5.11)$$

where: $\dot{\omega}_L$ Motor shaft acceleration.
 T_s Supply torque generated by the hydraulic supply circuit.
 J_{eff} The effective inertia of both the motors and the connecting shaft.
 c Rotational friction coefficient.

Bear in mind that the rotational friction coefficient c is introduced to have a linear friction model. A non-linear friction model is introduced later in Section 5.5 which will be used in the non-linear simulation model of the hydraulic load circuit. The aim is to obtain a linearized model which is used to find a suitable control system that provides sufficient performance. The linearized model is found by taking the Laplace transform of the two governing differential equations given in Equations (5.10) and (5.11). The resulting two equations in the s-domain are given in Equations (5.12) and (5.13).

$$p_L(s) = \frac{1}{s} \frac{2\beta}{V_{L0}} (K_{qu} u_{sv}(s) - K_{qp} p_L(s) - K_L(\alpha_L) \omega_L(s)) \quad (5.12)$$

$$\omega_L(s) = \frac{1}{s} \frac{K_L(\alpha_L) p_L(s) - T_s(s) - \omega_L(s) c}{J_{eff}} \quad (5.13)$$

These two equations are combined and used to find linear relationships between input and output in the load circuit. To extract these transfer functions, a block model is drawn to illustrate the load circuit dynamics. The block model is shown in Figure 5.7.

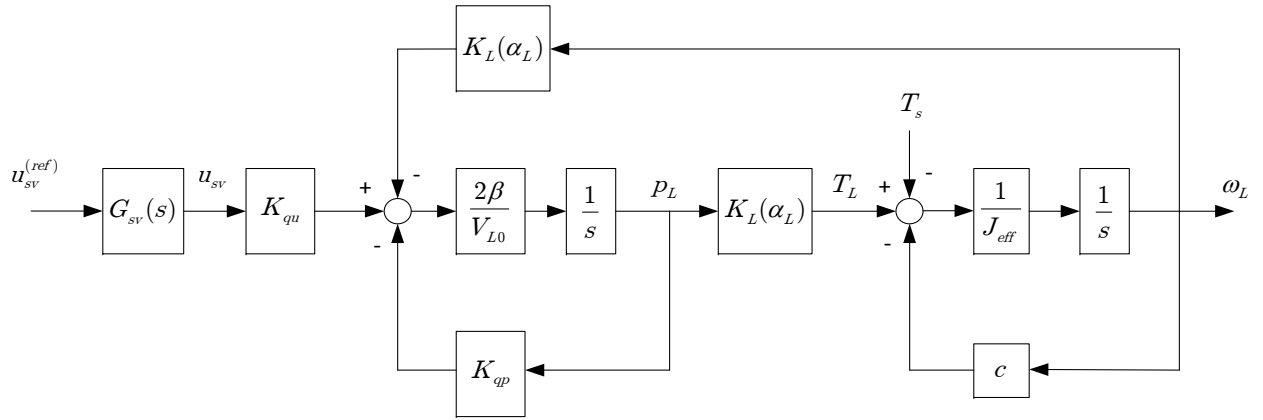


Figure 5.7: Load circuit block diagram.

From the block diagram in Figure 5.7 two main transfer functions are found. The first one describes the relationship between the input servo valve reference $u_{sv}^{(ref)}$ and the load pressure p_L . In this situation the shaft speed ω_L can be seen as a disturbance to the plant. This transfer function is given in Equation (5.14).

$$G_{p_L}(s) = \frac{p_L(s)}{u_{sv}^{(ref)}(s)} = G_{sv}(s) \frac{\frac{K_{qu} \frac{2\beta}{V_{L0}}}{s + \frac{2\beta}{V_{L0}} K_{qp}}}{1} \quad (5.14)$$

The second transfer function describes the relationship between the input servo valve reference $u_{sv}^{(ref)}$ and the output shaft speed ω_L . In this situation the torque T_s generated by the supply circuit can be seen as a disturbance to the plant. The transfer function is shown in Equation (5.15).

$$G_{\omega_L}(s) = \frac{\omega_L(s)}{u_{sv}^{(ref)}(s)} = G_{sv}(s) \frac{\frac{K_{qu} K_L(\alpha_L) \frac{2\beta}{V_{L0} J_{eff}}}{s^2 + \frac{2\beta J_{eff} K_{qp} + c V_{L0}}{V_{L0} J_{eff}} s + \frac{2\beta K_{qp} c + 2\beta K_L^2(\alpha_L)}{V_{L0} J_{eff}}}}{1} \quad (5.15)$$

The two transfer functions $G_{p_L}(s)$ and $G_{\omega_L}(s)$ are useful when designing a control system to either control the load pressure p_L or the shaft speed ω_L . However, both plants are originally non-linear, and the controllers should be designed in a conservative way when using linearized models.

In this section the non-linear load circuit was described. From the non-linear model, a linearized plant was identified for the sole purpose of designing a linear control system. The design of the control system is described in Section 5.4. However in the next section, a model of the supply circuit is introduced.

5.3 Supply Circuit Analysis

As for the load circuit described in Section 5.2, a simplified model of the supply circuit is also created. This circuit should be able to control both the shaft speed with a suitable A4VSG swash plate angle controller. A drawing of the simplified hydraulic supply circuit is given in Figure 5.8.

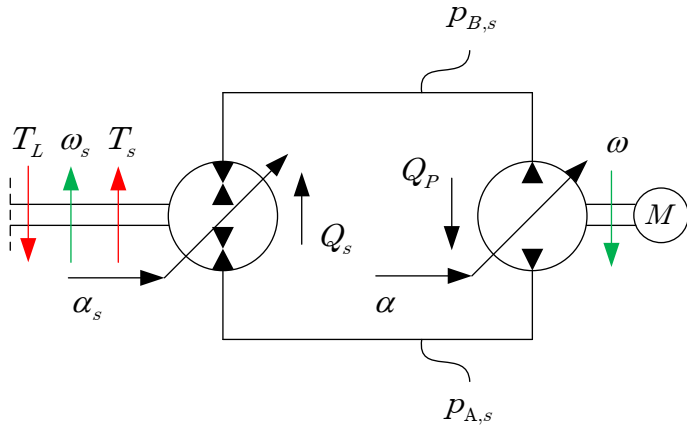


Figure 5.8: Supply circuit diagram.

By analyzing Figure 5.8, several equations are set up to describe the behavior of the hydraulic circuit. First the pump flow delivered by the Bosch Rexroth A4VSG is modeled using Equation (5.16).

$$Q_P = K_P \alpha \quad (5.16)$$

where: Q_P The delivered flow from the A4VSG variable piston pump.
 K_P Flow/pressure gain coefficient as function of α .
 α The actual swash plate angle of the variable piston pump.

The flow/pressure gain K_P introduced in Equation (5.16) is given by Equation (5.17).

$$K_P = \frac{1}{\alpha_{max}} \frac{V_{d,max}}{2\pi} \omega \quad (5.17)$$

where: α_{max} Maximum swash plate angle of the variable piston pump.
 $V_{d,max}$ Maximum pump displacement.
 ω A4VSG pump shaft speed.

The variable piston pump have been analyzed in details in Chapter 3 where the swash plate dynamics was identified using a Black box model and a non-linear gray box model. In this part of the project the most conservative Black box model is used, since a linear model is needed to design a sufficient control system. The equation describing the swash plate dynamics is given in Equation (5.18). The transfer function of the pump was identified in the Results Section 4.2.1. The referenced Equation (4.1) is the template of the transfer function, and the values for the five constants are extracted from Table 4.1 where Amplitude = 5% and Offset = 25%.

$$G_{Pump}(s) = \frac{\alpha(s)}{\alpha^{(ref)}(s)} = G_{est}(s) \quad (5.18)$$

where: $\alpha^{(ref)}(s)$ Swash plate angle reference signal.
 $G_{est}(s)$ Estimated Black box transfer function in Section 4.2.1.

Further the supply flow and torque across the motor is expressed using two simplified expressions in Equations (5.19) and (5.20).

$$Q_s = K_s(\alpha_s)\omega_s \quad (5.19)$$

$$T_s = K_s(\alpha_s)p_s \quad (5.20)$$

where: Q_s Supply circuit flow.

T_s Supply circuit torque.

ω_s Rotational speed of the shaft, $\omega_s = -\omega_L$.

p_s Pressure difference across the motor.

$K_s(\alpha_s)$ Supply circuit motor gain.

α_s Supply circuit motor swash plate angle.

In Equation (5.20) the supply pressure p_s is present. This pressure is defined as the pressure difference across the supply motor. The pressure is defined using Equation (5.21).

$$p_s = p_{A,s} - p_{B,s} \quad (5.21)$$

where: $p_{A,s}$ Hydraulic pressure at pump port A.

$p_{B,s}$ Hydraulic pressure at pump port B.

The motor gain $K_s(\alpha_s)$ is found by using Equation (5.22).

$$K_s(\alpha_s) = \frac{\alpha_s}{\alpha_{s,max}} \frac{V_{m,max}}{2\pi} \quad (5.22)$$

where: $\alpha_{s,max}$ The maximum swash plate angle of the supply circuit motor.

Using the equations presented in this section, it is possible to set up the main governing differential equations describing the supply circuit dynamics. The supply pressure gradient is expressed in Equation (5.23).

$$\dot{p}_s = \frac{2\beta}{V_{s0}}(Q_p - Q_s) \quad (5.23)$$

where: \dot{p}_s Supply pressure gradient.

β Hydraulic fluid bulk modulus.

V_{s0} Dead volume on each side of the motor.

Since the shaft speed should be controlled, the differential equation describing the rotational acceleration of the shaft is described. The rotational acceleration of the shaft is given in Equation (5.24).

$$\dot{\omega}_s = \frac{T_s - T_L - \omega_s c}{J_{eff}} \quad (5.24)$$

where: $\dot{\omega}_s$ Rotational acceleration of the shaft.

To represent the hydraulic supply circuit using a block diagram, the Laplace transformed equations of the two governing differential equations are evaluated. The resulting two equations in the Laplace domain are given by Equations (5.25) and (5.26).

$$p_s(s) = \frac{1}{s} \frac{2\beta}{V_{s0}} (K_P \alpha(s) - K_s(\alpha_s) \omega_s(s)) \quad (5.25)$$

$$\omega_s(s) = \frac{1}{s} \frac{T_s(s) - T_L(s) - \omega_s(s)c}{J_{eff}} \quad (5.26)$$

These two equations are used to construct a block diagram describing the linear dynamics of the supply circuit. The block diagram is shown in Figure 5.9.

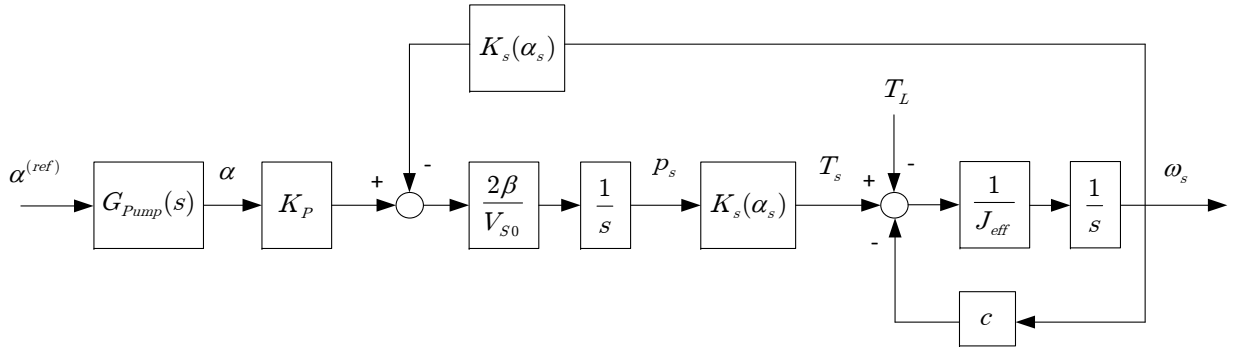


Figure 5.9: Supply circuit block diagram.

Figure 5.9 is used to find two transfer functions describing the dynamics. The first transfer function defines the relationship between the input swash plate angle reference $\alpha^{(ref)}$ and the output supply pressure p_s . The resulting transfer function is given in Equation (5.27).

$$G_{p_s}(s) = \frac{p_s(s)}{\alpha^{(ref)}(s)} = G_{Pump}(s) \frac{K_P \frac{2\beta}{V_{s0}}}{s} \quad (5.27)$$

Since the shaft speed is controlled using the variable displacement pump, the dynamics between the input swash plate reference $\alpha^{(ref)}$ and the output ω_s is described by the transfer function in Equation (5.28).

$$G_{\omega_s}(s) = \frac{\omega_s(s)}{\alpha^{(ref)}(s)} = G_{Pump}(s) \frac{K_P \frac{2\beta K_s(\alpha_s)}{V_{s0} J_{eff}}}{s^2 + \frac{c}{J_{eff}} s + \frac{2\beta K_s^2(\alpha_s)}{V_{s0} J_{eff}}} \quad (5.28)$$

In this section, a linear model of the load circuit was presented. Using this model, a transfer function describing the system was identified and will in the next section be used to design a linear control system.

5.4 Control System Design

In Sections 5.2 and 5.3 both the load and the supply circuit was analyzed in terms of linearized equations. These two hydraulic circuits are controlled using two separate Single Input, Single Output (SISO) control systems.

The load side control system is supposed to create a load situation by controlling the pressure difference across the Parker motor unit. This torque is seen as a disturbance in the supply circuit. The supply circuit shall control the rotational speed of the connection shaft between the two hydraulic loops analyzed in Sections 5.2 and 5.3. The rotational speed will again create a disturbance to the load circuit side, since the shaft rotation will generate a flow across the motor. A brief overview of the control loops are given in Figure 5.10, where the red stapled boxes contain the two respective control loops.

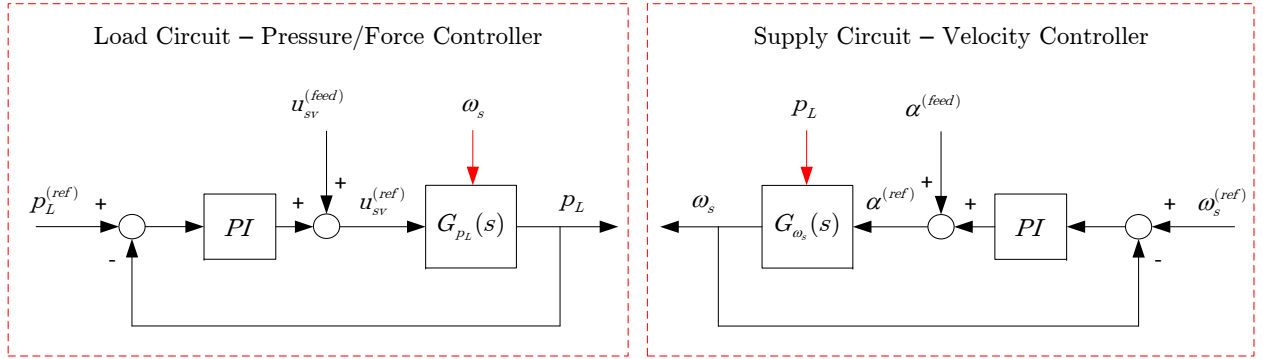


Figure 5.10: Control loops; using the load circuit to control the force/pressure and the supply circuit to control the shaft rotational speed.

In Figure 5.10, both controllers are chosen to be PI-controllers. The reason for using such a controller is explained by analyzing both of the plants $G_{p_L}(s)$ and $G_{\omega_s}(s)$ in open-loop. The control loops shall remove all steady state deviation for a step input when feedback is included. By looking at the transfer functions $G_{p_L}(s)$ and $G_{\omega_s}(s)$ it is clear that both of them are of type 0-systems, which means that the plant have no free integrators in the denominator. To ensure zero steady-state error for a step input, the open loop transfer function should have a free integrator in the denominator i.e. a type 1.system. This free integrator can be introduced by a PI-controller which is why a PI-controller is chosen. It should also be noted that the chosen servo valve linearization point is given by Equation (5.29).

$$u_{sv}^{(ss)} = 0.1 \quad \text{and} \quad p_L^{(ss)} = 0.0 \quad (5.29)$$

The two respective transfer functions are recalled from Equations (5.14) and (5.28) into Equations 5.30 and 5.31 respectively.

$$G_{p_L}(s) = \frac{p_L(s)}{u_{sv}^{(ref)}(s)} = G_{sv}(s) \frac{K_{qu} \frac{2\beta}{V_{L0}}}{s + \frac{2\beta}{V_{L0}} K_{qp}} \quad (5.30)$$

$$G_{\omega_s}(s) = \frac{\omega_s(s)}{\alpha^{(ref)}(s)} = G_{Pump}(s) \frac{K_P \frac{2\beta K_s(\alpha_s)}{V_{s0} J_{eff}}}{s^2 + \frac{c}{J_{eff}} s + \frac{2\beta K_s^2(\alpha_s)}{V_{s0} J_{eff}}} \quad (5.31)$$

The variables that are used to describe the transfer function coefficients are found by taking simplified measurements of the test set up. All the variables used are given in Table 5.1.

Table 5.1: Transfer function parameters.

Parameter	Value	Unit
K_{qu}	0.0035	-
K_{qp}	$5.61 \cdot 10^{-12}$	-
β	1400	MPa
V_{L0}	1.01	l
V_{s0}	1.52	l
K_P	0.0066	-
$K_s(\alpha_s)$	$9.5493 \cdot 10^{-6}$	-
c	0.2600	Ns/rad
J_{eff}	0.0733	kgm^2

By introducing a PI-controller in both control loops, it is possible to achieve zero steady-state error for a step input, since the PI-controller inclusion will make both plants a type 1-system. Also both plants are at all times subjected to disturbance from each other, and in such situations, a PI-controller is suitable since it is robust to reject noise/disturbance in the control loop. The tuning of the PI-controllers is carried out using bode shaping techniques. MATLAB offers an automated tuning algorithm to find suitable control parameters as long as the plant is known. In our situation, both plants are described using linearized transfer functions, and this gives us the ability to use MATLAB's tuning algorithm to tune the controller gains.

The PI-controller used in both control loops is described using the standard serial representation as shown in Equation (5.32).

$$G_{PI}(s) = K_p \left(1 + \frac{1}{T_i s} \right) \quad (5.32)$$

where: K_p Proportional gain part.

T_i Integration time constant.

The practical implementation of the PI-controller is chosen to be described as a difference equation. The PI-controller difference equation is given by Equation (5.33).

$$u(k) = u(k-1) + K_p e(k) + \left[\frac{K_p}{T_i} \Delta t - K_p \right] e(k-1) \quad (5.33)$$

where: $u(k)$ The current cycle control signal.

$u(k-1)$ The previous cycle control signal.

$e(k)$ The current cycle error signal.

$e(k-1)$ The previous cycle error signal.

Δt Time between each cycle interrupt.

To further increase the performance of both control loops, a feed forward signal is introduced in both control loops. By assuming that the delivered pump flow Q_P should be equal to the supply flow Q_s which is given by Equation (5.34), a feed forward signal describing the swash plate angle $\alpha^{(feed)}$ as a function of the reference velocity input signal $\omega_s^{(ref)}$ is created. The feed forward swash plate angle is given by Equation (5.35).

$$Q_P \approx Q_s \quad (5.34)$$

$$\alpha^{(feed)} = \frac{K_s(\alpha_s)}{K_P} \omega_s^{(ref)} \quad (5.35)$$

where: $\alpha^{(feed)}$ A4VSG swash plate angle feed-forward signal.
 $K_s(\alpha_s)$ Supply motor gain.
 $\omega_s^{(ref)}$ Rotational shaft speed reference signal.

The feed forward signal in the load circuit is dependent on both the servo valve spool opening u_{sv} , as well as the load pressure p_L across the load motor. The following assumption can be set up to find a suitable feed forward signal controlling the servo valve opening.

$$Q_L = -K_L(\alpha_L)\omega_s \approx Q_{sv} \approx K_{qu}u_{sv} - K_{qp}p_L \quad (5.36)$$

If the conservative steady state situation where $u_{sv}^{(ss)} = p_L^{(ss)} = 0$ is used to calculate the two linearized gains K_{qu} and K_{qp} , a conservative feed forward signal can be expressed using Equation (5.37).

$$u_{sv}^{(feed)} = -\frac{K_L(\alpha_L)}{K_{qu}} \omega_s^{(ref)} \quad (5.37)$$

where: $u_{sv}^{(feed)}$ Servo valve opening feed forward signal.
 K_P Flow/pressure gain coefficient.
 $K_L(\alpha_s)$ Supply circuit motor gain.
 K_{qu} The linearized servo valve opening gain.

By implementing both feed forward control signals after the controller as shown in Figure 5.10, it is possible to reduce the deviations from the reference control systems drastically. Also the controllers will compensate for less errors than without the feed forward. A more sophisticated and robust control system could be tuned if the time had allowed a deeper analysis of the control loops. This is one of the tasks that have to be further analyzed in order to achieve a fast and robust control system. Especially the load circuit is currently controlled using linear control theory, but the plant is heavily non-linear, and therefore a non-linear controller should be considered to control this loop in a satisfactory way [19].

The friction in the two Parker motors are until now described using a linear friction coefficient c . This was a simplification used to design a linear control system. However in the non-linear simulation model of the two circuits, a more accurate friction model is necessary. Therefore in the next section a non-linear friction model is presented.

5.5 Friction Model

The friction which is observed in the system is clearly a combination of a stiction friction and a static Coulomb friction as the rotational shaft velocity reaches higher speeds. It is desirable to combine the friction in both motors and find a relationship between the shaft speed and the friction. This is carried out by proposing a friction model [20], and map the friction in different rotational velocities. The proposed friction model is illustrated in Figure 5.11.

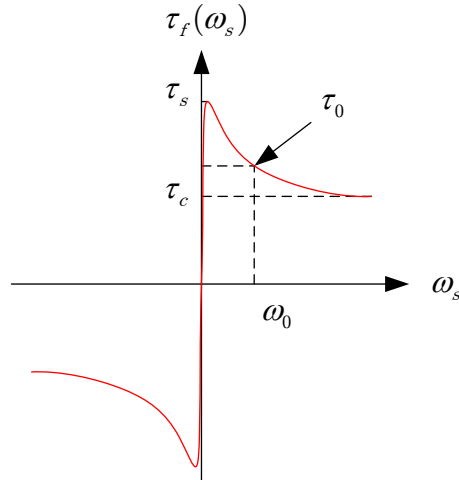


Figure 5.11: Illustration of the friction model.

Figure 5.11 introduce some new parameters describing the friction model used. The stiction friction τ_s describes the maximum friction torque which must be exceeded before the rotational coupling starts to rotate. At faster rotational velocities, the friction model reaches a steady state friction τ_c which is the constant Coulomb friction. Also a friction τ_0 exceeded at a given rotational speed ω_0 is specified since this is needed to find a suitable gradient on the curve. The mathematical description of the friction model is given in Equation (5.38).

$$\tau_f(\omega_s) = \tanh(r\omega_s) \left(\tau_c + (\tau_s - \tau_c)e^{-\frac{|\omega_s|}{\omega_0}} \right) \quad (5.38)$$

- where: $\tau_f(\omega_s)$ Model friction torque due to the rotational shaft velocity.
- τ_s The maximum friction exceeded in the model due to stiction.
- τ_c Coulomb friction during high rotational velocities.
- τ_0 Friction at ω_0 .
- ω_0 The rotational velocity at τ_0 .
- r Gradient factor describing the steepness of the *tanh* curve.

The unknown friction model parameters are included in the unknown parameter vector $\vec{\Phi}_f$, and it

is described using Equation (5.39).

$$\vec{\Phi}_f = \begin{bmatrix} r \\ \omega_0 \\ \tau_c \\ \tau_s \end{bmatrix} \quad (5.39)$$

The parameters can be tuned using optimization if the actual friction torque T_f is calculated through measurements of load pressures and accelerations during different velocities ω_s . By performing a manual test where the flow across the supply motor is manually controlled using the closed loop pump A4VSG, the load pressure p_L and the supply pressure p_s is measured as a function of the velocity ω_s . From Sections 5.2 and 5.3, the torques T_L and T_s are described as functions of the load pressures. An isolated model of the two Parker motors and the connecting shaft is given in Figure 5.12.

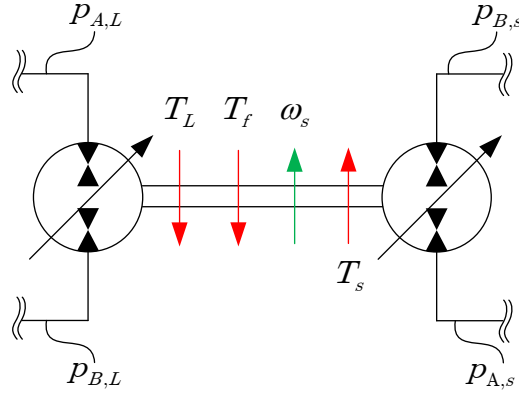


Figure 5.12: Simplified test bench model used to identify the friction.

From Figure 5.12, a governing differential equation describing the shaft torque equilibrium is expressed in Equation (5.40).

$$\dot{\omega}_s = \frac{T_s - T_L - T_f}{J_{eff}} \quad (5.40)$$

where: $\dot{\omega}_s$ Rotational acceleration found from numerical differentiation.

T_f Measured experimental friction torque.

Equation (5.40) is used to evaluate the friction torque as a function of the rotational velocity. By knowing the measured friction torque in our model, the objective is to find a set of friction model parameters that satisfies ($\tau_f \approx T_f$). The experimental friction torque T_f is calculated using Equation (5.41).

$$T_f(\dot{\omega}_s) = T_s - T_L - \dot{\omega}_s J_{eff} = K_s(\alpha_s)p_s - K_L(\alpha_L)p_L - \dot{\omega}_s J_{eff} \quad (5.41)$$

Where $K_s(\alpha_s)$ and $K_L(\alpha_L)$ are the gains due to the variable displacement of the Parker motors, and these are described in Sections 5.2 and 5.3. Equation (5.41) suggest that the rotational acceleration should be measured in order to calculate the friction torque. However, the measured rotational velocity is filtered using a zero-phase low pass filter (i.e. a filter used forward and backward in

time), and the rotational acceleration is obtained by numerically differentiating the filtered velocity afterwards. The measured pressures p_L and p_s are also filtered using the zero phase low pass filter. The results are used to identify the unknown parameters describing the friction model in Equation (5.38). The resulting friction model parameters are identified in Section 6.2.

With a detailed mathematical overview of the two hydraulic circuits, the control systems and the friction model, a complete SimulationX model is created in the next section.

5.6 SimulationX Model

From the load circuit model in Chapter 5 a SimulationX model is created. An overview of the model is shown in form of a block diagram in Figure 5.13.

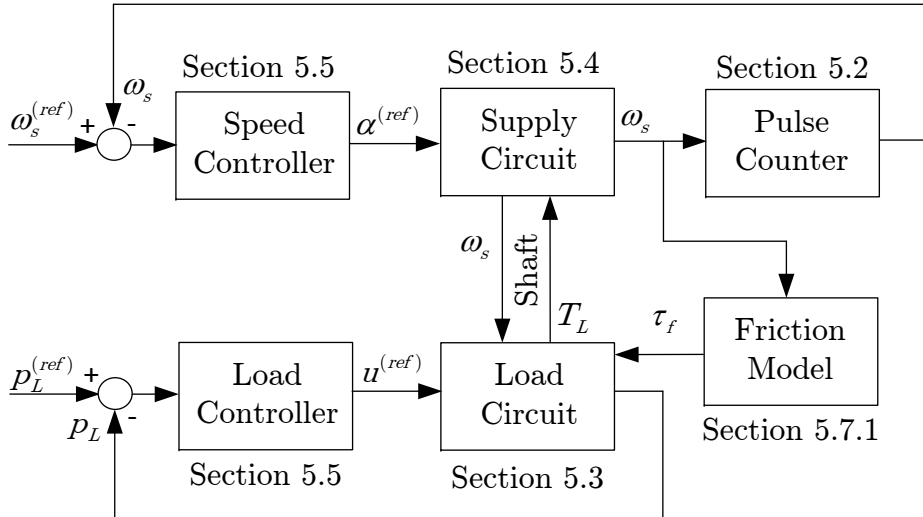


Figure 5.13: Block diagram of the SimulationX model of the load circuit.

In this figure, two inputs are shown, namely the reference speed $\omega_s^{(ref)}$ and reference load pressure $p_L^{(ref)}$. These two inputs, subtracted with the actual value of the respective parameter, is used as input to each controller, namely the speed controller and the load controller. These controllers are detailed in Section 5.4. The reference swash plate angle is sent to the A4VSG pump via its dynamics to produce flow on a closed loop motor. The Supply circuit model is detailed in Section 5.3. The reference valve position $u^{(ref)}$ controls the Parker servo valve which moves flow over its open loop motor. The load circuit is explained in detail in Section 5.2. The forces over the two motors are connected over a shaft where also a friction model is used as input. Finally a pulse counter system is used to measure the speed of the shaft when a pulse occurs.

There is a much more detailed description of this model in Appendix G, and this model is used to produce results in Section 6.3. In the next section, a simulation model of an active heave compensated crane is presented.

5.7 Active Heave Compensation Simulation Model

The main idea of constructing the hydraulic load circuit described in Chapter 5 is to simulate a small scale heave compensation situation offshore. MacGregor currently delivers several cranes that includes an Active Heave Compensation (AHC) ability. This system mainly consist of a winch connected to several hydraulic motors, who are placed in series with closed loop pumps i.e. A4VSG pumps analyzed in Chapter 3. The closed loop pump controls the direction and the magnitude of the flow inside the closed loop, which in the end will affect the rotational velocity of the wire drum. The small scale model is simplified to only use one single closed loop pump together with a single motor. Figure 5.14 illustrates an offshore crane during AHC of a fully submerged payload.

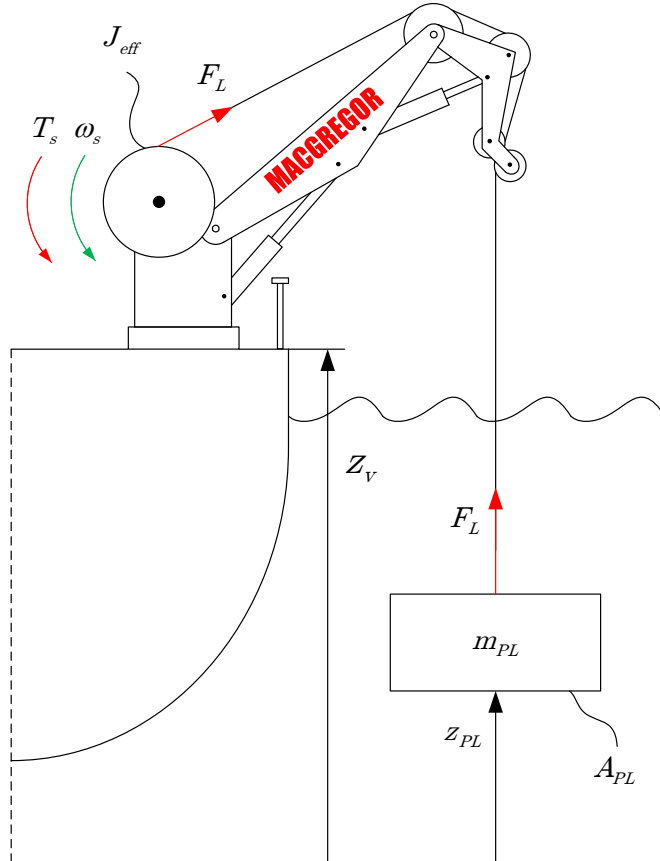


Figure 5.14: The AHC scenario offshore, where a payload shall be lowered and hoisted to the seabed with a closed loop hydraulic actuating circuit.

Figure 5.14 consists of a crane placed on floating vessel offshore. The crane has lowered a payload to reach a certain distance z_{PL} above the seabed. The objective of the AHC system is to compensate for the heave motion due to the vessels motion z_v . The heave motion of the vessel is assumed to follow a stochastic wave motion which is given by Equation(5.42).

$$z_v(t) = \sum_{n=1}^N z_{v,n}(t) \quad (5.42)$$

- where:
- N Number of wave components.
 - $z_v(t)$ The stochastic wave propagation in the heave direction.
 - $z_{v,n}(t)$ Each single wave component n given by the stochastic wave energy spectrum.

The theory regarding the generation of the stochastic wave motion is further explained in Appendix A. The rotational motion of the wire drum is given by recalling Equation (5.24) from Section 5.3, which is shown in Equation (5.43).

$$\dot{\omega}_s = \frac{T_s - T_L - \omega_s c}{J_{eff}} \quad (5.43)$$

- where:
- $\dot{\omega}_s$ Rotational acceleration of the wire drum.
 - T_s Torque supplied to the wire drum from the closed loop motor.
 - T_L Torque due to the wire tension connected to the payload.
 - ω_s Rotational wire drum velocity.
 - c Rotational damping coefficient.
 - J_{eff} Overall effective mass inertia of the combined motor and wire drum.

The rest of the differential equations needed are described in detail in Section 5.3. The main idea in this section is to simulate the load disturbance which will affect the wire drum due to the wire tension. The governing equation describing the payloads z-directional acceleration is given in Equation (5.44).

$$\ddot{z}_{PL} = \frac{F_L + F_{buoy} - F_{drag}}{m_{PL}} \quad (5.44)$$

- where:
- \ddot{z}_{PL} z-directional acceleration of the payload.
 - F_L The force due to the wire tension.
 - F_{buoy} Buoyancy force.
 - F_{drag} Drag force due to viscous friction in the sea water.
 - m_{PL} Gravitational mass of the payload.

A simplified drag force describing the drag force acting on the payload during movement in the sea water is given by Equation (5.45) [21].

$$F_{drag} = \frac{1}{2} \rho_s C_d A_{PL} \dot{z}_{PL}^2 \quad (5.45)$$

- where:
- ρ_s The sea water density.
 - C_d The drag force coefficient, dependent to the payload shape.
 - A_{PL} Payloads projected area in the z-direction.
 - \dot{z}_{PL} z-directional velocity of the payload.

The payload is assumed to be fully submerged during the simplified AHC scenario. When the payload is fully submerged in sea water, the payload will be subjected to a upwards force due to

the buoyancy effect. The buoyancy force is given by Equation (5.46).

$$F_{buoy} = \rho_s g V_{PL} \quad (5.46)$$

where: g Earth's gravity constant.

V_{PL} The submerged volume of the payload.

The wire force is modeled using a simple spring-damper model, where the spring stiffness is described by the wire elasticity. The spring stiffness is given by Equation (5.47).

$$k_w = \frac{E_w A_w}{L_w} \quad (5.47)$$

where: k_w Wire spring stiffness.

E_w Wire elasticity modulus.

A_w Wire cross-section area.

L_w Length of the wire.

The damping coefficient is defined to be 10% of the spring stiffness, and is given by Equation (5.48).

$$c_w = \frac{k_w}{10} \quad (5.48)$$

where: c_w Wire damping force coefficient.

The wire force is modeled using a piecewise function describing the wire force as a function of the payloads position relative to the wire drum rotation. The wire force is given by Equation (5.49).

$$F_L = \begin{cases} 0 & r_d\theta_s < z_{PL} - z_v \\ k_w(z_v - z_{PL} + r_d\theta_s) + c_w(\dot{z}_v - \dot{z}_{PL} + r_d\omega_s) & r_d\theta_s \geq z_{PL} - z_v \end{cases} \quad (5.49)$$

where: z_v Motion of the floating vessel.

r_d Wire drum radius.

θ_s Wire drum rotation angle.

The complete simulation is carried out by solving the above equations using numerical software such as MATLAB, Octave or Scilab. If the simulation is intended to be used in a real-time application, it should be implemented using a myRIO or a fast PLC.

An infinite fast control system is assumed to be controlling the wired drum in the simulation. This will of course result in a static load pressure p_L in the load circuit, since the payload stands more or less still. In real life, a more inaccurate controller in the simulation should be considered to create some varying load pressures. However, the given scenario is easy to implement in a PLC, since it does not need to be simulated real-time. The simulation could be performed before the test, and both the velocity and load pressure could be used as references in the load simulation circuits described in Chapter 5. The stochastic heave motion is illustrated in Figure 5.15.

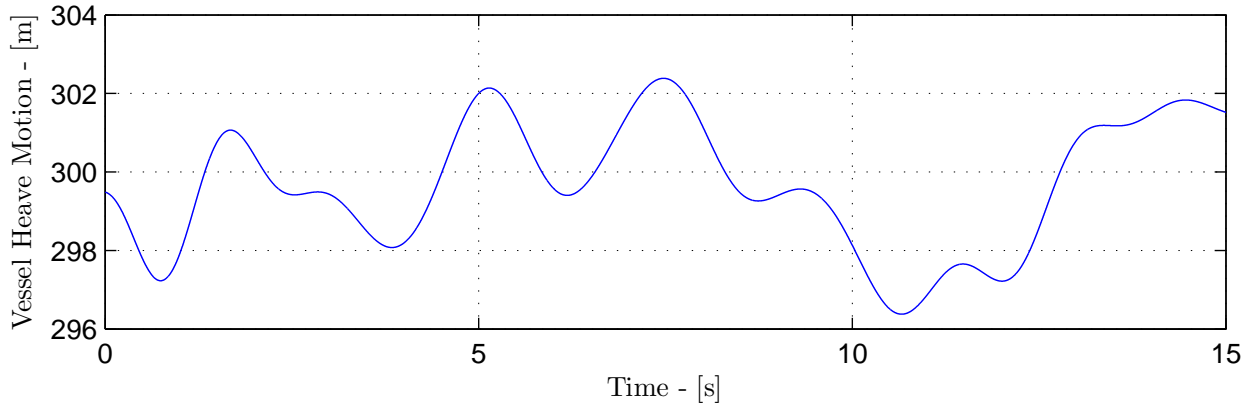


Figure 5.15: Heave motion of the vessel due to a stochastic wave.

from the stochastic wave motion it is possible to generate a velocity reference signal based on the heave motion and the wire drum radius. The velocity reference is described using Equation (5.50).

$$\omega_s^{(ref)} = -\frac{1}{r_d} \frac{dz_v}{dt} \quad (5.50)$$

The load pressure reference can be found by simulating the AHC using the stochastic wave input, or set to a static value if an infinite fast control system is considered in the AHC simulation. The load pressure reference, while assuming an infinite fast control system, is given by Equation (5.51).

$$p_L^{(ref)} = cst \quad (5.51)$$

An illustration of the supply and load pressure during 15 seconds of AHC simulation is given in Figure 5.16.

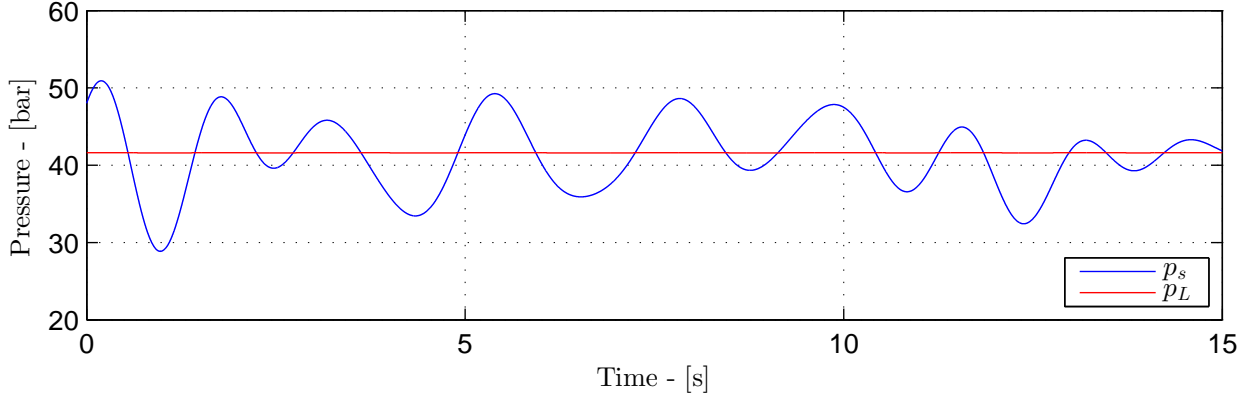


Figure 5.16: Pressure difference during ideal heave compensation.

This AHC simulation is used to generate reference speed and load pressure on the supply and load circuit respectively, and the results are measured and shown in the results in Section 6.3. This AHC simulation concludes the theory of the load circuit design and control. The next chapter is devoted to the results gathered using the methods and models in this chapter.

Results from Hydraulic Load Simulation Circuit

This chapter contain all experiments and results from the hydraulic load and supply circuit as detailed in Chapter 5 and also simulation results from using the SimulationX model of the two circuits as detailed in Section 5.6. At first the control parameters for the two circuits are identified in Section 6.1. The next step is to identify the parameters describing the friction, as shown in Section 6.2. Finally after using the control parameters and the friction model in a non-linear simulation model, it is verified by comparing to measurements in Section 6.3.

6.1 Controller Tuning

In Section 5.4 a control system for both the load and the supply circuits was presented. A PI-controller was chosen to control both hydraulic circuits, since such a controller gives zero steady state error for a step input, and a PI-controller is also robust in terms of rejecting noise in the control loop. MATLAB's tuning toolbox have been used to find suitable control parameters. Afterwards, the suggested control parameters were manually adjusted until the physical system behavior seemed stable. The representative control parameters describing the two control loops are given in Table 6.1.

Table 6.1: Transfer function parameters.

Load Circuit	MATLAB Tuned	Manually Tuned
K_P	$1.01 \cdot 10^{-9}$	$1.98 \cdot 10^{-9}$
T_i	0.023	0.03
Supply Circuit	MATLAB Tuned	Manually Tuned
K_P	$1.41 \cdot 10^{-7}$	$1.06 \cdot 10^{-7}$
T_i	0.000159	0.000159

In Table 6.1 the manually tuned and the MATLAB tuned control parameters are shown. Because of time limits, the controller gains had to be adjusted manually when testing the control system. However, the manually tuned parameters were chosen since the theoretical parameters introduced some instability in the control loops. Still the gains found using MATLAB indicates a very good control gain guess. This clearly states the benefit of using modeling techniques when designing control systems.

Two bode plots are used to illustrate the open and closed loop dynamics using the two different tuned controllers. The bode plots are shown in Figures 6.1 and 6.2 for the load circuit controller and supply circuit controller respectively.

6.1. CONTROLLER TUNING

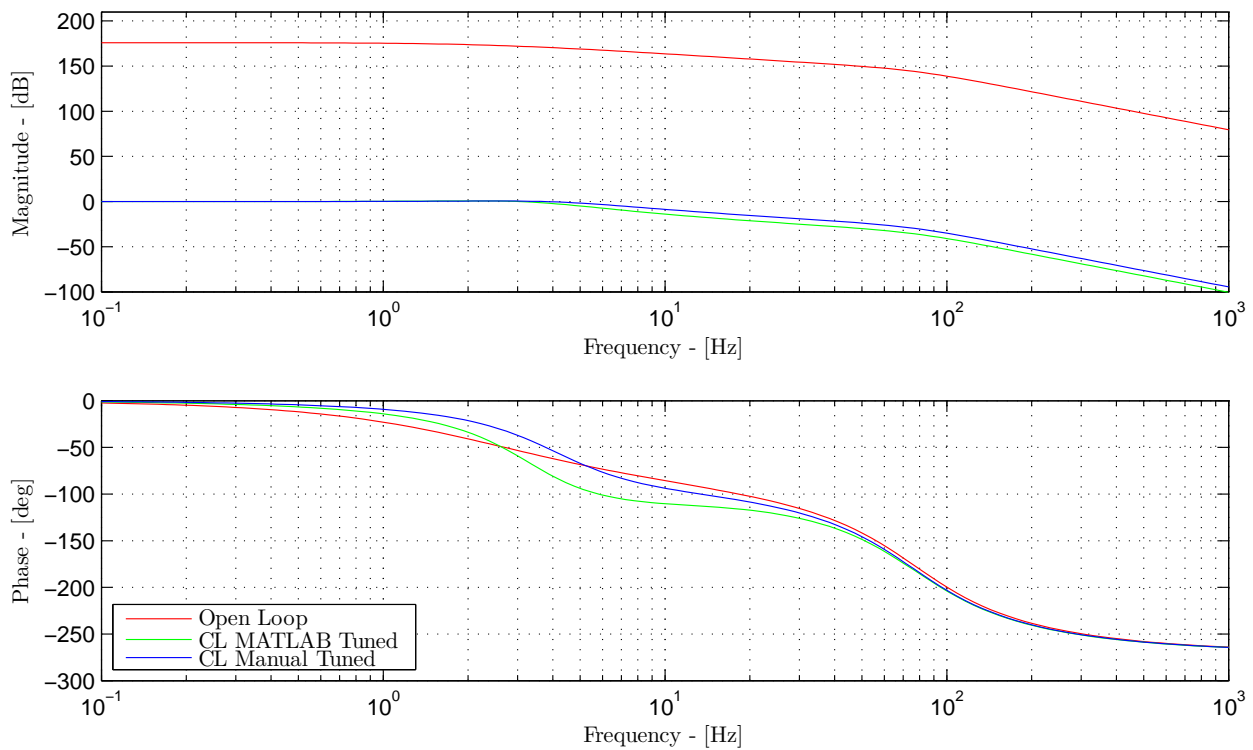


Figure 6.1: Bode plot illustrating load circuit tuning.

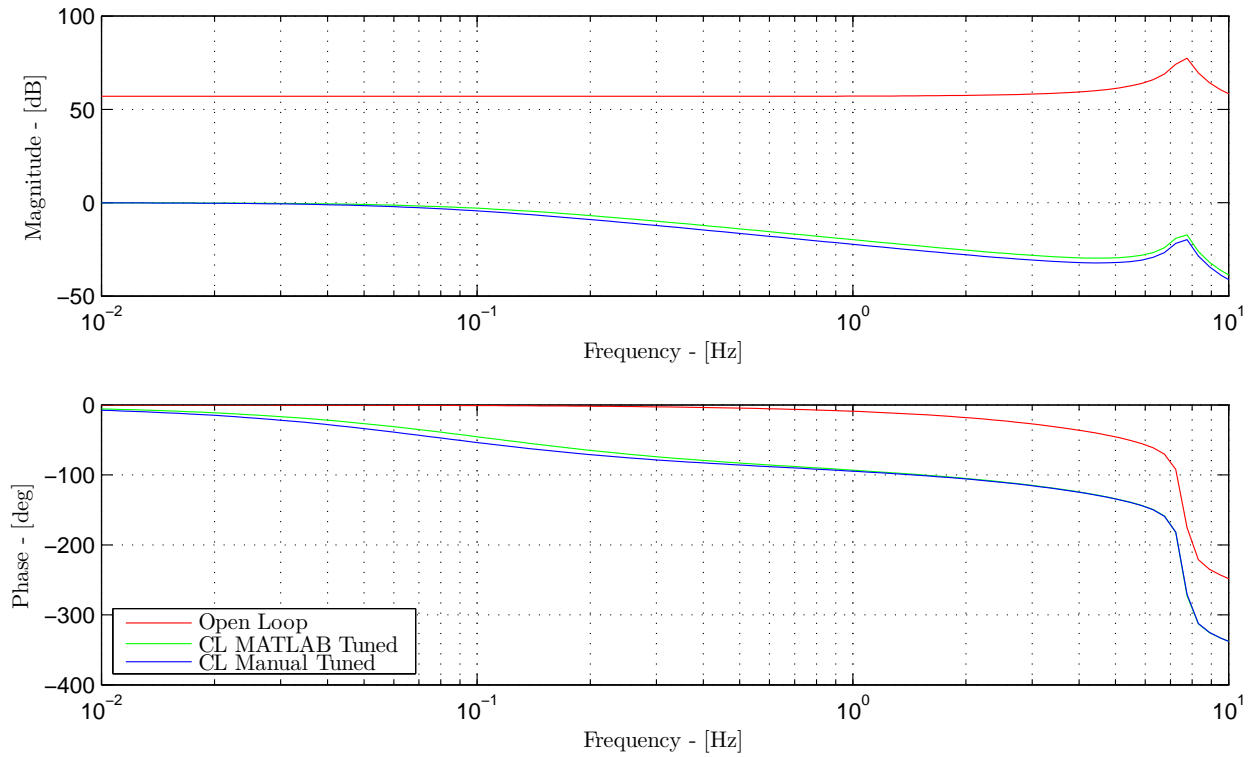


Figure 6.2: Bode plot illustrating supply circuit tuning.

The two bode plots also states that the manually tuned control parameters represents a much more

conservative control system than the one tuned using MATLAB's toolbox. Figure 6.2 clearly shows that the open loop dynamics of the supply circuit should give satisfying results, by only using an open loop P-controller, since the open loop gain is maintained constant up to about $30Hz$. However, a feedback controller is needed since an open loop controller would struggle to reject noise created by the load circuit.

When testing the control systems in a real life system and a simulation, it is obvious that the load circuit is heavily disturbed by the flow generated in the load circuit due to the shaft rotation, which again is controlled by the supply circuits velocity controller. This deviation could probably be reduced if a flow sensor was placed in the load circuit's hydraulic loop. Then a cascade controller could be used on the load side to ensure that the servo valve always supplies enough flow to obtain a constant load pressure p_L given any rotational velocity of the connecting shaft. Another idea is to ensure constant pressure difference across the servo valve at all times. This would physically linearize the servo valve and a robust feed forward control system could be introduced to remove the noise generated by the rotating shaft. This solution would probably give the best results, since feed-forward signals tends to increase the control bandwidth drastically.

Now that the control parameters are identified, the two hydraulic circuits may be controlled. In the next section the parameters describing the friction is identified.

6.2 Identification of Friction Model Parameters

As mentioned in Section 5.5 where the friction in the motor was defined, the constant parameters are unknown and must be identified by using measured data. The test bench described in Section 5.1 is used to gather the data necessary to identify the friction parameters. The experimental test was performed by manually manipulating the supply flow using the A4VSG pump. The rotational velocity, supply pressure and load pressure have been logged at all times. The friction torque was calculated using Equation (5.41) together with the zero-phase filtered experimental data. The experimental measurements (blue) is plotted together with the optimized friction model (red) in Figure 6.3.

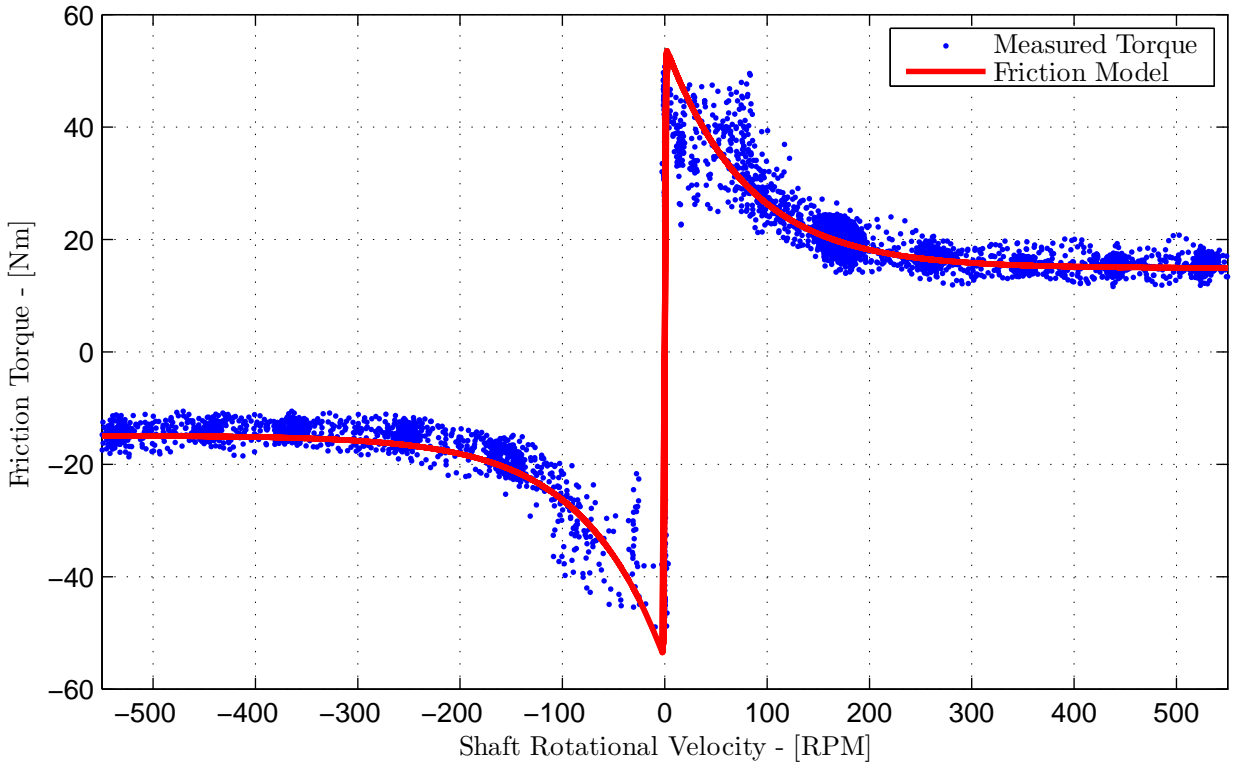


Figure 6.3: Comparison between the measured and the modeled friction.

The friction model illustrated with the red line in Figure 6.3 is obtained using the non-linear optimization algorithm described in Section 2.6.1. This ensures that the model parameters are fitted in a sufficient way. The objective function used to find the set of unknown friction model parameters introduced in Equation (5.38) are designed to minimize the squared error between the measured friction torque and the friction model torque. The minimization problem using the squared error is given by Equation (6.1).

$$\arg \min_{\vec{\Phi}_f} [\vec{\tau}_f(\vec{\Phi}_f, \omega_s) - \vec{T}_f(\dot{\omega}_s)]^T [\vec{\tau}_f(\vec{\Phi}_f, \omega_s) - \vec{T}_f(\dot{\omega}_s)] \quad (6.1)$$

where: $\vec{\tau}_f(\vec{\Phi}_f, \omega_s)$ The calculated friction torque due to the friction model parameters $\vec{\Phi}_f$.
 $\vec{T}_f(\dot{\omega}_s)$ Experimental friction at a given rotational acceleration $\dot{\omega}_s$.
 $\vec{\Phi}_f$ Vector containing the unknown friction model parameters.

The optimized model parameters found by minimizing Equation (6.1) is representing the model shown by red in Figure 6.3, and the model parameters are given in Table 6.2.

Table 6.2: Optimized friction model parameters.

Parameter	Value	Unit
r	13.8806	[\cdot]
ω_0	8.3593	[rad/s]
τ_c	14.8939	[Nm]
τ_s	54.8258	[Nm]

The optimized friction model parameters are used together with the friction model described in Section 5.5 to describe the friction torque in the SimulationX model. The friction model have been tested during a small scale AHC simulation, and the results are presented in Section 6.3.

6.3 Verification of SimulationX Model

The objective and motivation to build and design the load circuit is to reproduce an active heave compensation situation offshore. To find suitable reference signals for the load controller controlling the load pressure p_L and the supply circuit controller controlling the shaft rotational velocity, ω_s , the small scale AHC simulation model described in Section 5.7 have been used.

The AHC simulation should control the payload to remain a given height above the sea floor, even though the floating vessel experiences a heave motion due to a stochastic wave motion. The drum controlling the wire length at all times is actuated using the closed loop A4VSG pump inside the simulation. To test the real life test bench, the same control reference is used to control the rotational velocity of the shaft connection the supply motor and the load motor. At the same time, a static load pressure p_L have been applied to the load side, generating a constant torque T_L disturbing the supply circuit at all times during AHC.

The same scenario and reference inputs have been used in the SimulationX model which uses the same control parameters found in Section 6.1 and the friction model found in Section 6.2. A comparison between simulated and measured rotational velocity and load pressure is shown in Figures 6.4 and 6.5 respectively.

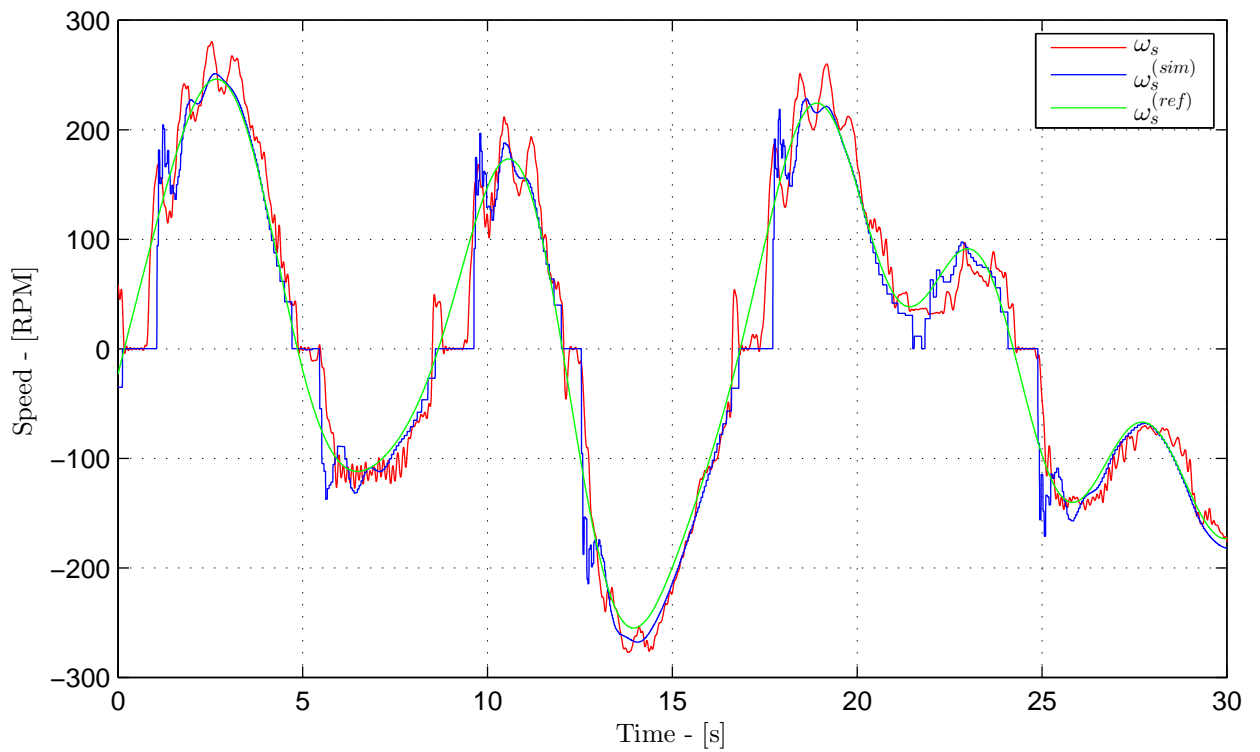


Figure 6.4: Comparison of measured and simulated rotational shaft velocity, when a stochastic velocity reference signal is applied to simulate a small scale AHC.

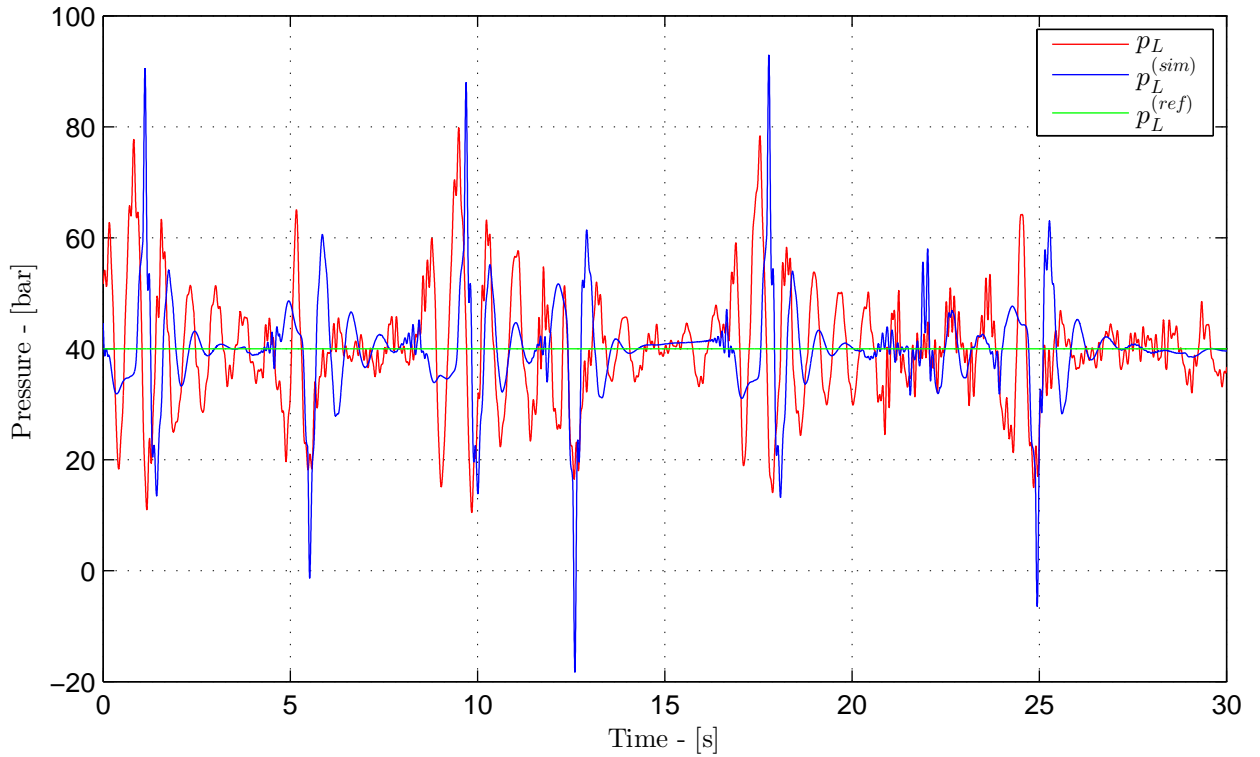


Figure 6.5: Comparison of measured and simulated load pressure, when a static pressure reference signal is applied during AHC.

From Figures 6.4 and 6.5 it is clear that the similarities between measurements and simulations in terms of both rotational shaft velocity and load pressure are not perfectly equal. However, the two result are not completely different, and should be a good approximation if the load circuit simulation is used to further test and modify the hydraulic loops or the control system. Especially the stiction friction which prevent the shaft from rotating when passing trough zero velocity is maintained in quite a satisfying way. This can be seen of the curves in Figure 6.4 where the rotational velocity is close to zero. This states that the friction model described in Section 5.5 is close to real, and it could be used to further improve the control system in the future through simulations.

Also the supply pressure is measured and simulated. Therefore it would be interesting to compare them as well to check the SimulationX model for errors. The compared supply pressures are illustrated in Figure 6.6.

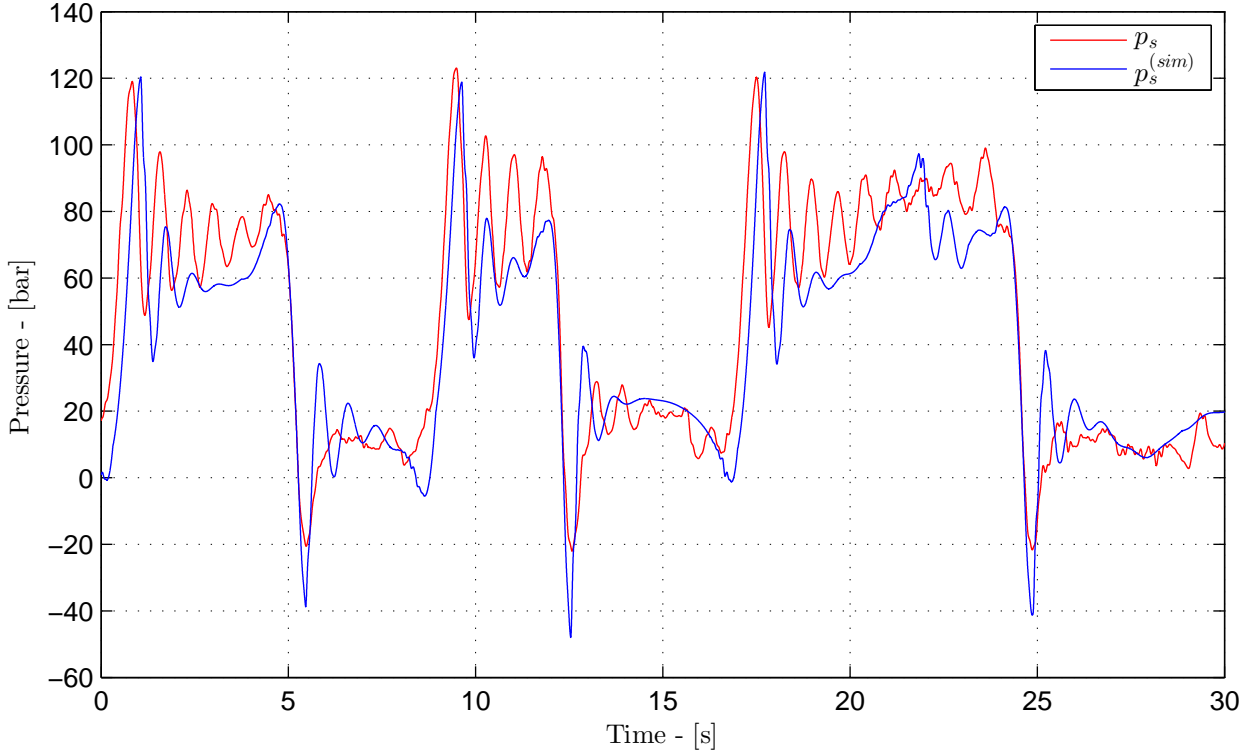


Figure 6.6: Comparison of measured and simulated supply pressure during AHC.

Figure 6.6 also indicates some deviations between real-life experiments and the simulation results. Anyhow, by examining the results, it is clear that the main trend in both the simulated and measured supply pressure signal are quite similar. The simulation model is therefore seen as a quite good representation of the real-life test bench behavior. However, if more time had been available, a more accurate simulation model should be identified by examining the model in more detail.

6.4 Simulated Step Test Verification of Control Parameters

The results in this section is based on the SimulationX model of the load circuit and supply circuit as described in Section 5.6. Using this model, a step test on the speed and load pressure reference were performed one at a time. For the speed step test, a comparison of the reference speed and measured speed is shown in Figure 6.7

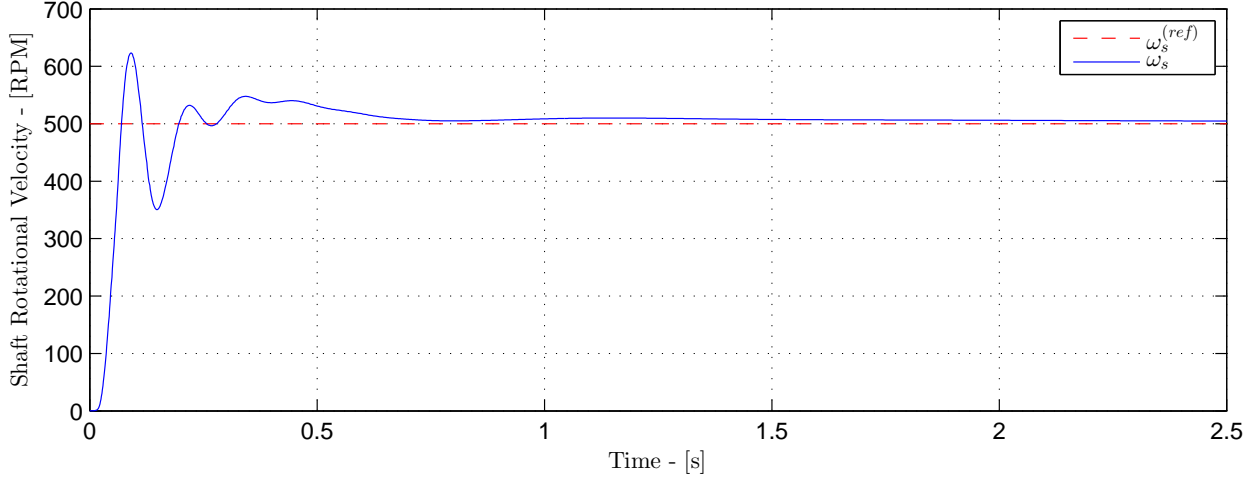


Figure 6.7: Load pressure reference step on simulation model.

As shown in Figure 6.7, the speed controller manages to get zero steady state error on the speed step test. For the load pressure step test, the comparison between input and response is shown in Figure 6.8.

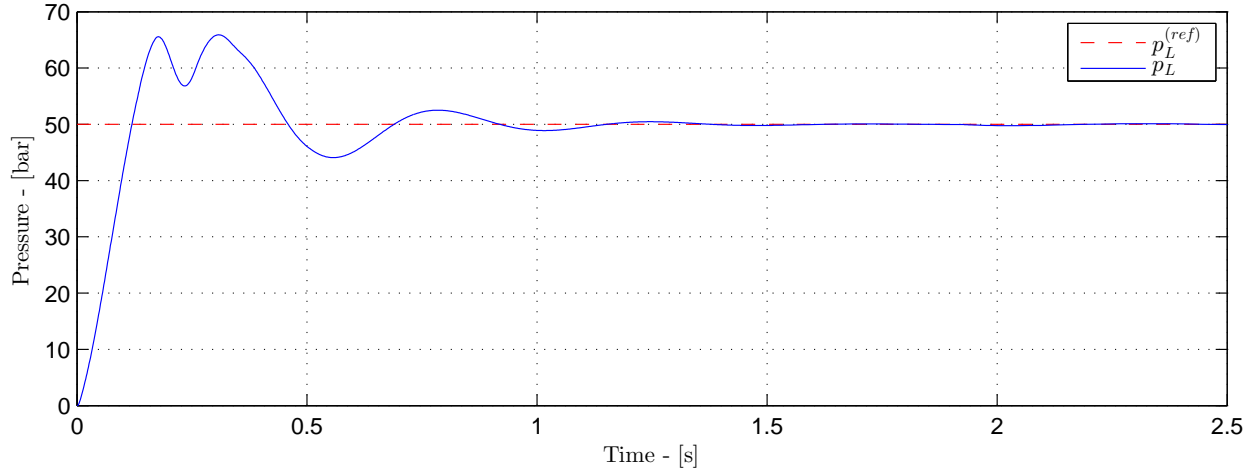


Figure 6.8: Speed reference step on simulation model.

Also in Figure 6.8 the load pressure controller removes any steady state error from the step input. These step tests were not conducted on the physical system because of lack of safety valves due to a misdelivery from Parker. From these tests it is shown that the controllers removes any steady state error, and are therefore verified. However overshoot, rise time and settling time could be better with a more sophisticated control system and/or tuning process.

Chapter **7**

Discussion and Conclusions

7.1 Hydraulic Pump Model

In this project a mathematical simulation model of a variable displacement piston pump named A4VSG manufactured by Bosch Rexroth have been presented. The simulation model includes the internal piston kinematics that describes the volume flow through the pump, and the dynamics of the hydraulic swash plate angle control circuit, hereby called the actuating circuit. The dynamics of the actuating circuit is described using either a Black box model or a Grey box model. The Black box model is represented with a linear transfer function from an input of a swash plate angle reference to the actual swash plate angle. Since the actuating circuit is non-linear, several Black box models have been identified around different linearization points in terms of swash plate angle offsets and amplitudes. In order to identify the frequency response of the actuating circuit, a frequency response test and analysis was conducted on the swash plate angle control circuit. To identify the linear Black box model of the frequency response, MATLAB's System Identification Toolbox have been used to fit a fifth order transfer function to the frequency response data. Such a linear Black box model is useful for designing a linear control system, however it falls short to represent the true dynamics since the actuating circuit is non-linear.

To overcome this problem, a non-linear Grey box model of the actuating circuit is presented. This model includes the internal valve control system and a hydraulic model of the actuating circuit. The unknown parameters for this model are identified using a gradient based numerical optimization algorithm that minimizes the deviation between measured and simulated responses in the time and frequency domain. Two sets of unknown parameters are identified in total; one set where all parameters are optimizeable (hereby called the Free Grey box model), and one set where two hard parameters of the cylinder are locked based on a data sheet of the actuating circuit (hereby called the Locked Grey box model).

In order to determine the accuracy of the models, predefined criteria for maximum and mean deviation between simulated and measured response is used. In the frequency domain, the free Grey box model and the Black box models passes the criteria, however the locked Grey box model does not pass the criteria on any point. The same issue is revealed in the time domain where the locked Grey box model does not manage to keep the simulated internal valve position close to the measured one. Because of this, the free Grey box model is concluded to be the best non-linear model of the swash plate angle control circuit.

The movement of the pistons attached to the swash plate is also described using three dimensional kinematic equations. This allows for simulations of the high frequent, low magnitude ripple flow that is included on top of a mean volume flow. Because of the numerical complexity of simulating the piston movements, an empirical simplification of the ripple flow was presented. It was shown however that the ripple flow is unnecessary to simulate if the pump is connected to a hose as the damping will cancel out the ripple strokes.

With the basis of the free Grey box model and the simplified ripple flow, a complete SimulationX model of the A4VSG pump have been created. This model is compounded into a single SimulationX block that can be used in any simulation model. To create this model, the governing equations for the system were used instead of the standard hydraulic block library to keep the model completely similar to the optimized model.

7.2 Hydraulic Load Simulation Circuit

The second part of this project focuses on the design and control of a hydraulic load simulation circuit. The load circuit is a hydraulic circuit including an supply pump, a servo valve and a motor. The shaft of this motor is mechanically connected to a second motor whose hydraulic ports are connected to a closed loop circuit with the A4VSG pump. This hydraulic closed loop circuit is hereby called the supply circuit. The servo valve in the load circuit is controlled to keep a reference load pressure across the motor, and the swash plate angle on the A4VSG pump is controlled to keep a reference speed on the shaft.

In order to design a linear control system for the two hydraulic circuits, mathematical models of the two circuits were presented and linearized. The linearized models created the basis for designing PI-controllers for the two circuits using MATLAB's controller tuning toolbox. A PI-controller was chosen to remove all steady state error from a step input. MATLAB was used to tune the controllers theoretically based on the linearized models, however the suggested controller values introduced some instability on the physical system. Therefore the controller gains were reduced manually with the suggested values from MATLAB as initial guess to remove the instability. Both control systems were verified through a simulation where a step input was applied, where both controllers removed all steady-state error.

To illustrate the purpose of the load circuit, an Active Heave Compensation (AHC) simulation was presented. This simulation consists of a closed loop pump in loop with a motor whose mechanical shaft is connected to a wire drum. The aim is to compensate for heave motion of the offshore boat by lowering and hoisting wire. The load circuit's job is to reproduce the load subjected on the drum during the AHC simulation in order to recreate the simulated load physically. From tests using this simulation, the speed controller on the supply circuit managed to reproduce the reference speed quite closely, however the performance of the load controller was not as good. This is due to the non-linear nature of the servo valve. Therefore a non-linear control system could be implemented instead.

From the non-linear model of the two hydraulic circuits, a SimulationX model of the setup was created. This model includes a LuGre inspired friction model whose parameters were identified using a gradient based numerical optimization algorithm. From comparisons between this model and measured test data, it was shown that they are quite similar in terms of controller performance and load pressures. The model consists of standard hydraulic library blocks to include the true behavior on hoses, bulk pressure and oil density.

Bibliography

- [1] National Instruments. Picture of myRIO - <http://sine.ni.com/psp/app/doc/p/id/psp-1166/lang/no>. 10.05.2015.
- [2] Bosch Rexroth. Picture of Pumpcard - <http://www.directindustry.com/prod/bosch-rexroth-industrial-hydraulics/proportional-flow-regulators-numerical-control-9143-1270927.html>. 10.05.2015.
- [3] Siemens. PLC Picture - <http://w3.siemens.com/mcms/programmable-logic-controller/en/distributed-controller/et200sp-based/Pages/default.aspx>. 10.05.2015.
- [4] S. S. Tørdal and A. Klausen. Dynamiske karakteristikker av Brevini HPV41 med åpen og lukket sløyferegulering. Bachelor's thesis., 2013.
- [5] Bosch Rexroth Group. *Axial Piston Variable Pump A4VSG*, RE 92100/05.11.
- [6] Bosch Rexroth Group. *Control Systems HM, HS, HS4 and EO*, RE 92076/08.10.
- [7] Bosch Rexroth Group. *VT-VPSCD, Digital closed-loop control electronics for axial piston pumps A4VS... with HS4 control and A2V... with EO4 control*, RE 30028-B/09.13.
- [8] Parker. *Hydraulic Motors, Series V12, V14, T12, Variable Displacement*, HY30-8223/UK.
- [9] Parker Servo Valve, Series D3FD Catalogue HY11-3500/UK.
- [10] Noah Manring. *Hydraulic control systems*. Wiley, 2005.
- [11] Jian Qiu Zhang, Zhao Xinmin, Hu Xiao, and Sun Jinwei. Sinewave fit algorithm based on total least-squares method with application to ADC effective bits measurement. *Instrumentation and Measurement, IEEE Transactions on*, 46(4):1026–1030, 1997.
- [12] Theagenis J Abatzoglou, Jerry M Mendel, and Gail A Harada. The constrained total least squares technique and its applications to harmonic superresolution. *Signal Processing, IEEE Transactions on*, 39(5):1070–1087, 1991.
- [13] Richard H Byrd, Jean Charles Gilbert, and Jorge Nocedal. A trust region method based on interior point techniques for nonlinear programming. *Mathematical Programming*, 89(1):149–185, 2000.
- [14] Richard A Waltz, José Luis Morales, Jorge Nocedal, and Dominique Orban. An interior algorithm for nonlinear optimization that combines line search and trust region steps. *Mathematical Programming*, 107(3):391–408, 2006.

- [15] Richard H Byrd, Mary E Hribar, and Jorge Nocedal. An interior point algorithm for large-scale nonlinear programming. *SIAM Journal on Optimization*, 9(4):877–900, 1999.
- [16] Bosch Rexroth Group. *4/2 and 4/3 proportional directional valves direct operated, with electrical position feedback, Types 4WRE and 4WREE, RE 29 061/02.03*.
- [17] Roland Burns. *Advanced control engineering*. Butterworth-Heinemann, 2001.
- [18] Michael Rygaard Hansen and Torben Ole Andersen. *Hydraulic Components and Systems*. University of Agder and Aalborg University, 2012.
- [19] Garrett A Sohl and James E Bobrow. Experiments and simulations on the nonlinear control of a hydraulic servosystem. *Control Systems Technology, IEEE Transactions on*, 7(2):238–247, 1999.
- [20] K Johanastrom and Carlos Canudas-De-Wit. Revisiting the lugre friction model. *Control Systems, IEEE*, 28(6):101–114, 2008.
- [21] Carl M. Larsen. *Ocean currents, Linear Wave Theory, Wave Induced Forces and Motions*. NTNU, Department of Marine Technology, 2012.
- [22] Willard J Pierson and Lionel Moskowitz. A proposed spectral form for fully developed wind seas based on the similarity theory of SA Kitaigorodskii. *Journal of geophysical research*, 69(24):5181–5190, 1964.
- [23] H. Garnier, M. Mensler, and A. Richard. Continuous-time Model Identification From Sampled Data: Implementation Issues and Performance Evaluation. *International Journal of Control*, 76(13):1337–1357, 2003.
- [24] L. Ljung. Experiments With Identification of Continuous-Time Models. *IFAC Symposium on System Identification*, 15, 2009.
- [25] P. C. Young and A. J. Jakeman. Refined instrumental variable methods of time-series analysis: Part III, extensions. *International Journal of Control*, 31:741–764, 1980.
- [26] Bosch Rexroth Group. *Spare Part List, A4VSG 71HS4KP/10R-PPB10K680N*, 01 2015.
- [27] Pepperl+Fuchs. *Inductive Sensor NEB6-12GM50-E2-V1 - Data sheet*, 2013.
- [28] HYDAC. Flow Sensor, EVS 3100-H.
- [29] National Instruments. MyRIO general documentation.

Appendices

A Stochastic Wave Generation

In order to test a system response with a stochastic wave input, a Pierson-Moskowitz [22] wave spectrum is used to generate a stochastic wave. This wave spectra simulates a typical sea state with a given significant wave weight and wave period. The spectrum is obtained by Equation (1).

$$S_x(\omega_{st}) = 5\pi^4 \cdot \frac{H_s^2}{T_p^4} \cdot \frac{1}{\omega_{st}^5} \cdot \exp\left[-\frac{20\pi^4}{T_p^4} \cdot \frac{1}{\omega_{st}^4}\right] \quad (1)$$

where: S_x Stochastic wave spectrum.

ω_{st} Frequency of a stochastic wave part.

H_s Significant wave height.

T_p Significant wave period.

By using Equation (1), the wave spectrum is plotted for a given sea state. Figure 1 shows an example of a Pierson-Moskowitz spectrum with $H_s = 10m$ and $T_p = 2s$.

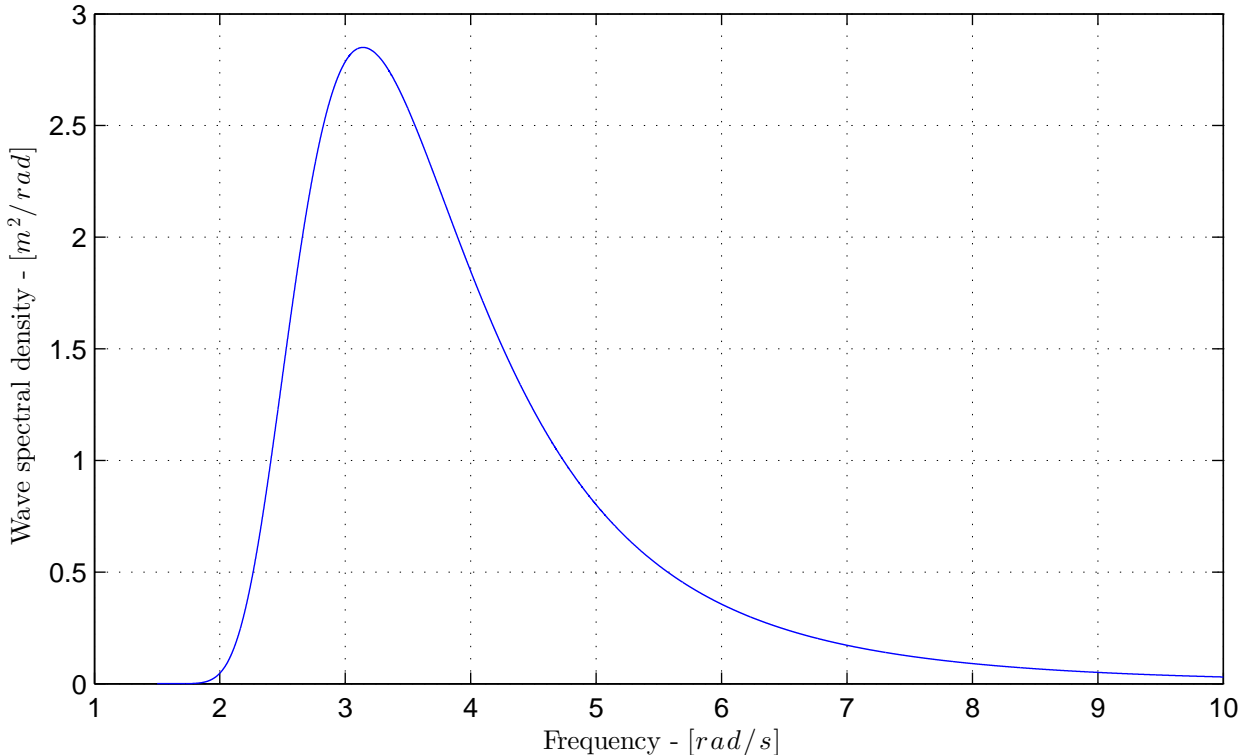


Figure 1: Example of a Pierson-Moskowitz spectrum.

A stochastic wave is generated from this spectrum using a summation of several sine components. The sine components are identified by dividing the spectrum into appropriate intervals. For instance the wave spectrum may be divided into $N = 20$ intervals. This evenly spaced interval is shown in Figure 2

With this spaced spectrum, it is possible to calculate the amplitude of each sine wave signal. This amplitude is given by Equation (2).

$$C_n(\omega_{s,n}) = \sqrt{2 \cdot S_x(\omega_{s,n}) \cdot \Delta\omega_s} \quad (2)$$

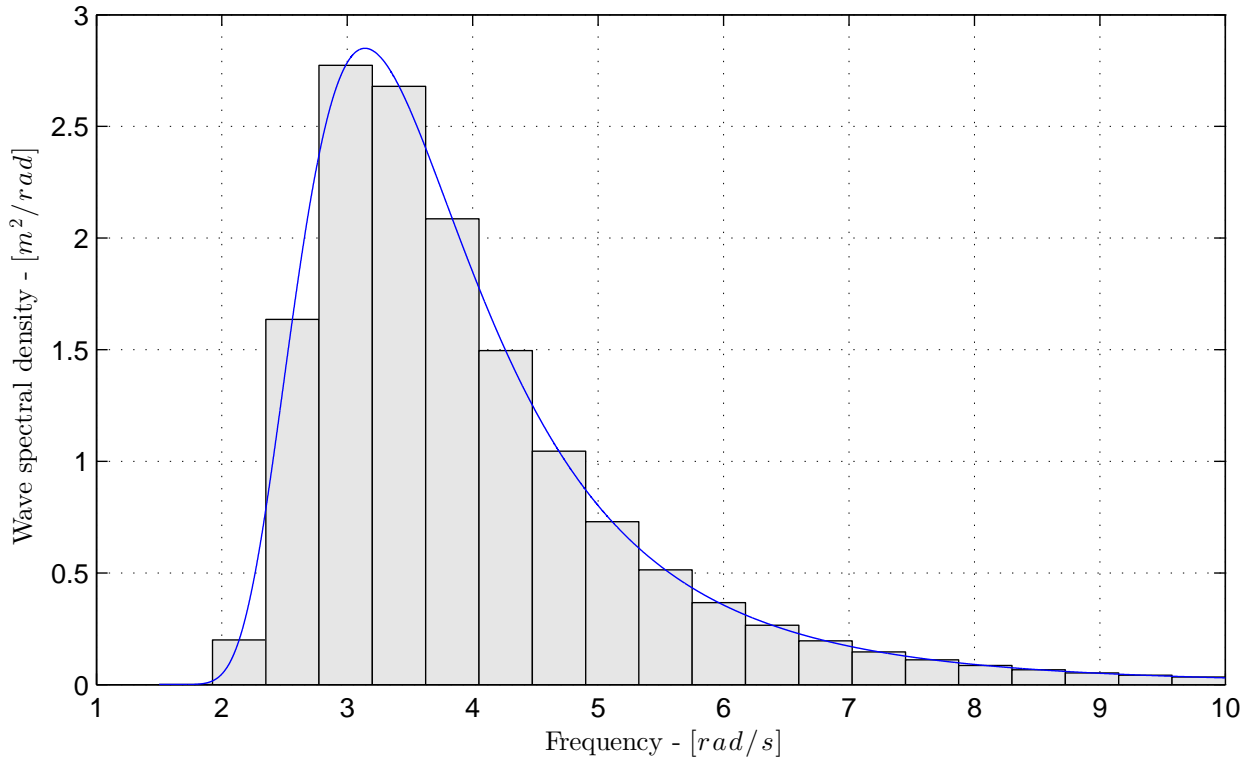


Figure 2: Evenly spaced wave spectrum.

where: C_n Amplitude of sine wave n .

$\omega_{s,n}$ Frequency of sine wave n .

$\Delta\omega_s$ Frequency between $\omega_{s,n+1}$ and $\omega_{s,n}$.

When each wave amplitude is calculated, the different wave components can be calculated in the time domain. The waves are given by:

$$x_n(t) = C_n(\omega_{n,s}) \cdot \sin(\omega_{n,s} \cdot t + \epsilon) \quad (3)$$

where: $x_n(t)$ Wave component n .

ϵ Random number $\in [0, 2\pi]$.

After all wave components are calculated, a summation is used to make the complete stochastic wave, as shown in Equation (4).

$$x(t) = \sum_{n=1}^N x_n(t) \quad (4)$$

where: N Number of wave components the spectrum is divided into.

The final stochastic wave $x(t)$ can be used in a time simulation by evaluating Equation (4) at every time step. A stochastic wave generated from the spectrum shown in Figure 2 is shown in Figure 3.

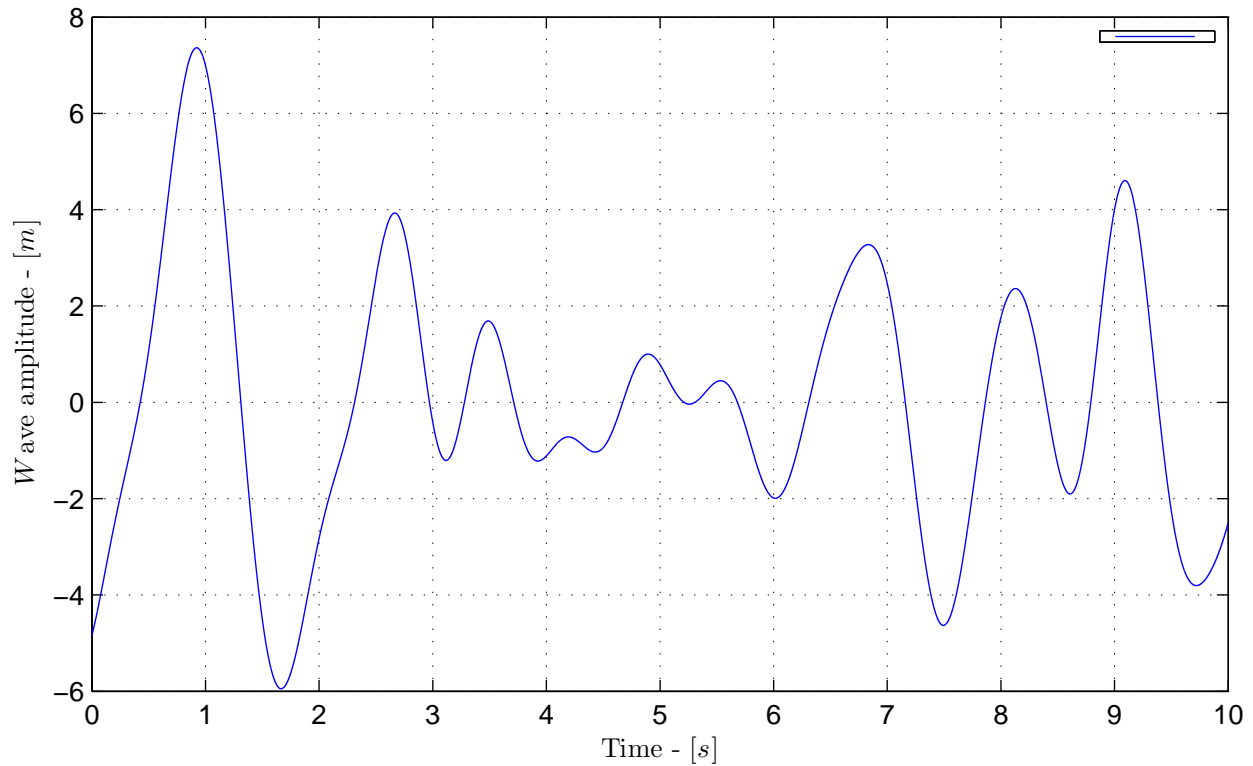


Figure 3: Stochastic wave.

B Transfer Function Estimation

The system identification is performed using MATLAB's System Identification Toolbox [23, 24, 25]. The toolbox presents a useful graphical user interface (GUI) which is used to import the frequency domain data from the lab test results presented in Section 2.3. The toolbox is used to estimate time continuous transfer functions from bode frequency response data, which should characterize the dynamics between the reference swash plate angle and the measured swash plate angle. An overview of the system identification toolbox is shown in Figure 4.

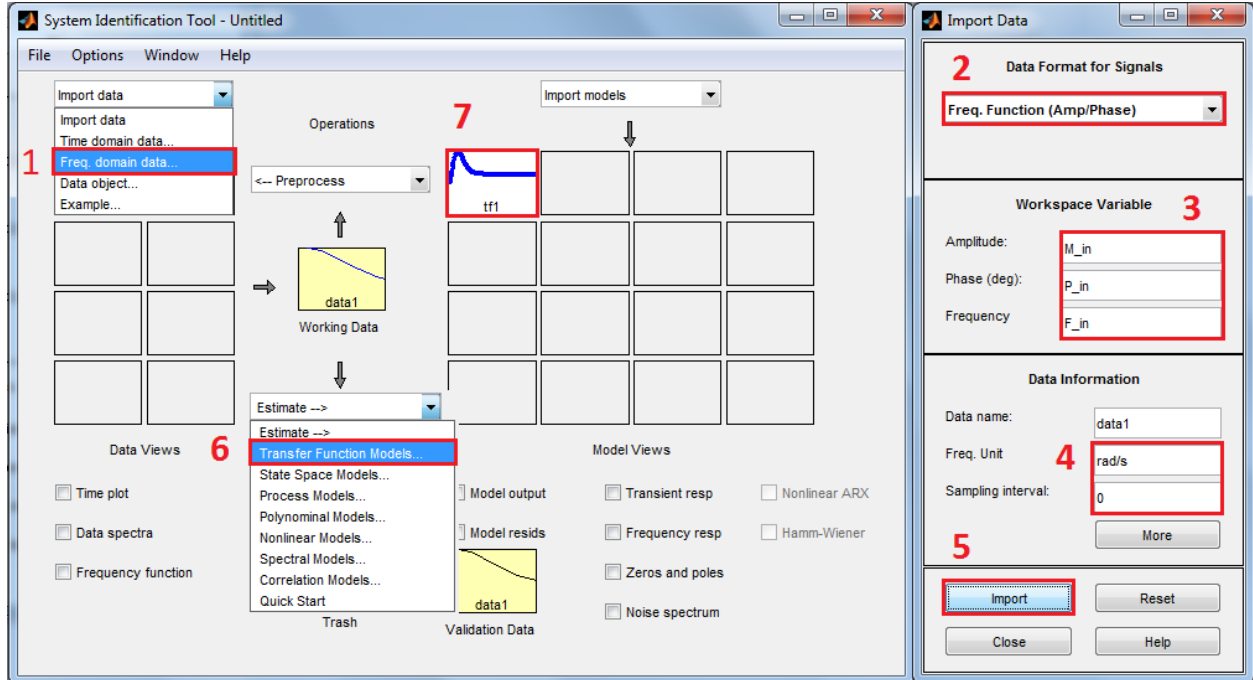


Figure 4: System identification toolbox layout [4].

Figure 4 shows seven steps which are necessary to produce an estimated transfer function using the experimental test results. The seven steps are:

1. The data type is set to be frequency domain data.
2. The data format of the experimental data is given as three vectors containing the magnitude M , phase ϕ and the frequency in rad/s.
3. Here the reference to the three vectors stored in MATLAB's workspace is specified.
4. The sampling time is set 0 to get a time continuous transfer function, since the sampling of the experimental data is much faster than the systems bandwidth, and should therefore give satisfactory results.
5. Press this button to import the experimental frequency domain data.
6. Choose "Transfer Function Models" from the drop down menu, then specify number of poles and zeros in your estimated transfer function.
7. The information about the approximated transfer function is found here.

C Bode Plot Comparisons

In this appendix the Black box models from Section 4.2.1 and the Free and Locked Grey box models from Section 4.4.1 are compared to a measured frequency response in order to assess their accuracy side by side. Bode plots from all amplitudes, $A \in [5, 10, 20]\%$, and all offsets, $O \in \pm[25, 50, 75]\%$ are presented here. The x-axis on all bode plots in this appendix is the frequency in Hz and the test amplitude and offset is displayed in the title of the magnitude plot. Two subplots are together, i.e. a magnitude and phase plot is displayed together under the same title. The legend is only shown on the phase plot because of space limitations.

In all the bode plots, the black dots shows the magnitude or phase of the measured frequency response at the given test sine amplitude and offset. The blue line shows the frequency response of the free parameter Grey box model, the green line shows the frequency response of the locked parameter Grey box model, and finally the red line shows the frequency response of the Black box model.

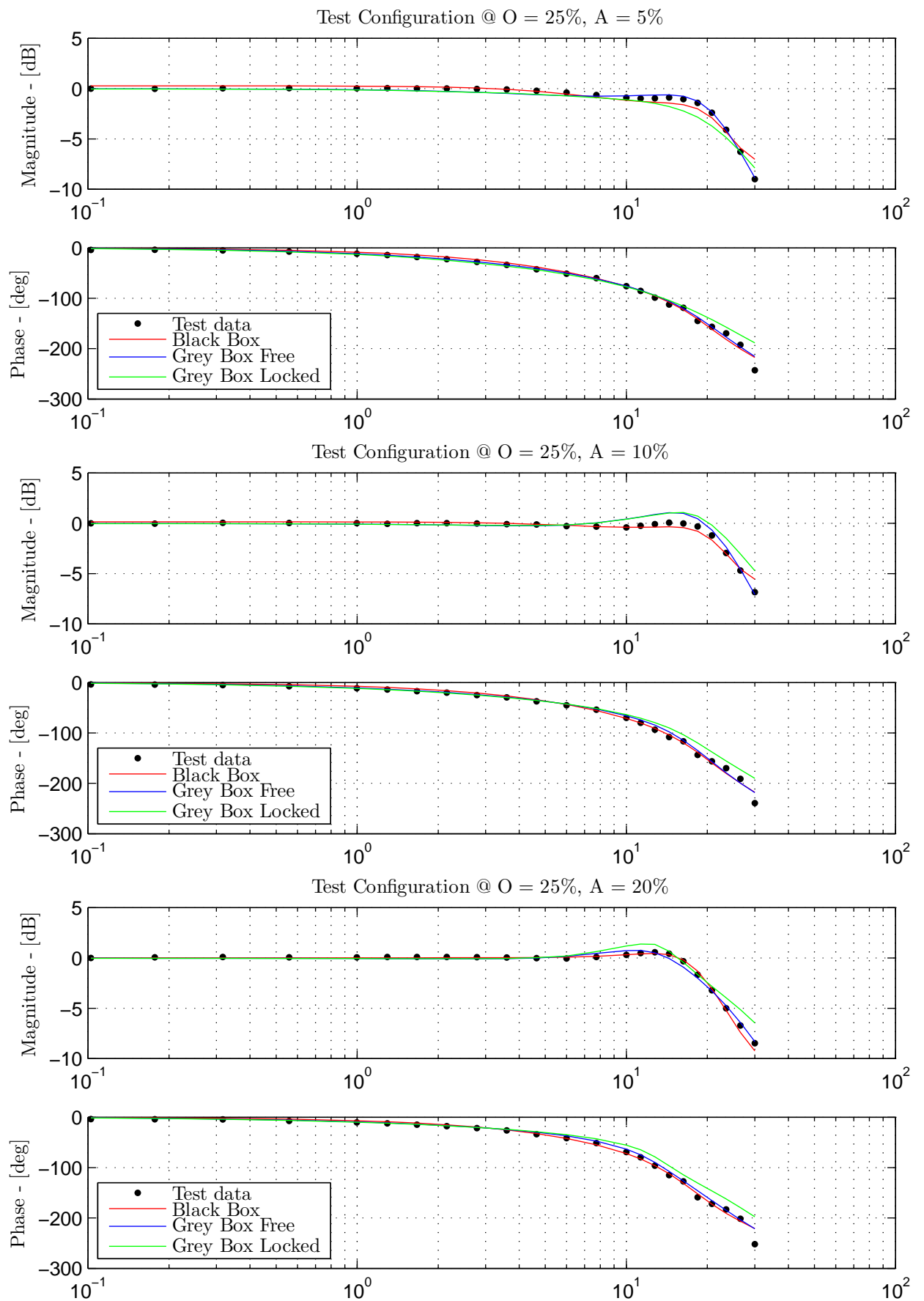
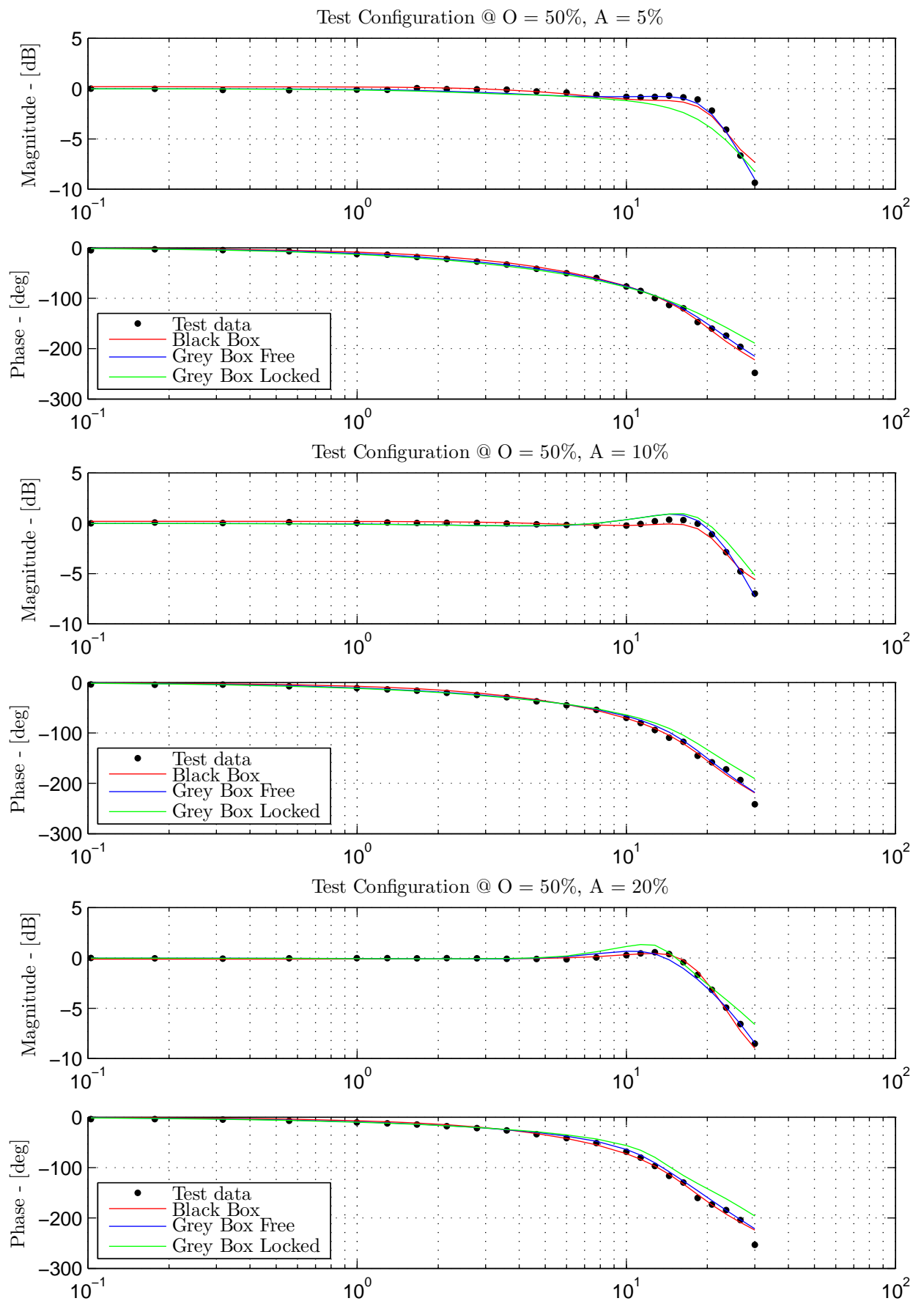
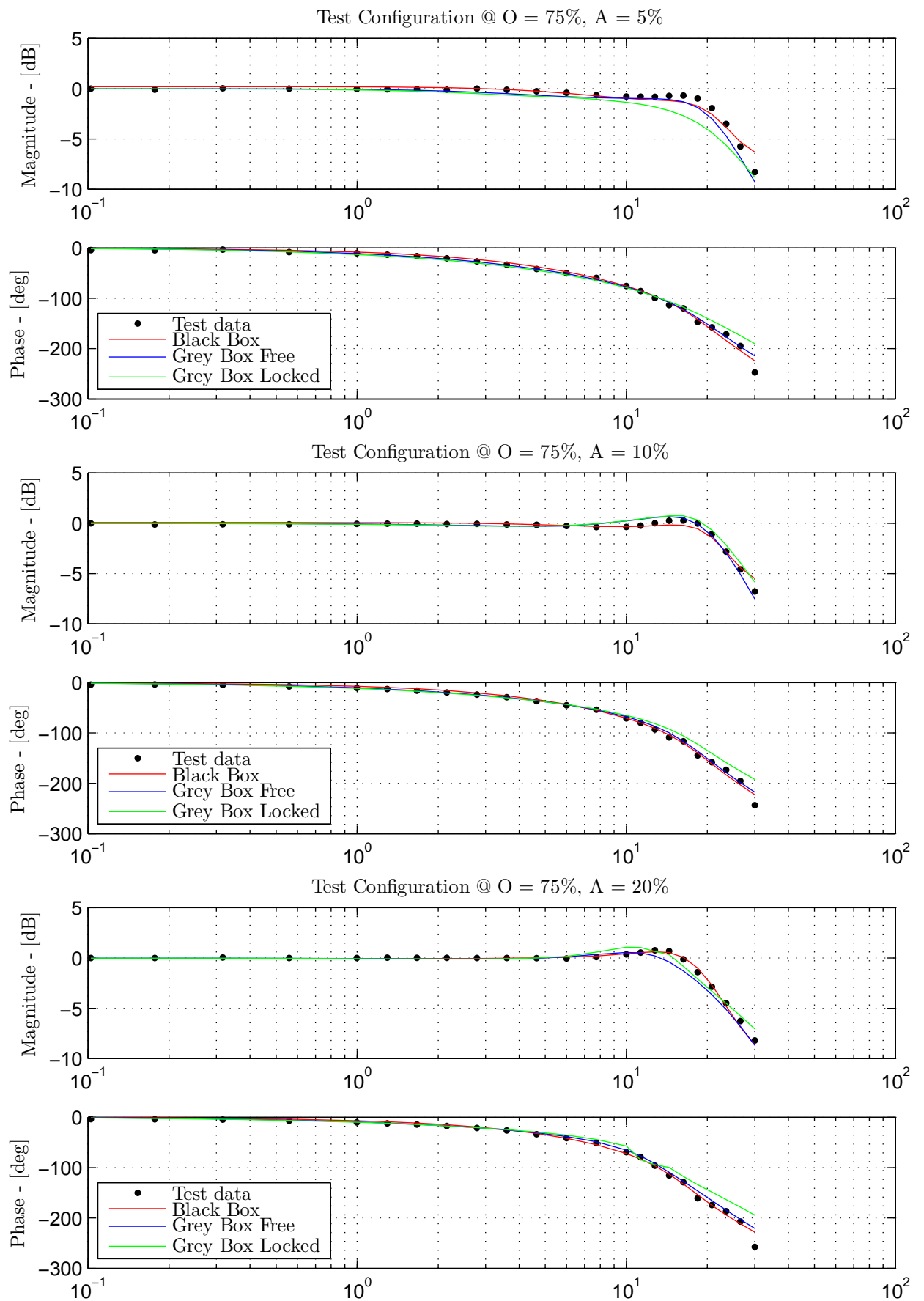
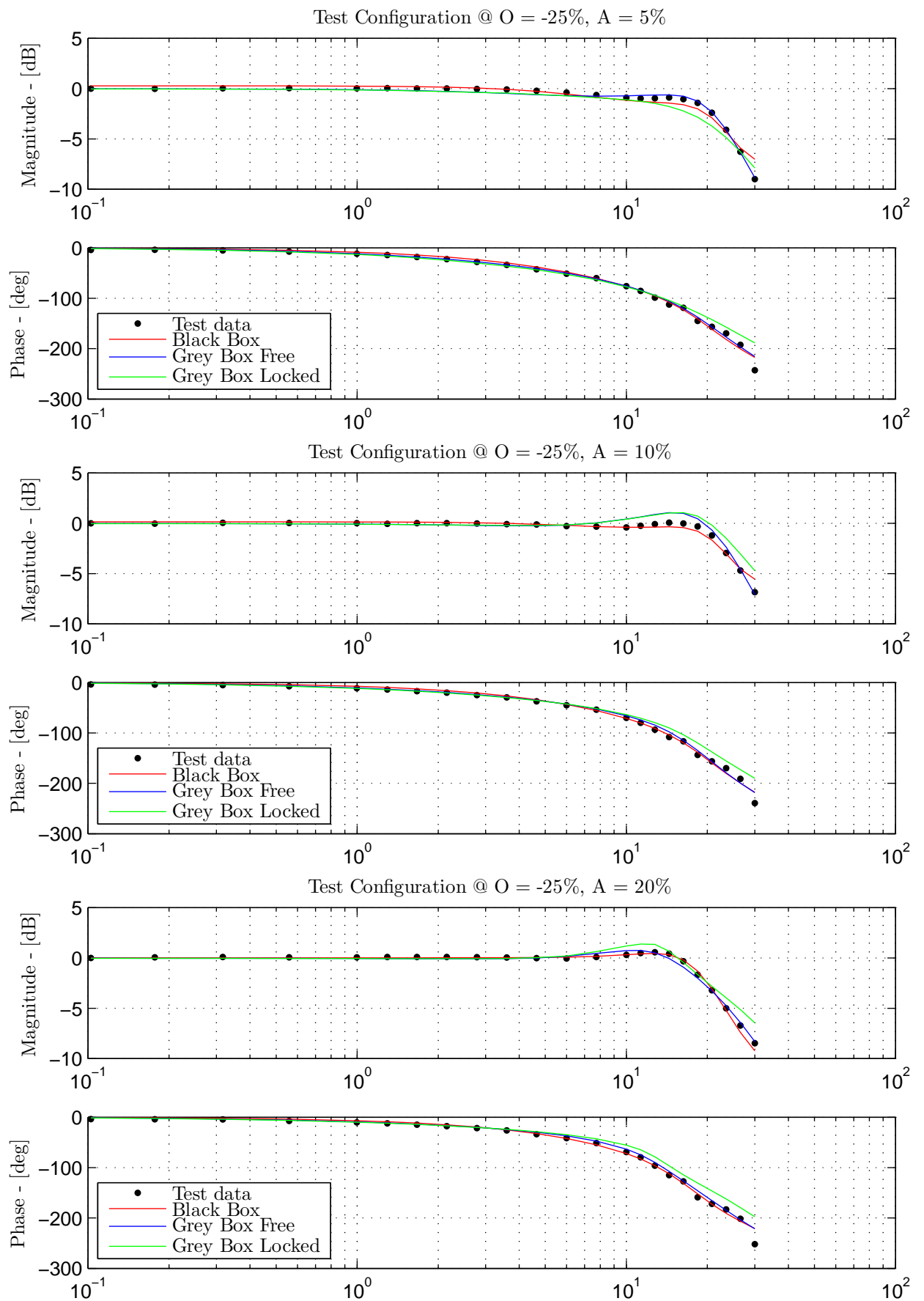


Figure 5: Test data compared with Black and Grey Box model @ O = 25%.

Figure 6: Test data compared with Black and Grey Box model @ $O = 50\%$.

Figure 7: Test data compared with Black and Grey Box model @ $O = 75\%$.

Figure 8: Test data compared with Black and Grey Box model @ $O = -25\%$.

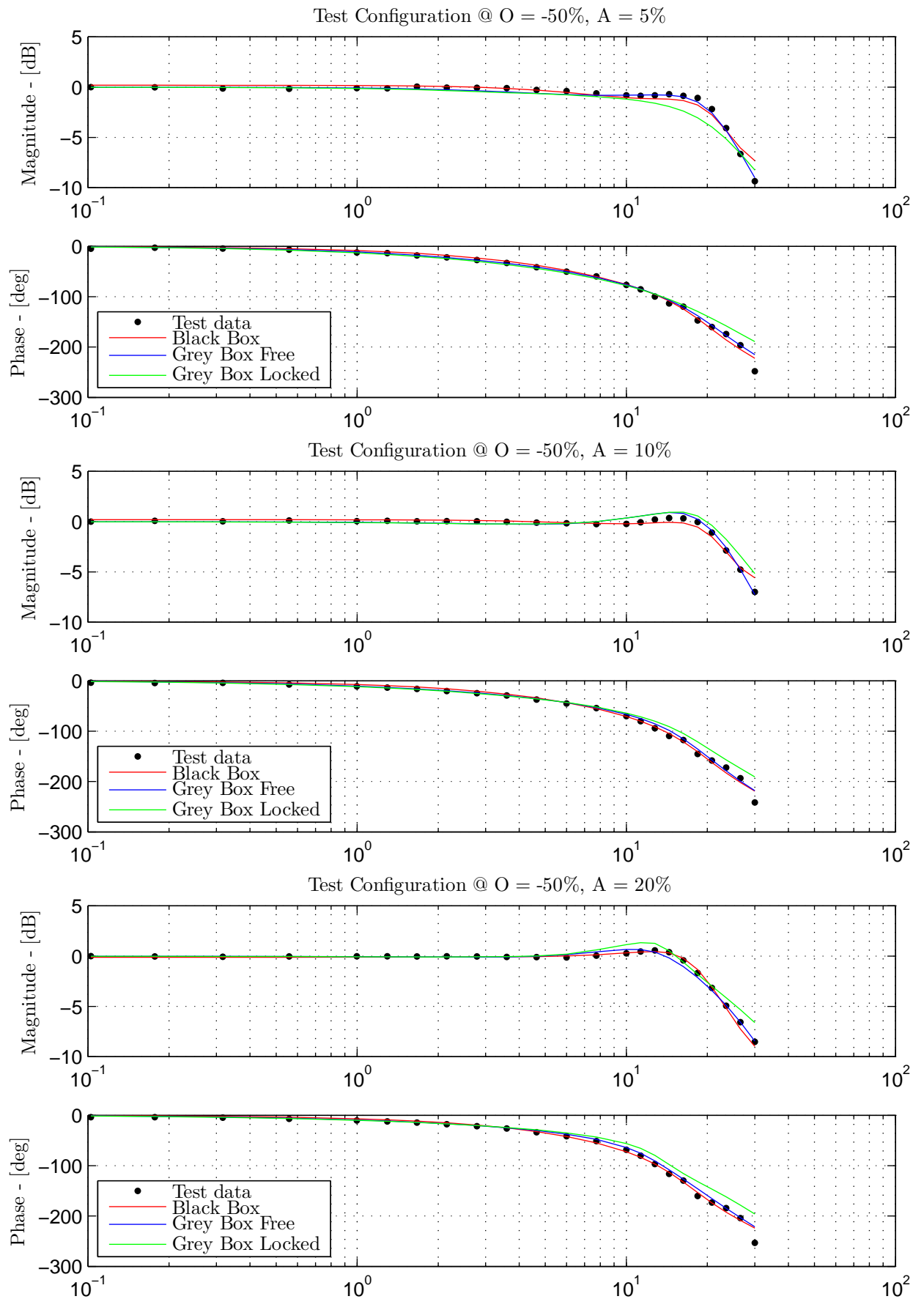


Figure 9: Test data compared with Black and Grey Box model @ O = -50%.

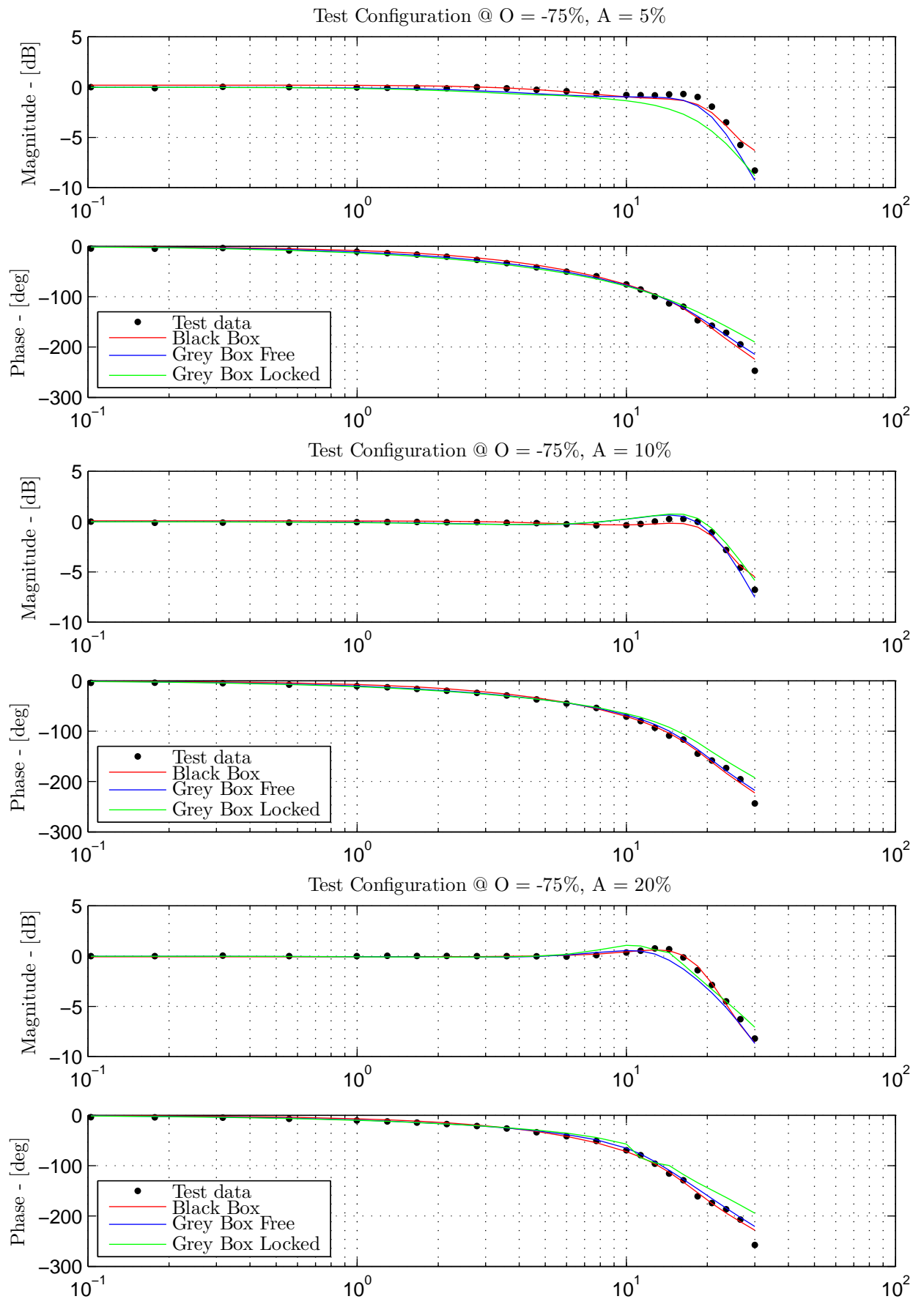


Figure 10: Test data compared with Black and Grey Box model @ O = -75%.

D Sensors and Components

This Appendix presents the core components which are used to perform the physical experiments in the master project. The main parameters and specifications of each single component is extracted from the data sheet and presented in a compressed form. This appendix gives an overview of the main components and their specifications.

D.1 Bosch Rexroth A4VSG Closed Loop Pump

The variable axial piston pump used in this project is delivered by Bosch Rexroth. The complete data sheet containing all the technical descriptions is given by Bosch Rexroth and can be found in [5]. The order code is needed to find several specific specifications about the pump. Our units specific order code is: A4VSG 71HS4KP/10R-PPB10K680N. The description of the order code is found in the data sheet.

The pump is designed using a swash plate mechanism, and meant to be used within closed hydraulic loops. Also the pump is configured to deliver a flow which is proportional to the drive speed and the displacement. The displacement is variable by tilting the swash plate. The swash plate mechanism is controlled by an external control circuit which is described in D.2. A illustration picture of the pump is shown in Figure 11.



Figure 11: Bosch Rexroth axial piston variable pump A4VSG [5].

Bosch Rextroth is not specifying any of the parameters describing the internal components such as the piston diameters, swash plate geometry, lens plate openings and so on. However, they supply the most traditional technical data needed. The technical data of interest in this project is given in Table 1.

Table 1: A4VSG pump parameters.

Description	Variable	Value	Unit
Max displacement	$V_{g,max}$	71	cm^3
Max speed	n_{max}	3200	rpm
Max flow	Q_{max}	227	l/min
Max pressure	p_{max}	400	bar
Nominal pressure	p_{nom}	350	bar
Minimum pressure	p_{min}	15	bar
Max power	P_{max}	132	kW
Maximum swash plate angle	α_{max}	15	deg

D.2 Control Actuating Circuit with Proportional Valve

The axial piston pump described in D.1 requires a control system in order to adjust the swash plate angle. The control system is also delivered by Bosch Rexroth, and the complete technical description is found in the data sheet [6]. The complete order code for the unit used in this project is given as HS4KP and it is located in the pump order code. The variable piston pump with the control system and the servo valve is shown in Figure 12.



Figure 12: Pump control unit with a servo valve [6].

The specifications of the proportional valve shown in Figure 12 is found by searching in the pump's spare part list [26]. The order code of the proportional valve is 4WRE6V08-2X/G24K4/V-822 and the data sheet is found in [16]. The data sheet includes two hard parameters; the control piston stroke length and area as shown in Table 2.

Table 2: Hydraulic control circuit parameters.

Description	Variable	Value	Unit
Control pistons stroke length	L	34.2	mm
Control pistons area	A_p	12.6	cm^2

D.3 Pump Microcontroller Control Card

The hydraulic control piston is controlled using a proportional valve which is controlled by a electronic controller card produced by Bosch Rexroth. The complete specifications of the controller card is found in [7]. The controller card supports a software in which the user can change several parameters. The accompanying software is named BODAC and it can be downloaded from Bosch Rexroth's web pages for free. A picture of the controller card is shown in Figure 13.

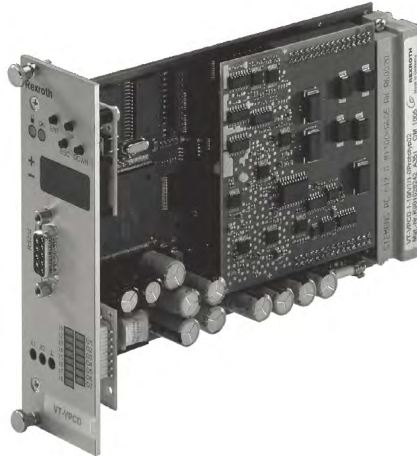


Figure 13: Bosch Rexroth actuating circuit valve control card [7].

D.4 Parker V12 Variable Displacement Motor

The two hydraulic circuits which are supposed to simulate a load situation on the pump described in D.1 consists of two hydraulic motors from Parker. The complete order code is 11005063 V12-060-MS-SV-S-014-D-0-040/020-HOS011-010/000 and a simple picture of the motor is given in Figure 14.



Figure 14: Parker V12 bent axis variable displacement pump [8].

The main pump/motor properties needed in this project is given in Table 3.

Table 3: Parker V12 data sheet specifications.

Description	Variable	Value	Unit
Motor max displacement.	V_{max}	60	cm^3/rev
Maximum swash plate angle.	α_{max}	35	deg
Rotary moment of inertia.	J_m	$3.1 \cdot 10^{-3}$	kgm^2

D.5 Inductive Transmitter

On a shaft between two Parker motors an inductive transmitter is used to get the speed of the shaft. Its technical name is NEB6-12GM50-E2-V1 manufactured by Pepperl+Fuchs [27]. This sensor is placed close to the shaft coupling facing the coupling. When metal is in front of the sensor, the output signal is high, else it's low. The sensor may change this pulse signal up to 800 times per second.

D.6 Parker Servo Valve

The servo valve used in the load circuit is a Parker Servo Valve with the technical name D3FP. The valve is shown in figure 15.



Figure 15: Parker D3FP Servo valve [9].

The valve dynamics is evaluated using a second order transfer function which is fitted to the catalog data. The servo valve parameters needed in this project are given by Table 4.

Table 4: Parker servo valve specifications.

Description	Variable	Value	Unit
Valve opening coefficient	K_{sv}	$1.863 \cdot 10^{-5}$	m^2
Natural frequency	ω_{sv}	78.1	Hz
Damping ratio	ζ_{sv}	0.646	—

The servo valve dynamics have been chosen to be modeled using a second order transfer function. The transfer function describing the servo valve dynamics is given by Equation (5).

$$G_{sv}(s) = \frac{u_{sv}(s)}{u_{sv}^{(ref)}(s)} = \frac{\omega_{sv}^2}{s^2 + 2\zeta_{sv}\omega_{sv}s + \omega_{sv}^2} \quad (5)$$

The comparison between the data sheet bode plot and the second order system valve dynamics prescribed in Table 4 is given in Figure 16.

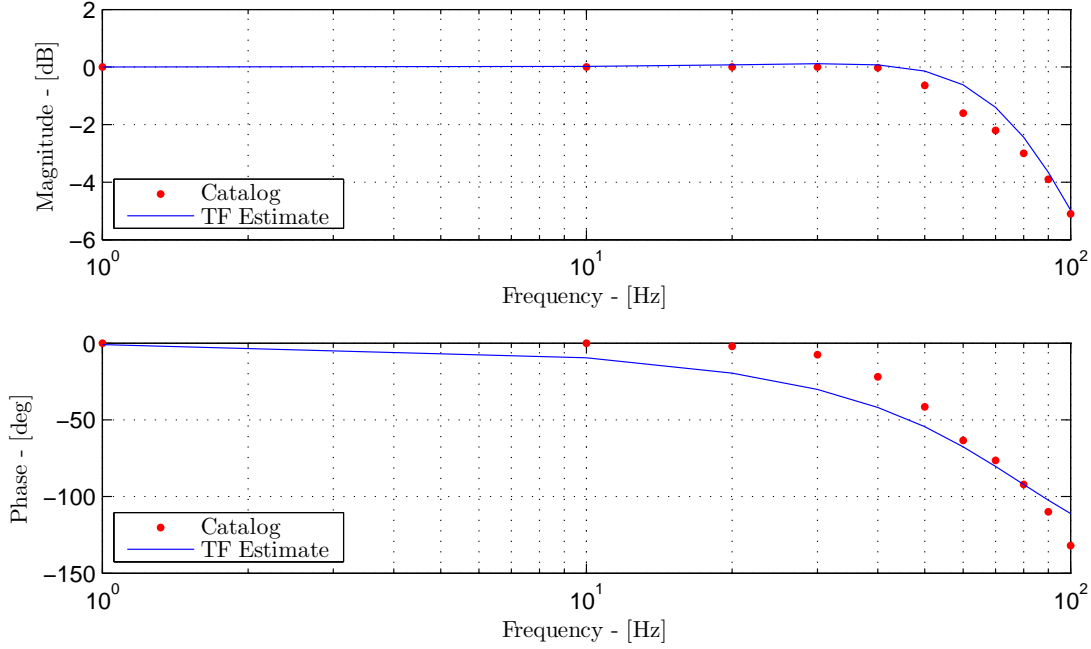


Figure 16: Parker Servo Valve approximated dynamics.

D.7 HYDAC Flow Sensors

In order to measure the flow from the closed loop pump (A4VSG), two HYDAC flow sensors have been used. The product name is HYDAC EVS 3100-H [28] and it is a turbine type flow measurer which converts turbine speed to an electrical signal. The sensor is shown in Figure 17. Because the oil flow from the pump is expected to be up to roughly 100 l/min, the flow measurement device needs to be accurate up to this point. MacGregor's test division have two such flow measurement devices which are capable of flows between 1.2 to 20 l/min and 40 to 600 l/min respectively. Because of the various measurement intervals, both devices are used to measure the flow. The accuracy of the sensor type is less than 2% of the actual value.



Figure 17: HYDAC Flow sensor

D.8 HYDAC Pressure Transmitter

HYDAC Pressure transmitters are used to measure the pressure at certain positions in the hydraulic circuits. The product name is 7400 series and it measures pressures ranging from 0-400 bar with less than 0.5% accuracy. The output is a current signal ranging from 4-20 mA.

D.9 National Instruments myRIO

The National Instruments (NI) myRIO is a compact computer with a System on a Chip (SoC) from Xilinx that includes a dual core ARM Cortex A9 processor and a Field Programmable Gate Array (FPGA) with 28,000 programmable logic cells [29]. It boasts 8 + 2 analog inputs with ranges from 0..5V and -10..+10V respectively, and 4 + 2 analog outputs with ranges from 0..5V and -10..+10V respectively. Also, up to 40 Digital inputs/outputs can be configured. This box is programmed using NI LabVIEW, and can run two different types of programs. The first type is similar to the ones run able on a 32-bit windows computer, which uses the dual core A9 processor. The second type is less flexible in complexity, data types and size, but can be compiled to run on the FPGA. The advantage of using a FPGA is the high clock speed of 40 MHz and fast execution. It is ideal for measuring analog and digital signals at high speeds.

D.10 Laptop Computer

A laptop running 64-bit Windows 8.1 is used to program and initiate the National Instruments myRIO and monitor the pump controller card through BODAC.

E Static Model Parameters

For static model parameters used in simulations of the A4VSG pump, refer to Table 5.

Table 5: Static model parameters used in all simulations of the A4VSG pump.

Parameter	Description	Value	Unit
β	Oil stiffness	1400	MPa
ρ	Density of oil	875	kg/m ³
α_{Max}	Maximum swash plate angle of the pump	15	deg
p_P	Supply pressure on the angle control circuit	170	bar
p_T	Tank pressure on the angle control circuit	0	bar
k_1	Orifice opening area constant	-4.67	mm ²
k_2	Orifice opening area constant	6.6454	mm ²
k_3	Orifice opening area constant	0.967	mm ²

F SimulationX Model of the A4VSG pump

From the pump model in Chapter 3 a SimulationX model is created. This is because MacGregor wants to use the model of the pump as a single block in the simulation software. The interface of this block is simple as it only includes inputs for a motoring shaft, two hydraulic ports and a drain port. The interior however is complex and includes the swash plate dynamics and the flow ripple generator. The parameters of the pump are adjustable through a user interface, but default values should work with the tested pump. This model contains the swash plate dynamics and simplified ripple effects as described in Chapter 3. The entire model is shown in Figure 18 and the equations in the 5 numbered sections are explained in separate tables, namely Table 6 through 10. Any variable that is not displayed, i.e. the eigenfrequency of the valve ω_v , are considered user selected parameters and are not displayed here. In Figure 18 part 1 contains static model parameters that should not change. Part 2 includes the control system given in Section 3.3. Part 3 consists of most of the differential equations describing the system together with time integration. Part 4 includes the equations necessary to calculate the simplified ripple flow. Finally, part 5 handles the volume flow calculation through the pump.

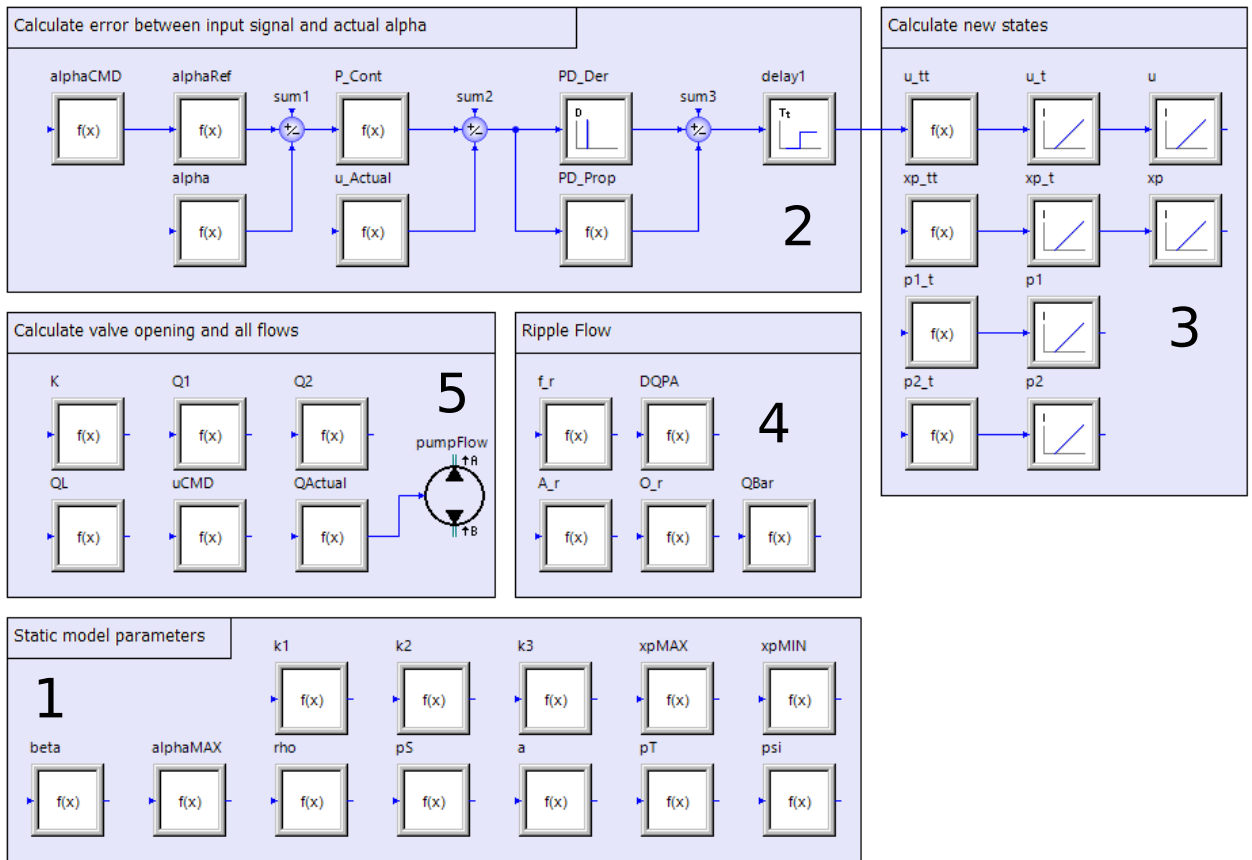


Figure 18: The SimulationX model of the pump.

The SimulationX model shown in this section is compromised into a Modelica block which may be used in any model in SimulationX. The user may change up to 18 parameters in the pump, but the default values of the parameters representing the swash plate dynamics are optimal to represent the true dynamics. The Modelica block and 10 of the adjustable parameters are shown in Figure 19. In this figure two volumes are included to show the two hydraulic ports and a function which shows the location of the swash plate angle command input.

Table 6: Variable explanation of SimX Model part 1.

SimulationX Name	Description	Equation number
beta	Oil stiffness β	-
alphaMAX	Maximum swash plate angle α_{max}	3.21
rho	Oil density ρ	-
pS	Supply pressure p_S	-
a	Distance from swash plate to cylinder a	3.8
pT	Tank pressure p_T	-
psi	Ratio of actual ripple used ψ	3.63
k1, k2, k3	Valve opening area constants k_n	-
xpMAX	Maximum cylinder position practically	-
xpMIN	Minimum cylinder position practically	-

Table 7: Variable explanation of SimX Model part 2.

SimulationX Name	Description	Equation number
alphaCMD	Swash plate angle command between ± 100 .	-
alphaRef	Converted swash plate angle command to radians	-
alpha	Actual swash plate angle	3.10
P_Cont	P-controller	3.18
u_Actual	Actual spool position	-
PD_Der & PD_Prop	PD-controller	3.17
delay1	Time delay	-

Table 8: Variable explanation of SimX Model part 3.

SimulationX Name	Description	Equation number
u_tt	Spool acceleration	3.19
u_t	Spool velocity	-
u	Spool position	-
xp_tt	Cylinder acceleration	3.9
xp_t	Cylinder velocity	-
xp	Cylinder position	-
p1_t	Pressure gradient chamber 1	3.4
p1	Pressure chamber 1	-
p2_t	Pressure gradient chamber 2	3.5
p2	Pressure chamber 2	-

Table 9: Variable explanation of SimX Model part 4.

SimulationX Name	Description	Equation number
f_r	Ripple frequency	3.54
A_r	Ripple amplitude	3.64
O_r	Ripple offset	3.57
QBar	Mean flow	3.48
DQPA	Ripple flow	3.53

Table 10: Variable explanation of SimX Model part 5.

SimulationX Name	Description	Equation number
K	Opening area of the valve	3.3
Q1	Flow into cylinder chamber 1	3.1
Q2	Flow out of cylinder chamber 2	3.2
QL	Leakage flow from cylinder chamber 1 and 2	3.6
uCMD	Actual spool command	-
QActual	Pump flow with/without ripple	-
pumpFlow	Flow source with hydraulic ports	-

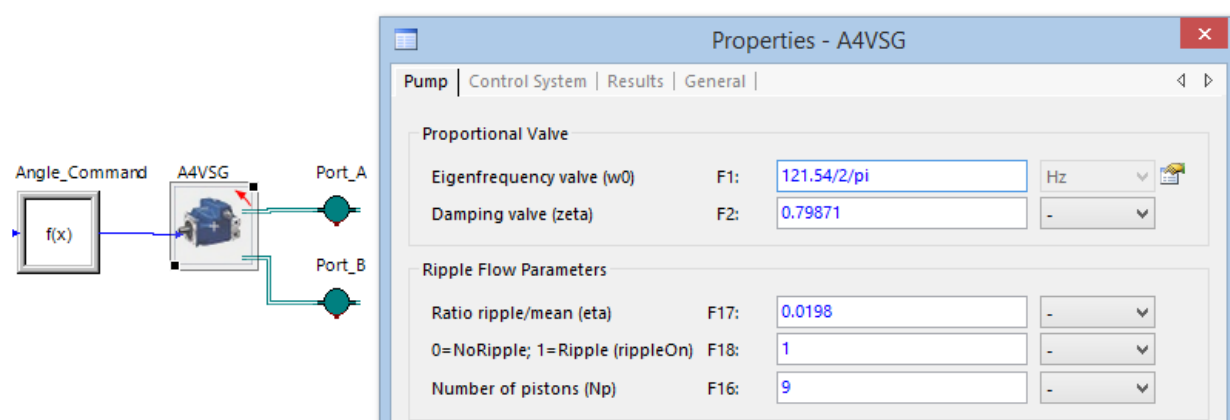


Figure 19: The SimulationX Modelica block model of the pump.

G SimulationX Model of the Hydraulic Load Circuit

The full SimulationX model of the test bench including the load side (Section 5.2) and the supply side (Section 5.3) is described here in detail. A schematic of the model is shown in Figures 20 and 21. In these two figures, the model is divided into groups displayed by red numbers. There are a total of seven groups and they are described below:

- 1 This part contains the friction model as described in Section 5.5. Details about every block is given in Table 11.
- 2a This is the first part of the hydraulic system, i.e. the load circuit. It is controlled via the Servo Valve to keep a reference pressure drop over the parker motor $PumpL$. This circuit is explained in detail in Section 5.2.
- 2b This is the second part of the hydraulic system which is called the supply circuit. It is controlled via the swash plate angle of the pump A4VSG to keep the shaft speed of $PumpS$ as the reference speed. This circuit is explained in detail in Section 5.3.
- 3 This is the controller for the swash plate angle of the A4VSG closed loop pump. The controller is described in detail in Section 5.4 and all the blocks are explained in Table 12.
- 4 This is the controller for the directional control valve which keeps a reference pressure drop over the pump. The control system is detailed in Section 5.4 and the blocks are explained in Table 13.
- 5 This a model of the pulse counter system which mimics an inductive sensor that calculates the speed every time a pulse is encountered on the coupling. The usage of this sensor is explained briefly in Section 5.1 and the blocks are detailed in Table 15.
- 6 Other variables as shown in Table 15.

Table 11: Variable explanation of SimX Model part 1 - Friction model.

SimulationX Name	Description	Equation number
Ts	Maximum static friction τ_s	-
Tc	Coulomb friction τ_c .	-
r	Gradient of change between negative and positive speed r .	-
w0	Rotational velocity at τ_0	-
Tf	Friction torque due to the shaft velocity τ_f	5.38

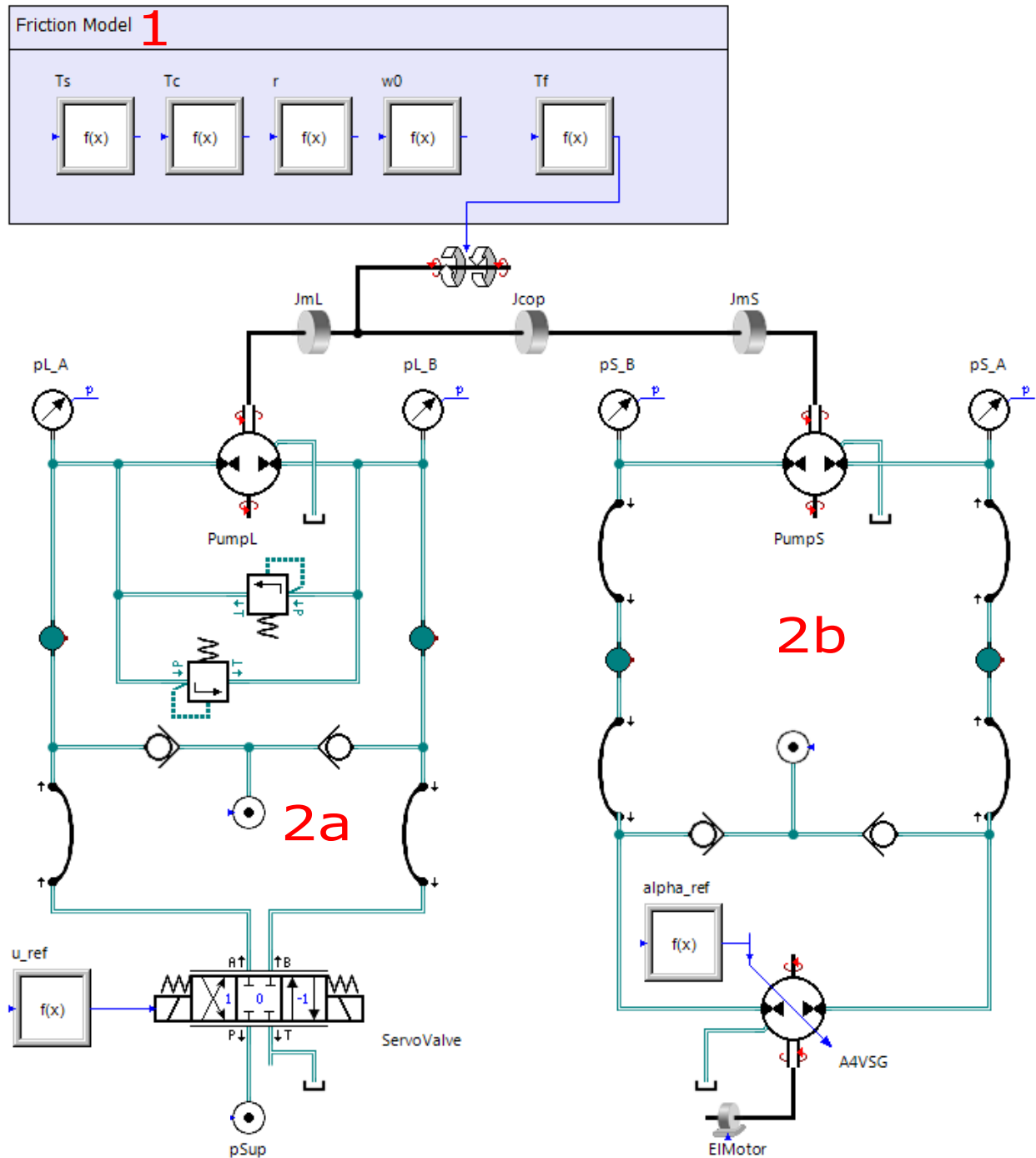


Figure 20: SimulationX model of the Load Circuit test bench.

Table 12: Variable explanation of SimX Model part 3 - Swash plate angle controller.

SimulationX Name	Description	Equation number
omegaS	Measured shaft speed from inductive sensor ω_s	5.1
omegaS_ref	Reference shaft speed $\omega_s^{(ref)}$	-
masterSpeed	Master gain to limit the theoretical control system	-
abs_omegaS	Absolute value of measured omegaS $ \omega_s $	-
ZeroSwitch	Connects controller when speed is over a threshold	-
PI	PI-controller	5.33
alpha_feed	Feed forward signal for angle control $\alpha^{(feed)}$	5.35
Gest	Black box model of swash plate angle dynamics	5.18
alpha	Desired swash plate angle in radians	-
NormalizeSignal	Desired swash plate angle converted to percentage	-

Table 13: Variable explanation of SimX Model part 4 - Servo valve control system.

SimulationX Name	Description	Equation number
pL	Actual pressure drop over the load site pump/motor p_L	5.3
pL_ref	Reference pressure drop $p_L^{(ref)}$	-
masterLoad	Master gain to limit the theoretical control system	-
pi2	PI-controller	5.33
u_feed	Feed forward signal for spool position control	5.37
limit1	Limiter of control signal	-
Negate	Negate the control signal to match mathematical model	-

Table 14: Variable explanation of SimX Model part 5 - Coupling pulse counter system.

SimulationX Name	Description	Equation number
theta	Actual coupling radial position θ_s	-
sum5	Rotation since last pulse	-
absMe	Absolute value of input	-
EventTheta	Triggers one sampling of theta when $absMe$ is larger than the threshold $2\pi/10$.	
contOmega	The actual rotation speed of the shaft ω_s	-
EventOmega	Triggers one reading of continuous ω_s when $absMe$ is larger than $2\pi/10$.	-
discOmega	Measured actual speed when event triggers.	5.1
Time	Simulation time t	-
EventTimer	Triggers one sampling of time when $absMe$ is larger than the threshold $2\pi/10$.	-
Timer	Time since last event trigger.	-

Table 15: Variable explanation of SimX Model part 6 - Other variables.

SimulationX Name	Description	Equation number
Jeff	Effective moment of inertia	Table 5.1
Vm_max	Maximum displacement of the pump/motor	-
pS	Load pressure over motor on supply side	5.21

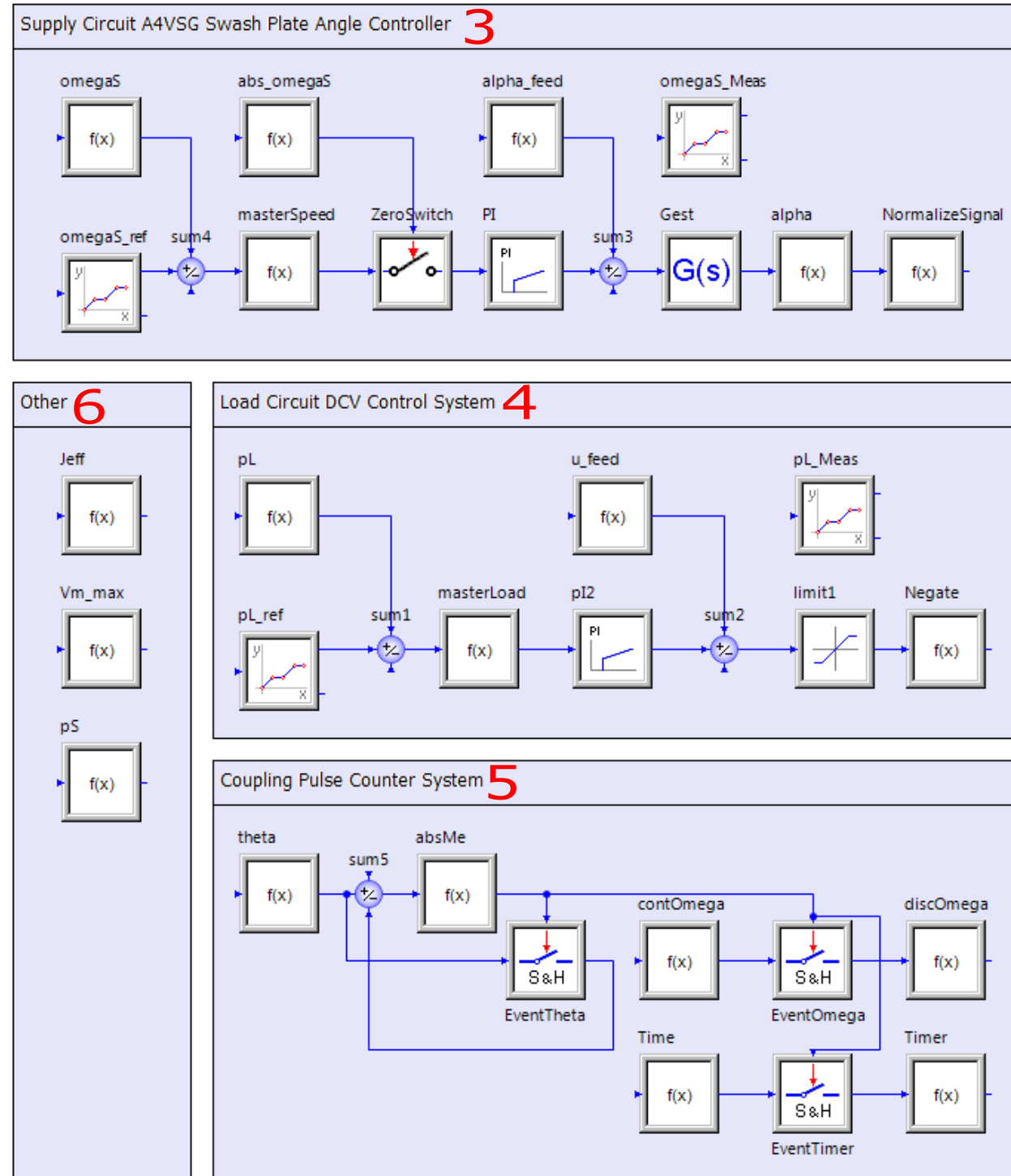


Figure 21: SimulationX model of Controllers.

H Detailed Overall Hydraulic Drawing

